Journal of Space Science and Technology

JSST

Vol.18, Special Issue, 2025

Print ISSN: 2008-4560
Online ISSN: 2423-4516

JSST
Journal of Space Science and Technology

Journal of
Space Science and Technology

Vol. 18, Special Issue, 2025

Indexed in:
DOAJ, ISC, EBSCO, …

Publisher: IAS

Director-in-Charge: M. Navabi, PhD.
Editor-in-Chief: R. Ebrahimi, PhD.
Deputy Editor: M. Azimi, PhD

Address: No. 1, Mohandes St., Darya Blv.
Tehran, I.R. Iran

Tel: +98(21) 88366030
Website: https://jsstpub.com
E-Mail: jsst@jsstpub.com
International E-Mail: info1@jsstpub.com

Print ISSN: 2008 - 4560 **Online ISSN: 2423 - 4516**

International Editorial Board

Andon Dimitrov Lazarov, Professor, Information Technology Department, Nikola Vaptsarov Naval Academy, Bulgaria
Mohamed Himdi, Professor, Institute of Electronics and Digital Technologies, University of Rennes 1, France
Helmi Zulhaidi Mohd Shafri, Associate Professor, Department of Civil Engineering, University Putra Malaysia, Malaysia
Hajar Binti Ja'afar, Associate Professor, School of Electrical Engineering, MARA Technological University, Malaysia
Nicola Luigi Bragazzi, Professor, University of Parma, Italy
Samir Ladaci, Professor, Department of Automatics and Control Engineering, National Polytechnic School of Algiers, Algeria
Syed Amer Mahmood, Professor, Department of Space Science, University of the Punjab, Pakistan
Mahmoud Najafi, Professor, Department of Mathematical Sciences, Kent State University, USA

Editorial Board

Mohsen Bahrami, Professor, Department of Mechanical Engineering, Amirkabir University of Technology
Hossein Bolandi, Professor, Department of Electrical Engineering, Iran University of Science and Technology
Mohammad Farshchi, Professor, Department of Aerospace Engineering, Sharif University of Technology
S. Mostafa Hoseinalipour, Professor, School of Mechanical Engineering, Iran University of Science and Technology
Mansour Kabganian, Professor, Department of Mechanical Engineering, Amirkabir University of Technology
Mehran Mirshams, Professor, Faculty of Aerospace Engineering, K. N. Toosi University of Technology
M. Navabi, Associate Professor, Faculty of New Technologies Engineering, Shahid Beheshti University
S. Hossein Pourtakdoust, Professor, Department of Aerospace Engineering, Sharif University of Technology
Jafar Roshanian, Professor, Faculty of Aerospace Engineering, K. N. Toosi University of Technology
Mohammad Homayoune Sadr, Professor, Department of Aerospace Engineering, Amirkabir University of Technology
Mohammad Taeibi-Rahni, Professor, Department of Aerospace Engineering, Sharif University of Technology
Mohammad Tahaye Abadi, Associate Professor, Aerospace Research Institute

Advisory Board

Mohammad Hassan Entezari, Scientist, Iranian Research Organization for Science and Technology
Hamid Fazeli, Associate Professor, Malek Ashtar University of Technology
Ali Akbar Golroo, Lecturer, Aerospace Research Institute
Abolghasem Naghash, Associate Professor, Department of Aerospace Engineering, Amirkabir University of Technology
S. Mostafa Safavi Homami, Professor, Department of Electrical Engineering, Amirkabir University of Technology
Saeed Shakhesi, Associate Professor, Iranian Space Research Center

Table of Contents

JSST
Journal of Space Science and Technology

P-ISSN: 2008-4560
E-ISSN: 2423-4516

Journal of Space Science and Technology

Vol. 18, Special Issue, pp. 1-15, 2025
https://doi.org/10.22034/jsst.2025.1527
Journal Homepage: https://www.jsstpub.com

Original Research Paper

Cyber Risk Prediction for UAVs in Space-Related Missions Using Deep Reinforcement Learning

Erfan Khosravian[1]* and Motahareh Dehghan[2]

1. Faculty of Mechanical Engineering, Payame Noor University, Tehran, Iran
2. Faculty of Industrial and Systems Engineering, Tarbiat Modares University, Tehran, Iran

ARTICLE INFO

Article History:

Received 21 January 2025
Revised 07 February 2025
Accepted 09 February 2025
Available Online 01 March 2025

Keywords:

Space-related missions
Satellites
Unmanned aerial vehicles (UAV)
Cyber risk prediction
Deep reinforcement learning
Feature importance

ABSTRACT

Space exploration and satellite deployment drive modern technological advancements. They are crucial for global communication, navigation, and scientific discovery. Satellites form the backbone of interstellar communication, ensuring reliable data transfer in both civilian and defense sectors. However, as space missions grow more complex, maintaining their integrity and security becomes a major challenge. Unmanned aerial vehicles (UAVs) play a key role in space missions. They assist in satellite deployment, orbital inspections, and inter-satellite communication. Yet, these cyber-physical systems face evolving cybersecurity threats that could jeopardize mission-critical tasks. Traditional intrusion detection systems struggle to counter the complex and dynamic cyber threats targeting UAVs in harsh space environments. This paper introduces a novel Deep Reinforcement Learning model to predict and mitigate cyber risks in space-related UAV missions. Using a publicly available dataset that combines cyber and physical UAV data, the model predicts multi-step threats such as Denial of Service, Replay, Evil Twin, and False Data Injection. This enables proactive threat mitigation. Compared to traditional machine learning models—Support Vector Machines, Random Forests, and Recurrent Neural Networks—the proposed model achieves superior performance, with 99.34% accuracy and an AUC score of 0.99.

---

*Corresponding Author's E-mail: erfankhosravain@pnu.ac.ir

How to Cite this Article:
E. Khosravian and M. Dehghan, "Cyber risk prediction for UAVs in space-related missions using deep reinforcement learning," *Journal of Space Science and Technology*, Vol. 18, Special Issue, pp. 1-15, 2025, https://doi.org/10.22034/jsst.2025.1527.

1. Nomenclature & Units

DRL	Deep Reinforcement Learning
FDI	False Data Injection
DoS	Denial Of Service
IDS	Intrusion Detection System
UAV	Unmanned Aerial Vehicle
FDI	False Data Injection
AUC	Area Under Curve
SHAP	Shapley Additive Explanation
APT	Advanced Persistent Threat
SVM	Support Vector Machine
RNN	Recurrent Neural Network
RF	Random Forest
H-LSTM	Hierarchical Attention-Based Long-Short Term Memory
ConvLSTM	Convolutional LSTM
CNN-LSTM	Convolutional Neural Networks- Long Short Term Memory
WRELM	Weighted Regularized Extreme Learning Machine
QIWO	Quantum Invasive Weed Optimization
DQN	Deep Q-Network
WLAN	Wireless Local Area Network
UDP	User Datagram Protocol
MDP	Markov Decision Process
FIA	Feature Importance Analysis

2. INTRODUCTION

Space has always been of strategic importance, encompassing satellite deployment, planetary exploration, and interstellar communication. Satellites play a vital role in global connectivity, navigation, weather forecasting, and defense [1]. As nations and private enterprises expand space ventures, mission success becomes paramount. However, the harsh and dynamic space environment poses unique challenges, demanding advanced technologies for seamless and adaptive operations [2].

UAVs are key enablers of space missions. They support satellite deployment, facilitate real-time communication, and inspect or maintain orbiting structures. Unlike ground-based systems, UAVs offer agility, precision, and autonomy to navigate complex space environments. Their ability to operate autonomously in zero gravity enhances mission efficiency while reducing human intervention in high-risk scenarios. However, integrating UAVs into space operations introduces cybersecurity challenges [3].

In space missions, UAVs link satellites and ground infrastructure, ensuring uninterrupted communication and data flow. Any cyber threat could disrupt satellite alignment, interfere with telemetry, or even compromise entire missions [4]. UAVs, as complex cyber-physical systems, require robust security solutions addressing both cyber and physical vulnerabilities. As cyber threats grow, securing UAVs becomes essential for their safe and effective use in critical applications [5].

Cybersecurity threats targeting UAVs are becoming increasingly complex. Multi-step attacks such as DoS, Replay, Evil Twin, and FDI can lead to loss of control, data integrity breaches, and even mission failure [6]. While IDSs exist to counter these threats, many are limited in effectiveness. Most IDSs rely on small datasets and struggle to generalize across different threat types [7]. The lack of publicly available cyber-physical UAV data further hinders the development of robust IDS solutions. These challenges highlight the need for advanced models that not only detect threats but also predict their evolution [8].

This paper introduces a predictive model designed to forecast the next step in multi-step cyber threats on UAVs. Unlike traditional IDSs that merely detect threats, our model anticipates how an attack may progress—such as a DoS attack escalating to replay or FDI. To achieve this, we utilize DRL, which enables learning from sequential threat data to predict future attack steps. The model is trained and tested on a newly available dataset that captures both cyber and physical UAV data under normal and attack conditions, offering a comprehensive view of UAV security [9]. The key contributions and innovations of this research are outlined below.

- **Proactive Threat Mitigation**: The DRL-based model predicts the next step in multi-step cyber threats on UAVs, allowing for proactive defense measures rather than reactive responses.

- **Feature Importance Analysis**: The model incorporates FIA to identify and utilize critical features - such as time_since_last_packet and wlan.duration -improving prediction accuracy and minimizing noise.
- **Evaluation against Leading Models**: The proposed model is rigorously evaluated against baseline models, including SVM, RF, and RNN, demonstrating superior performance across all metrics.
- **Real-Time Threat Prediction**: By leveraging DRL, the model learns threat patterns in real-time, enabling it to adapt to evolving threats as they emerge.
- **Comprehensive Performance Evaluation**: The model's effectiveness is measured using accuracy, precision, recall, F1-score, and AUC, making it highly suitable for deployment in real-world UAV applications.

The paper is structured as follows:

Section 2 reviews current methods for UAV cybersecurity, including traditional IDS techniques and recent advancements in machine learning approaches. Section 3 details the architecture of the proposed DRL-based prediction model, including the hyperparameters tuning process and the role of feature importance in enhancing performance. Section 4 presents the evaluation results of the proposed model, comparing its performance with baseline models and providing a detailed analysis of the metrics. Section 5 discusses the FIA, highlighting the significance of key features in improving the model’s predictions. Sections 6 and 7 conclude the paper with a discussion and summary of the findings.

3. RELATED WORKS

The use of unmanned aerial vehicles (UAVs) is expanding into space exploration, satellite deployment, and communication, where reliability is crucial for mission success. Operating in dynamic and complex environments, UAVs have become essential for autonomous space missions. However, their increasing deployment brings significant cybersecurity risks, making robust security measures vital. Among the most common threats are DoS, Replay, Evil Twin, and FDI, which can compromise UAV operations in military, surveillance, and emergency response scenarios [9,10].

Sarıkaya and Bahtiyar in [11] reviewed UAV security challenges and explore DRL as a solution. They highlight how DRL-based approaches enhance UAV resilience against cyber and physical threats. Recent research has also advanced UAV cybersecurity. Niyonsaba et al. in [12] developed deep learning-based IDSs, including CNN, LSTM, and hybrid CNN-LSTM models. Their approach, evaluated on the CICIDS2017 dataset, showed that the hybrid model achieved 99.063% accuracy, outperforming traditional machine learning methods.

Javeed et al. in [13] introduced an IDS using H-LSTM networks. This model improves UAV monitoring by focusing on critical features and incorporating SHAP for interpretability. Tested on the N-BaIoT dataset, the H-LSTM model achieved high detection accuracy with fewer false positives. Alzahrani in [14] proposed a ConvLSTM model to secure IoT-enabled small drones. Using datasets like KDD Cup-99, NSL-KDD, and CICIDS2017, the ConvLSTM model demonstrated 99.99% accuracy in intrusion detection.

Dehghan and Khosravian in [15] introduced a federated learning approach with homomorphic encryption to enhance UAV IDSs, ensuring data privacy. Rizwanullah et al. in [16] developed MMLCS-UAVs, a metaheuristic-based approach combining QIWO for feature selection and WRELM for intrusion detection.

Despite these advancements, most IDSs focus on detecting anomalies in network traffic but struggle to predict multi-step threats [17]. This gap highlights the need for predictive models that anticipate cyber threats before they escalate. This paper proposes a DRL-based model to forecast the next steps in multi-phase attacks.

DRL enables systems to learn optimal responses by interacting with their environment, making it effective in robotics, gaming, and cybersecurity [18]. One notable application, ProAPT [19], uses DRL to predict the progression of APTs. Similarly, applying DRL to UAV cybersecurity allows for forecasting cyber threats and taking preventive actions before escalation. While research on DRL for UAV security is still emerging, its potential for improving threat detection and prediction is significant.

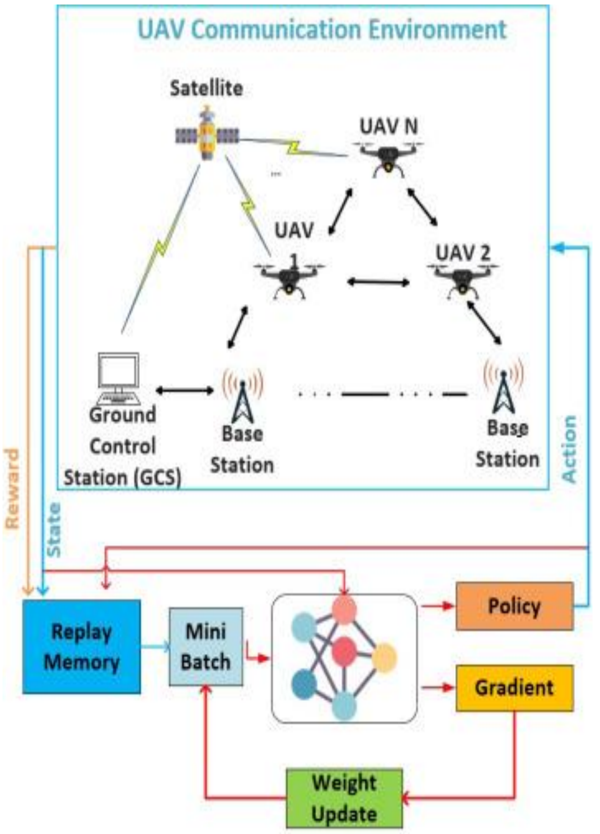

Fig. 1. Deep reinforcement learning for UAVs in space-related missions [11].

4. PROPOSED MODEL

The proposed model for predicting cyber-threat progression in UAV systems is inspired by the ProAPT model, which uses DRL to track the evolution of APTs. This approach is effective for threat prediction as it learns from both the current system state and past attack sequences. By leveraging a reinforcement learning framework, the model anticipates the next threat in an ongoing attack, enabling UAVs to take proactive countermeasures before escalation.

The model predicts the next threat type based on the current attack and system state, focusing on four key threats: DoS, Replay, Evil Twin and FDI. It is trained on a publicly available dataset containing UAV operation data under both normal and attack conditions.

Built on a reinforcement learning framework, the model follows a state-action-reward paradigm, assessing system status and past threats to forecast future attacks [20]. The state space includes key UAV system features such as:

- **Current Threat:** The threat type currently being executed on the UAV system. Understanding this is vital for determining the system's vulnerabilities and predicting subsequent threat types.
- **UAV System Status:** The operational state of the UAV, including sensor readings, flight status, communication health, and control system performance. These features help evaluate the UAV's overall health and resilience against threats.
- **Historical Threat Data:** The record of past threats and their effects on the UAV system, providing context for predicting future threats.

The dynamic state space updates continuously as the UAV system evolves, allowing the model to adapt to changing threats and conditions. The action space includes four main threat types—DoS, Replay, FDI, and Evil Twin—representing possible next steps in an attack sequence. The model predicts which threat is most likely to occur next based on the current system state and attack history, helping the UAV system anticipate the adversary's next move.

The reward function is designed to optimize threat prediction accuracy. It evaluates the model's predictions against actual threats and assigns rewards accordingly. The reward structure is as follows:

- **Positive Reward:** The model receives a positive reward if the predicted threat matches the actual threat in the sequence.
- **Negative Reward:** A penalty is applied if the model incorrectly predicts the threat, reinforcing the need for accurate predictions.
- **Intermediate Rewards:** For partial correct predictions (e.g., correctly identifying the threat category but not the exact type), smaller rewards are given to encourage learning from partial successes.

This reinforcement learning framework improves predictions over time by refining its strategy based on feedback. The DRL model is built on DQN [21] and consists of the following components:

- **Neural Network:** The core of the DRL model is a neural network that processes input states (system status, current threat, etc.) and predicts the next threat. It may include fully connected layers or recurrent layers like LSTM to capture temporal dependencies in attack sequences.

- **Q-Learning / DQN:** The model uses DQN to learn the optimal action-value function. It estimates Q-values, representing expected rewards for each action in a given state, and aims to maximize these rewards by predicting the most probable next threat.
- **Exploration vs. Exploitation:** Using an epsilon-greedy strategy, the model balances exploration (trying new actions) and exploitation (choosing the best-known actions). This prevents overfitting to specific threats and encourages learning across diverse attack patterns.

The model is trained on a dataset containing UAV operations under normal and attack conditions. The training process includes key steps:

- **Data Preprocessing:** The dataset is standardized, and missing values are handled figure 2. Feature selection reduces input dimensionality, ensuring only the most relevant variables are used, improving efficiency and accuracy.

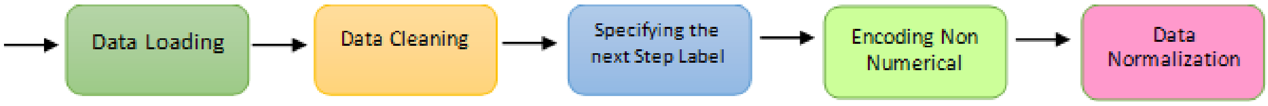

Fig. 2. Pre-processing steps.

- **Hyperparameter Tuning:** Key parameters like learning rate, discount factor, and exploration rate are optimized using grid search. This ensures the best performance by finding the ideal combination of these values.
- **Model Training:** The model learns through reinforcement learning, updating Q-values based on feedback from the reward function. Over time, it refines its ability to predict threats accurately.
- **Testing and Evaluation:** After training, the model is tested using classification metrics such as accuracy, precision, recall, F1-score, and AUC. These metrics measure its predictive performance and reliability. AUC, in particular, assesses the model's ability to differentiate between various threats.

By using these evaluation methods, we determine how effectively the model predicts the next cyber-threat, contributing to proactive UAV defense strategies.

5. EXPERIMENTAL SETUP AND EVALUATION

The cyber-physical IDS for UAVs dataset [9] serves as the foundation for evaluating our proposed model. Based on [9], the dataset used in this study is derived from the cyber-physical IDS for UAVs. This dataset has been specifically designed to capture both cyber and physical features of UAV operations under normal and attack scenarios, making it well-suited for training and testing intrusion detection models.

The dataset contains 38 features that cover various operational aspects of UAVs, including network traffic patterns, sensor data, and control system telemetry. It is divided into 5 distinct classes normal operations, DoS, Replay, Evil Twin, and FDI attacks. It includes a large number of instances, providing a diverse range of attack scenarios across different UAV use cases. The total dataset size ensures that the model is trained on a variety of attack patterns, significantly reducing overfitting and improving generalization to new, unseen threats. This dataset includes a variety of common cyber-physical threats targeting UAVs. It covers attacks that exploit both network vulnerabilities and physical system weaknesses, such as:

- **Denial of Service (DoS):** Preventing the UAV from accessing critical services by overwhelming its communication network.
- **Replay Attacks:** Capturing and retransmitting valid communication data to deceive the UAV.
- **Evil Twin Attacks:** A scenario where an attacker masquerades as a legitimate access point to intercept UAV communications.
- **False Data Injection (FDI):** Injecting malicious data into the system to disrupt UAV operations, often affecting sensor or control data.

Each threat is simulated within a controlled environment that mimics real-world UAV operations, ensuring that the dataset is representative of typical use cases in mission-critical UAV applications. The dataset is designed to simulate a wide array of UAV operational contexts, ensuring it encompasses various scenarios such as normal operations in civilian and military settings, emergency and surveillance missions where UAVs need to maintain high reliability and security, and real-time communication relay operations between UAVs and ground stations, where maintaining data integrity is crucial. These varied scenarios ensure that the dataset covers a broad spectrum of potential UAV applications, making it suitable for training models that need to be generalized to different environments. The data has been carefully collected from both cyber and physical dimensions, including telemetry data, communication logs, and sensor readings, to provide a holistic view of UAV system behavior under both normal and attack conditions. Given its comprehensive coverage of threat scenarios, this dataset is highly suitable for both training and testing machine learning models focused on UAV cybersecurity. The multi-class nature of the dataset allows for the evaluation of the model’s ability to differentiate between multiple types of attacks, as well as its performance in real-world UAV scenarios. moreover, the dataset includes labeled instances of attacks, ensuring that models can be trained in a supervised manner, with clear distinctions between malicious and benign behavior. This makes it an effective tool for developing and testing cyber-physical intrusion detection systems that aim to enhance UAV security.

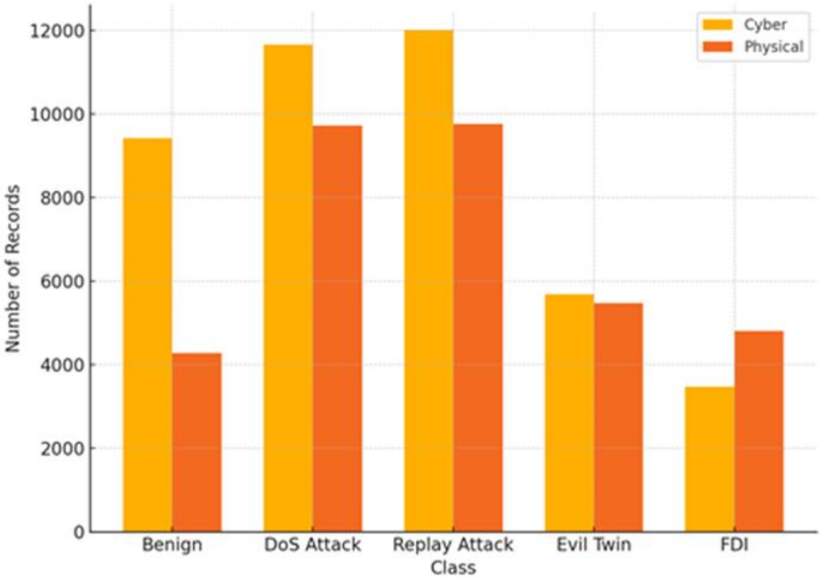

Fig. 3. Distribution of five classes in the dataset.

First, we preprocess the dataset following the steps in Figure 2. Next, we perform a grid search [22] for hyperparameters tuning on a Q-Learning based model, using a reduced parameter grid to evaluate performance. This involves setting up the Q-Learning environment, applying the grid search, and analyzing the results for each hyperparameters combination. The outcomes are summarized in Table 1 and visualized in Figure 3. The table presents the average reward and standard deviation for each combination, helping to determine optimal values for learning rate, discount factor, exploration rate, batch size, and target update frequency. The standard deviation reflects reward consistency across episodes, where lower values indicate greater stability. Figure 4 further illustrates these results, with each point representing a hyperparameters combination and error bars showing the standard deviation. By balancing reward and stability, we identify hyperparameters settings that achieve both high average rewards and low variability, making them ideal for model training.

Table 1. Q- Learning hyperparameters greed search result.

std_reward	average_reward	params
21.1359744	247.5137956	{'batch_size': 32, 'discount_factor': 0.9, 'exploration_rate': 0.1, 'learning_rate': 0.1, 'target_update_frequency': 100}
18.98846078	249.9578762	{'batch_size': 32, 'discount_factor': 0.9, 'exploration_rate': 0.1, 'learning_rate': 0.1, 'target_update_frequency': 500}
17.71009204	250.0179335	{'batch_size': 32, 'discount_factor': 0.9, 'exploration_rate': 0.1, 'learning_rate': 0.5, 'target_update_frequency': 100}
21.63080579	248.4489532	{'batch_size': 32, 'discount_factor': 0.9, 'exploration_rate': 0.1, 'learning_rate': 0.5, 'target_update_frequency': 500}
18.34741134	251.6797308	{'batch_size': 32, 'discount_factor': 0.9, 'exploration_rate': 0.5, 'learning_rate': 0.1, 'target_update_frequency': 100}
21.36083092	251.2519457	{'batch_size': 32, 'discount_factor': 0.9, 'exploration_rate': 0.5, 'learning_rate': 0.1, 'target_update_frequency': 500}
17.72686258	246.8532666	{'batch_size': 32, 'discount_factor': 0.9, 'exploration_rate': 0.5, 'learning_rate': 0.5, 'target_update_frequency': 100}
20.82083433	251.9783953	{'batch_size': 32, 'discount_factor': 0.9, 'exploration_rate': 0.5, 'learning_rate': 0.5, 'target_update_frequency': 500}
20.34282947	247.4348603	{'batch_size': 32, 'discount_factor': 0.99, 'exploration_rate': 0.1, 'learning_rate': 0.1, 'target_update_frequency': 100}
20.82049582	247.5401704	{'batch_size': 32, 'discount_factor': 0.99, 'exploration_rate': 0.1, 'learning_rate': 0.1, 'target_update_frequency': 500}
18.97466687	250.7741141	{'batch_size': 32, 'discount_factor': 0.99, 'exploration_rate': 0.1, 'learning_rate': 0.5, 'target_update_frequency': 100}
21.64458778	249.5405649	{'batch_size': 32, 'discount_factor': 0.99, 'exploration_rate': 0.1, 'learning_rate': 0.5, 'target_update_frequency': 500}
20.47600339	248.9452282	{'batch_size': 32, 'discount_factor': 0.99, 'exploration_rate': 0.5, 'learning_rate': 0.1, 'target_update_frequency': 100}
19.992076	251.4655468	{'batch_size': 32, 'discount_factor': 0.99, 'exploration_rate': 0.5, 'learning_rate': 0.1, 'target_update_frequency': 500}
18.19167563	252.0576918	{'batch_size': 32, 'discount_factor': 0.99, 'exploration_rate': 0.5, 'learning_rate': 0.5, 'target_update_frequency': 100}
20.98148314	250.5580712	{'batch_size': 32, 'discount_factor': 0.99, 'exploration_rate': 0.5, 'learning_rate': 0.5, 'target_update_frequency': 500}
20.28485974	249.1730499	{'batch_size': 64, 'discount_factor': 0.9, 'exploration_rate': 0.1, 'learning_rate': 0.1, 'target_update_frequency': 100}
19.66271791	253.0944403	{'batch_size': 64, 'discount_factor': 0.9, 'exploration_rate': 0.1, 'learning_rate': 0.1, 'target_update_frequency': 500}
17.9560669	250.5274853	{'batch_size': 64, 'discount_factor': 0.9, 'exploration_rate': 0.1, 'learning_rate': 0.5, 'target_update_frequency': 100}
21.27665195	247.8462585	{'batch_size': 64, 'discount_factor': 0.9, 'exploration_rate': 0.1, 'learning_rate': 0.5, 'target_update_frequency': 500}
18.96873134	247.7319118	{'batch_size': 64, 'discount_factor': 0.9, 'exploration_rate': 0.5, 'learning_rate': 0.1, 'target_update_frequency': 100}
19.80201262	248.4106121	{'batch_size': 64, 'discount_factor': 0.9, 'exploration_rate': 0.5, 'learning_rate': 0.1, 'target_update_frequency': 500}
20.21036297	249.1504777	{'batch_size': 64, 'discount_factor': 0.9, 'exploration_rate': 0.5, 'learning_rate': 0.5, 'target_update_frequency': 100}
17.10374115	248.8757748	{'batch_size': 64, 'discount_factor': 0.9, 'exploration_rate': 0.5, 'learning_rate': 0.5, 'target_update_frequency': 500}
19.69385759	254.6294979	{'batch_size': 64, 'discount_factor': 0.99, 'exploration_rate': 0.1, 'learning_rate': 0.1, 'target_update_frequency': 100}

std_reward	average_reward	params
21.18109694	249.9136594	{'batch_size': 64, 'discount_factor': 0.99, 'exploration_rate': 0.1, 'learning_rate': 0.1, 'target_update_frequency': 500}
19.40166479	252.7295711	{'batch_size': 64, 'discount_factor': 0.99, 'exploration_rate': 0.1, 'learning_rate': 0.5, 'target_update_frequency': 100}
22.85800608	250.1627762	{'batch_size': 64, 'discount_factor': 0.99, 'exploration_rate': 0.1, 'learning_rate': 0.5, 'target_update_frequency': 500}
20.1933785	249.8034661	{'batch_size': 64, 'discount_factor': 0.99, 'exploration_rate': 0.5, 'learning_rate': 0.1, 'target_update_frequency': 100}
20.48796075	251.880191	{'batch_size': 64, 'discount_factor': 0.99, 'exploration_rate': 0.5, 'learning_rate': 0.1, 'target_update_frequency': 500}
17.04230555	251.1224726	{'batch_size': 64, 'discount_factor': 0.99, 'exploration_rate': 0.5, 'learning_rate': 0.5, 'target_update_frequency': 100}
19.0126865	253.7873657	{'batch_size': 64, 'discount_factor': 0.99, 'exploration_rate': 0.5, 'learning_rate': 0.5, 'target_update_frequency': 500}

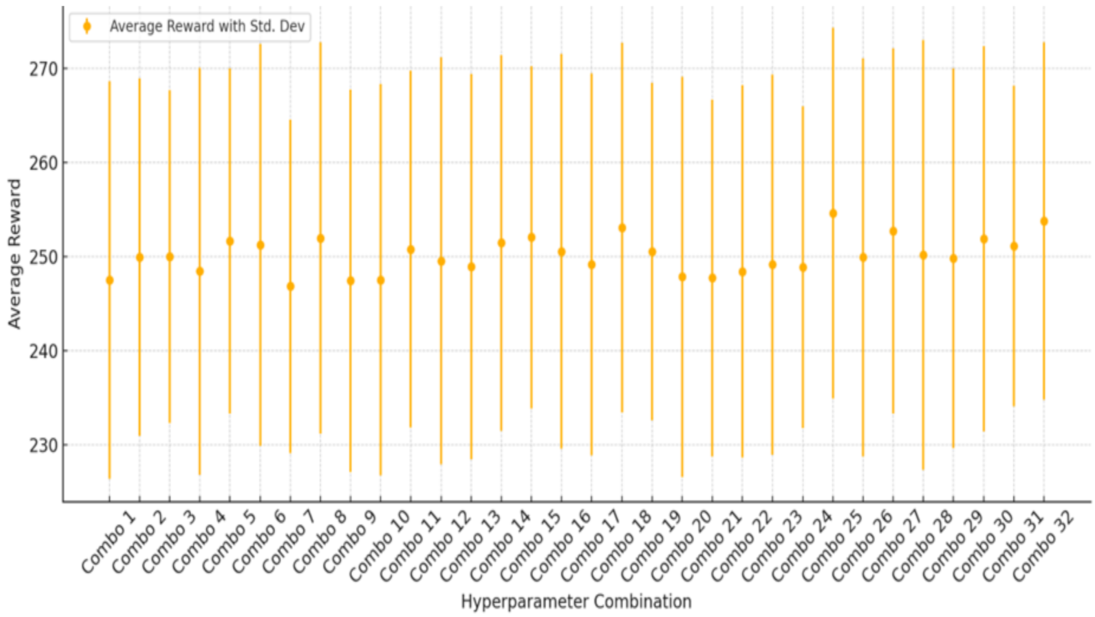

Fig. 3. Q- Learning hyperparameters greed search result.

Based on the greed search, we use the hyperparameters as follows:

Table 2. The best hyperparameters.

Hyperparameter	Value
Learning Rate	0.1
Discount Rate	0.99
Exploration Rate	0.1
Batch Size	64
Target Update Frequency	500

A low learning rate ensures stable model updates, while a high discount factor prioritizes long-term rewards. A low exploration rate encourages the model to exploit learned policies, whereas a larger batch size and higher update frequency help stabilize training. To evaluate our prediction model's performance, we use key metrics outlined by [23]:

- **Accuracy**: Measures the proportion of correct predictions, indicating overall model performance in predicting the next threat step.

- **Precision:** Assesses the percentage of correctly predicted threats, minimizing false positives—critical in cybersecurity.
- **Recall:** Measures the proportion of actual threats correctly identified, ensuring threats are not missed, even at the cost of some false positives.
- **F1-Score:** The harmonic mean of precision and recall, balancing both metrics, is especially useful for imbalanced datasets.
- **Error Rate:** This represents the proportion of incorrect predictions, where a lower value indicates higher reliability.
- **AUC (Area under the Curve):** Evaluates the model's ability to distinguish between different threat steps, with a higher AUC indicating better differentiation.

These metrics are crucial for assessing how well the model predicts multi-step threat sequences. Precision and recall are particularly important in cybersecurity to reduce false positives while ensuring timely threat detection. Table 3 presents the model's performance in predicting the next threat step, comparing it with baseline models such as SVM, RF, and a basic RNN.

Table 3. The result of multi-step threat prediction.

Model	Accuracy (%)	Precision (%)	Recall (%)	F1-Score	Error Rate (%)	AUC Score
Proposed DRL Model	96.5	94.2	95.8	95.0	3.5	0.98
SVM	85.3	82.1	78.4	80.2	14.7	0.88
RF	89.7	87.3	85.6	86.4	10.3	0.90
Basic RNN	91.2	88.9	90.3	89.6	8.8	0.93

As shown in table 3, the proposed DRL model outperforms all baseline models across key metrics, including accuracy, precision, recall, F1-score, and AUC. It achieved an impressive 96.5% accuracy, with 94.2% precision and 95.8% recall. The F1 score of 95.0% reflects a strong balance between precision and recall, while the AUC score of 0.98 highlights the model's exceptional ability to distinguish between different threat types. Figure 5 presents the confusion matrix, visualizing these results.

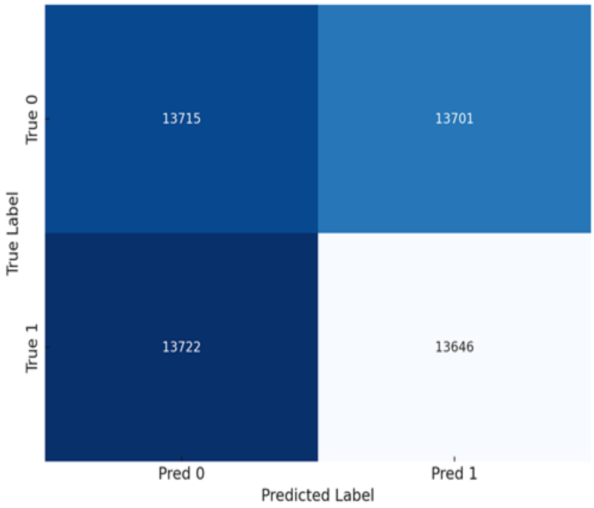

Fig. 5. Confusion matrix.

6. FEATURE IMPORTANCE

Feature importance measures how much each feature contributes to a machine learning model's predictions. In a RF classifier, importance is determined by a feature's ability to reduce uncertainty and improve decision-making at each tree split [24]. The algorithm's decision trees identify patterns that best separate different classes, such as benign behavior and various threat types (e.g., DoS). Features that create the most impactful splits—those that effectively distinguish between classes—are considered more important. For example, if "time_since_last_packet" effectively differentiates threats from benign behavior, it will likely be selected early in the tree splits. Each tree in the RF leverages these features for decision-making, and the feature importance score reflects how often a feature is used across trees and how well it reduces prediction errors.

Table 4 and figure 6 summarize the feature importance results, while figure 7 shows how the cumulative importance increases as more features are added, highlighting their contribution to overall model performance.

Table 4. Details of FIA.

Feature	Importance
time_since_last_packet	0.5605958025232953
wlan.duration	0.23993033152466678
frame.len	0.07674405004321838
ip.ttl	0.04358521396204749
udp.length	0.038300408301054516

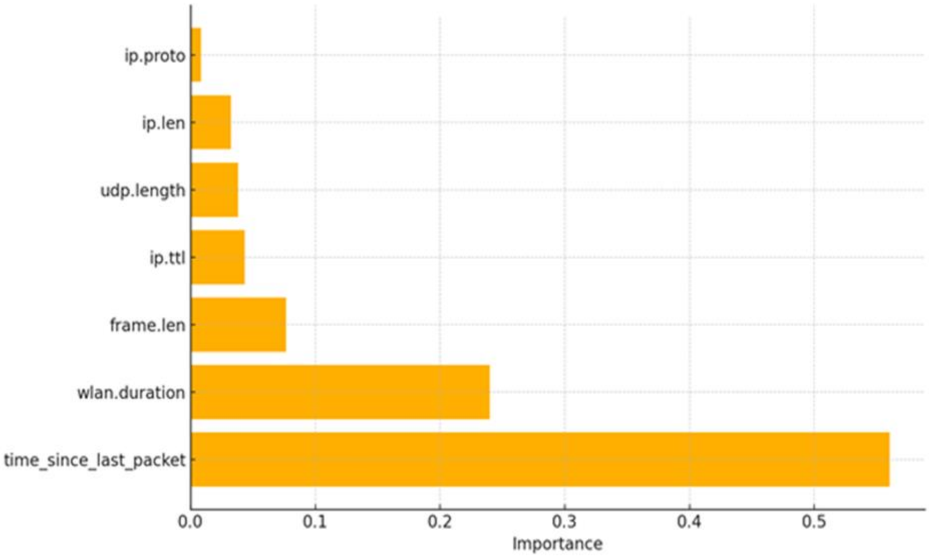

Fig. 6. The result of FIA.

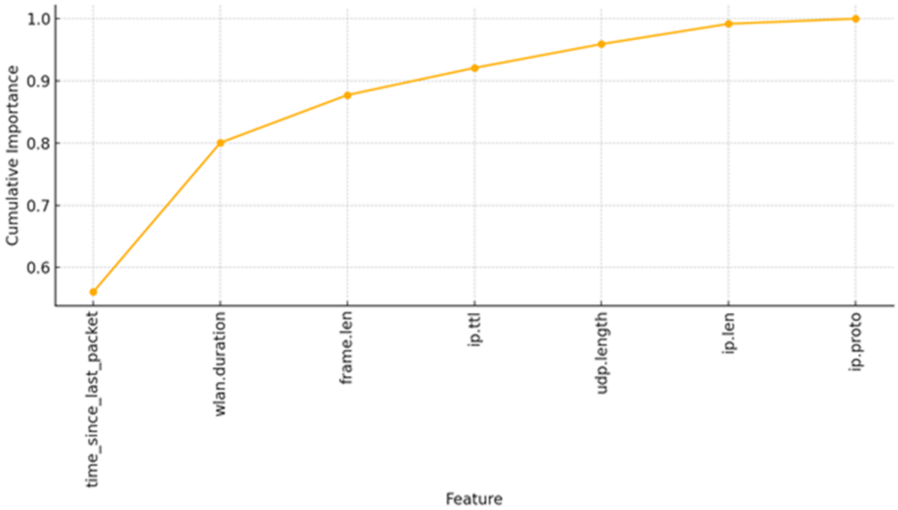

Fig. 7. Cumulative feature importance.

This section examines how the top features contribute to multi-step threat prediction:

- **Time_since_last_packet**: The most important feature, indicating that packet timing plays a key role in classifying network traffic. Certain threats exhibit distinct packet arrival patterns that differ from normal traffic.
- **Wlan.duration**: The duration of a WLAN connection is significant, as malicious activities often involve abnormal connection durations or frequencies. For example, a DoS attack may involve prolonged connection attempts with minimal data exchange.
- **Frame.len**: Frame length represents packet size and helps distinguish between normal and malicious traffic. In threats like false data injection (FDI), frame sizes may deviate from typical benign traffic patterns.
- **Ip.ttl (Time to Live)**: TTL defines a packet's lifespan within the network. Irregular TTL values may indicate evasion attempts or obfuscation of a threat's origin.
- **Udp.length**: UDP packet size is another key feature. Threats like DoS or replay attacks may display unusual UDP packet sizes or frequencies, signaling potential malicious activity.

Table 5 and figure 8 summarize the feature importance results, illustrating how each feature enhances the model's ability to predict the next threat step.

Table 5. The results of prediction after feature importance implementation.

Metric	Value
Accuracy (%)	99.33999999999999
Precision (%)	98.8199398566864
Recall (%)	99.3248234507795
F1-Score (%)	99.07173841835461
Error Rate (%)	0.6600000000000108
AUC Score	0.99

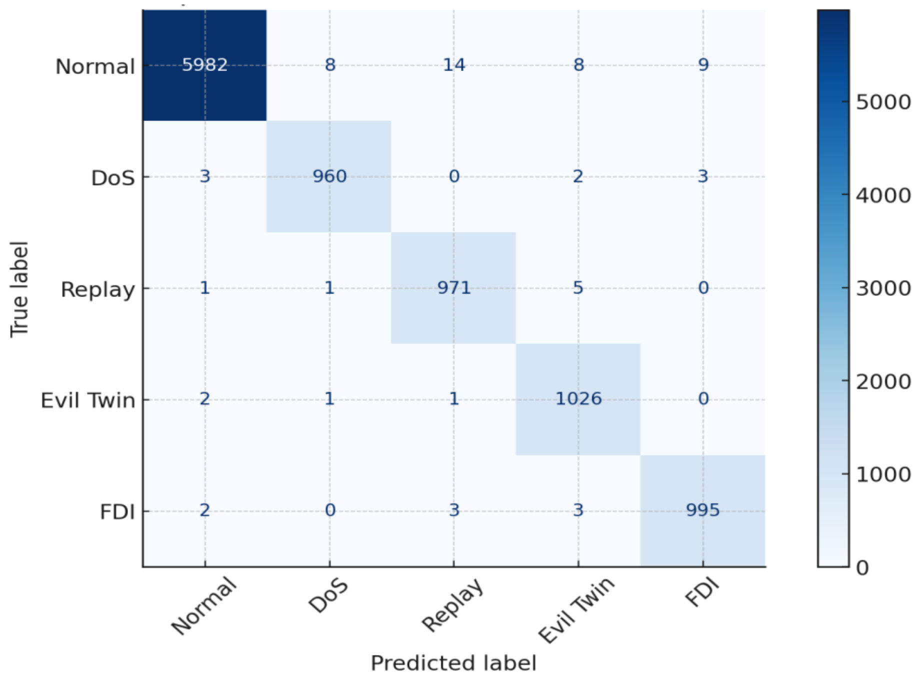

Fig. 8. Confusion matrix after feature importance implementation.

These results demonstrate the effectiveness of using feature importance in predicting multi-step UAV cyber threats. Table 6 presents the confusion matrix, detailing the model's performance across five threat classes: normal, DoS, Replay, Evil Twin, and FDI. This matrix provides valuable insights into how well the model differentiates between threat types and normal behavior, further validating its predictive capabilities.

Table 7 illustrates the metric comparison of the baseline DRL model and the improved model by feature importance.

Table 6. Details of confusion matrix after feature importance implementation.

Class	True Positives	False Positives	False Negatives
Normal	5982	35	18
DoS	960	10	5
Replay	971	7	6
Evil Twin	1026	4	5
FDI	995	8	5

Table 7. Metric comparison of baseline and improved model.

Metric	Baseline DRL Model (%)	Improved DRL Model (%)	Change (%)
Accuracy	96.5	99.34	+2.84%
Precision	94.2	98.82	+4.62%
Recall	95.8	99.32	+3.52%
F1-Score	95.0	99.07	+4.07%
Error Rate	3.5	0.66	-2.84%
AUC Score	0.98	0.99	+0.01

7. DISCUSSION

Our proposed model demonstrates the strong potential of DRL for predicting multi-step cyber threats in UAV systems. With 96.5% accuracy, 94.2% precision, and 95.8% recall, it outperforms traditional machine learning models like SVM and RF. These results indicate that the model not only delivers highly accurate predictions but also minimizes false positives, ensuring timely threat detection. The F1-score of 95.0% highlights its balance between precision and recall, while the AUC score of 0.98 reinforces its ability to distinguish between different threat sequences. Unlike traditional models, our reinforcement learning framework continuously learns optimal strategies, adapting to evolving cyber threats. As the model encounters more data, it refines its predictions, improving performance. Additionally, focusing on the five most important features reduces noise and enhances interpretability. DRL is fundamentally different from traditional supervised learning models like SVM and RF in the way it processes sequential decision-making and long-term dependencies. DRL learns through interaction with the environment, refining its predictions over time-based on a reward-driven mechanism. In our model, the UAV's cybersecurity environment is formulated as a MDP. This dynamic learning process allows the DRL model to adapt in real-time to the evolution of advanced persistent threats. DRL captures the sequential nature of threats by maintaining a history of past attacks and using it to predict future steps. Our DRL-based model effectively learns the transition probabilities between different attack types, allowing it to anticipate the next move of an attacker. The Q-learning algorithm enables the model to assign different values to different attack transitions, ensuring that the model prioritizes high-risk scenarios. Moreover, DRL balances exploration (trying new predictions) and exploitation (leveraging learned attack patterns) to refine its decision-making process, leading to higher adaptability against evolving cyber threats.

A key strength of our approach is its ability to predict the next step in a multi-step threat sequence, enabling proactive defense strategies. This capability helps mitigate threats before they escalate. however, the model’s performance depends on the quality and diversity of training data. If the dataset lacks coverage of potential threats or changes over time, performance may decline. Future work could integrate online learning techniques to continuously update the model with new threat data. Our model has significant applications for UAV security, particularly in surveillance, delivery, and search-and-rescue operations. UAVs are vulnerable to threats like DoS, replay, FDI, and evil twin attacks, which can compromise system integrity and lead to mission failure. Predicting the next step in a threat sequence allows for real-time defensive actions to minimize damage. For example, integrating this model into UAV security systems can enhance threat detection and prevention. By forecasting the next attack, the model can trigger defensive responses such as reconfiguring communication channels, isolating compromised components, or switching to backup systems. This proactive approach is especially valuable in high-risk environments, where early intervention can prevent severe consequences. Furthermore, the public availability of the dataset used for training provides a benchmark for researchers and developers in UAV cybersecurity, fostering innovation in this field. The fusion of cyber and physical data, as demonstrated in our model, enhances UAV resilience against complex cyber threats. This approach could also be extended to other critical infrastructure systems, where predicting cyber threats can reduce real-world risks. In conclusion, our DRL-based model offers a promising solution for predicting and mitigating multi-step UAV cyber threats. Leveraging reinforcement learning and advanced threat prediction, significantly enhances UAV security, providing proactive defense against evolving attacks. Future research could focus on improving adaptability to new threats and incorporating real-time learning to further enhance performance in dynamic environments.

8. CONCLUSION

In this paper, we introduced a novel prediction model for multi-step cyber threats on UAVs, using DRL techniques. By leveraging a comprehensive dataset that integrates both cyber and physical features of UAVs under normal and threat conditions, we demonstrated the model's ability to accurately predict the next step in an ongoing threat sequence. Our experimental results confirmed that the proposed model outperforms traditional machine learning-based approaches in terms of accuracy, precision, recall, F1-score, and AUC, emphasizing the power of DRL in predicting cyber threats for UAV systems. The fusion of cyber and physical features enables the model to make more informed predictions, providing a solid foundation for proactive defense strategies against evolving threats. The model's capacity to predict threat sequences—particularly for DoS, replay, FDI, and evil twin threats—opens new doors for UAV security. By anticipating the next threat step, the system can trigger countermeasures in real-time, preventing the escalation of cyber threats. The positive results of our experiments, along with the public availability of the dataset, make this work a meaningful contribution to the field of UAV cybersecurity.

While the model demonstrates impressive performance, there are several promising avenues for future research to enhance its capabilities. One potential direction is incorporating additional features, such as environmental data, GPS information, or real-time system feedback, which could improve predictive accuracy. Expanding the model to address a broader range of threat types, including APT and zero-day threats, would increase its robustness in real-world applications.

Additionally, deploying the model in live UAV systems would offer valuable insights into its performance under dynamic, real-world conditions, where both cyber and physical factors evolve continuously. This would provide opportunities to refine the model’s response times and adaptability to new threat strategies.

Future research could also focus on integrating online learning techniques, allowing the model to update continuously as new threat patterns and data emerge. This would ensure that the model remains relevant and capable of adapting to the ever-changing cyber threat landscape. In our approach, the model is trained on static datasets, meaning that their effectiveness may degrade as new cyber threats emerge. Online learning offers a solution by allowing the model to continuously update its parameters based on newly observed threat data. The model adapts to real-time variations in attack strategies without requiring full retraining. Moreover, it reduces computational overhead by processing incremental data updates rather than relying on large-scale batch training. One promising technique is incremental reinforcement learning, where the model periodically refines its threat detection policy by incorporating feedback from real-world UAV security logs. This ensures that the model remains effective against zero-day threats and novel attack patterns. Another critical step in improving model performance is ensuring that the dataset used for training is comprehensive and representative of real-world UAV cybersecurity threats.

In conclusion, our DRL-based prediction model marks a significant step forward in enhancing UAV cybersecurity. By predicting the next step in multi-step cyber threats, it offers a proactive defense approach, enabling UAV systems to better withstand a growing array of cyber threats. With continued improvements and research, this model could become an essential component of future UAV security infrastructure.

CONFLICT OF INTERESTS

The authors declare that they have no conflict of interest.

REFERENCES

[1]M. Navabi and F. Malekpour, “Satellite status control using tabulation gain controller in a variable parameter system,” *Journal of Space Science and Technology*, vol. 15, no. 2, pp. 15-25, 2022, (in Persian), https://doi.org/10.30699/jsst.2021.244891.1309.

[2] R. Ghasrizadeh and A. A. Nikkhah, “Improved spoofing loosely coupled INS /GPS with steady state Kalman matrix gain,” *Journal of Space Science and Technology*, vol. 16, no. 3, pp. 37-49, 2023, (in Persian), https://doi.org/10.30699/jsst.2023.1425.

[3] M. Ebrahimi Kachoie, M. Arbabmir, and M. Norouz, “A survey on vision navigation methods for UAV navigation applications,” *Journal of Space Science and Technology*, vol. 10, no. 2, pp. 33-52, 2017, (in Persian).

[4] M. Dehghan and E. Khosravian, “Advancing situation awareness systems: Evaluating decision-making methods with UAV applications,” *Management Strategies and Engineering Sciences*, vol. 6, no. 4, pp. 122-133, 2024, https://doi.org/10.61838/msesj.6.4.13.

[5] C. Rani, H. Modares, R. Sriram, D. Mikulski, and F. L. Lewis, “Security of unmanned aerial vehicle systems against cyber-physical attacks,” *The Journal of Defense Modeling and Simulation: Applications, Methodology, Technology*, vol. 13, no. 3. pp. 331-342, 2015, https://doi.org/10.1177/1548512915617252.

[6] M. Dehghan and B. Sadeghiyan, “Privacy-preserving collision detection of moving objects,” *Transactions on Emerging Telecommunications Technologies*, vol. 30, no. 3, 2019, Art. no. e3484, https://doi.org/10.1002/ett.3484.

[7] M. Dehghan, B. Sadeghiyan, and E. Khosravian, “Secure multi-party collision resolution protocol for air traffic control,” *Journal of Intelligent & Fuzzy Systems*, vol. 38, no. 4, pp. 4205-4221, 2020, https://doi.org/10.3233/JIFS-190675.

[8] Z. Yu, Z. Wang, J. Yu, D. Liu, H. Herbert Song, and Z. Li, “Cybersecurity of unmanned aerial vehicles: a survey,” *Aerospace and Electronic Systems Magazine*, vol. 39, no. 9, pp. 182-215, 2024, https://doi.org/10.1109/MAES.2023.3318226.

[9] S. C. Hassler, U. A. Mughal, and M. Ismail, “Cyber-physical intrusion detection system for unmanned aerial vehicles,” *Transactions on Intelligent Transportation Systems*, vol. 25, no. 6, pp. 6106-6117, 2024, https://doi.org/10.1109/TITS.2023.3339728.

[10] M. Dehghan and E. Khosravian, “A review of cognitive UAVs: AI-driven situation awareness for enhanced operations,” *AI and Tech in Behavioral and Social Sciences*, vol. 2, no. 4, pp. 54-65, 2024, https://doi.org/10.61838/kman.aitech.2.4.6.

[11] B. S. Sarıkaya and Ş. Bahtiyar, “A survey on security of UAV and deep reinforcement learning,” *Ad Hoc Networks*, vol. 164, 2024, Art. no. 103642, https://doi.org/10.1016/j.adhoc.2024.103642.

[12] S. Niyonsaba, K. Konate, and M. M. Soidridine, “Deep learning based intrusion detection for cybersecurity in unmanned aerial vehicles network,” in *4th International Conference on Electrical, Computer and Energy Technologies (ICECE)*, Sydney, Australia, 2024.

[13] D. Javeed, T. Gao, P. Kumar, S. Shoukat, I. Ahmad, and R. Kumar, “An intelligent and interpretable intrusion detection system for unmanned aerial vehicles,” in *International Conference on Communications (ICC)*, Denver, CO, USA, 2024, pp. 1951-1956, https://doi.org/10.1109/ICC51166.2024.10622703.

[14] A. Alzahrani, “Novel approach for intrusion detection attacks on small drones using ConvLSTM model,” *IEEE Access*, vol. 12, pp. 149238-149253, 2024, https://doi.org/10.1109/ACCESS.2024.3471806.

[15] M. Dehghan and E. Khosravian, "Private Federated Learning for APT detection in internet of drones," *Karafan Journal*, vol. 20, no. 3, pp. 465-484, 2023, (in Persian), https://doi.org.10.48301/kssa.2023.409787.2649.

[16] M. Rizwanullah *et al.*, "Modelling of metaheuristics with machine learning-enabled cybersecurity in unmanned aerial vehicles" *Sustainability*, vol. 14, no. 24, 2022, Art. no. 16741, https://doi.org/10.3390/su142416741.

[17] M. Dehghan and B. Sadeghiyan, "Secure multi-party sorting protocol based on distributed oblivious transfer," in *10th International Conference on Computer and Knowledge Engineering (ICCKE)*, Mashhad, Iran, 2020, pp. 011-017, 10.1109/ICCKE50421.2020.9303630.

[18] K. Arulkumaran, M. P. Deisenroth, M. Brundage, and A. A. Bharath, "Deep reinforcement learning: a brief survey," *Signal Processing Magazine*, vol. 34, no. 6, pp. 26-38, 2017, https://doi.org/10.1109/MSP.2017.2743240.

[19] M. Dehghan, B. Sadeghiyan, E. Khosravian, A. S. Moghaddam, and F. Nooshi, "ProAPT: Projection of APT threats with deep reinforcement learning," *arXiv:2209.07215*, 2022, https://doi.org/10.48550/arXiv.2209.07215.

[20] V. François-Lavet, P. Henderson, R. Islam, M. G. Bellemare, and J. Pineau, "An introduction to deep reinforcement learning," *Foundations and Trends® in Machine Learning*, vol. 11, no. 3-4, pp. 219-354, 2018, http://dx.doi.org/10.1561/2200000071.

[21] Z. Ding, Y. Huang, H. Yuan, and H. Dong, "Introduction to Reinforcement Learning," in *Deep Reinforcement Learning: Fundamentals, Research and Applications*, H. Dong, Z. Ding, and S. Zhang, Eds. Singapore: Springer Singapore, 2020, pp. 47-123, https://doi.org/10.1007/978-981-15-4095-0_2.

[22] J. S. Bergstra, R. Bardenet, Y. Bengio, and B. Kégl, "Algorithms for hyper-parameter optimization," in *Advances in neural information processing systems*24 *(NeurIPS 2011)*, J. Shawe-Taylor, R. Zemel, P. Bartlett, F. Pereira, and K. Weinberger, Eds. Curan Associates, Inc., 2011, pp. 2546-2554.

[23] D. V. Carvalho, E. M. Pereira, and J. S. Cardoso, "Machine learning interpretability: A survey on methods and metrics," *Electronics*, vol. 8, no. 8, 2019, Art. no. 832, https://doi.org/10.3390/electronics8080832.

[24] M. Saarela and S. Jauhiainen, "Comparison of feature importance measures as explanations for classification models," *SN Applied Sciences*, vol. 3, 2021, Art. no. 272, https://doi.org/10.1007/s42452-021-04148-9.

JSST
Journal of Space Science and Technology

P-ISSN: 2008-4560
E-ISSN: 2423-4516

Journal of Space Science and Technology

Vol. 18, Special Issue, pp. 16-25, 2025
https://doi.org/10.22034/jsst.2024.468738.1493
Journal Homepage: https://www.jsstpub.com

Original Research Paper

Plasma-Based Beamforming Antennas

Fatemeh Sadeghikia*, Mahmoud Talafi Noghani, Ali Karami Horestani, and Fatemeh Zamani

Aerospace Research Institute, Ministry of Science, Research and Technology, Tehran, Iran

ARTICLE INFO

Article History:

Received 20 July 2024
Revised 07 December 2024
Accepted 22 December 2024
Available Online 22 January 2025

Keywords:

Plasma antenna
Beamforming antenna
Space communication antenna
Plasma reflector

ABSTRACT

In this article, beamforming methodologies for antennas are first reviewed, highlighting the pros and cons of each method. It is observed that each method offers unique advantages and limitations. Some of the key technologies used to provide beamforming antennas are also compared with consideration of complexity, beamwidth, price, scanning angle, frequency range, beamforming speed, and accuracy. It is shown that beamforming using plasma offers flexibility compared to other techniques while remaining relatively cost-efficient. Moreover, using plasma components, it is possible to conceal the entire antenna or parts of it. Based on these advantages, this study presents a low-complexity, low-cost plasma-based antenna for beamforming. This novel antenna combines an axial mode helical antenna surrounded by circular arrays of plasma elements, forming plasma cups around the helix. The power to energize the plasma elements is supplied by a set of converters and switches. The state of each switch is independently managed by a microcontroller, thereby enabling plasma elements to be individually switched ON or OFF. The plasma cups are used to control the direction and width of the radiated beam of the helix. Activation of a plasma cup enhances the beamwidth of the helix, while asymmetrically activated configurations allow for steering the end-fire beam pattern up to ±27°. The height of the plasma cups is smaller than the height of the helix, ensuring no increase in the overall height of the antenna. A prototype of the proposed antenna structure has been fabricated based on commercially available tools, and measurements for different configurations of the plasma reflectors have been carried out. The concept and computational results have been validated by the strong agreement between the simulation and measurement results. The proposed antenna offers a cost-effective solution for scanning and target acquisition in space communications and radar systems.

---

*Corresponding Author's E-mail: Sadeghi_kia@ari.ac.ir

How to Cite this Article:
F. Sadeghikia, M. Talafi Noghani, A. Karami Horestani, and F. Zamani, "Plasma-based beamforming antennas," *Journal of Space Science and Technology*, Vol. 18, Special Issue, pp. 16-25, 2025, https://doi.org/10.22034/jsst.2024.468738.1493.

1. INTRODUCTION

Antennas equipped with beamforming capabilities play an important role in wireless communication by providing dynamic control over signal directionality and shaping. These advanced antennas enhance the efficiency and reliability of wireless networks, optimizing signal transmission and reception. Beamforming technology has found widespread applications in various fields, including wireless networks, satellite communications, radar systems, and autonomous vehicles .

Numerous beamforming methods have been explored, each offering unique advantages and limitations [1-8]. Recent advancements in beamforming leverage novel materials with adjustable electromagnetic (EM) properties. Real-time adjustments of these materials enable dynamic control over antenna radiation characteristics, allowing precise manipulation of beam direction and shape. This approach is particularly valuable for applications requiring rapid and accurate beamforming, despite potential challenges related to bandwidth and steering.

In recent years, plasma materials have attracted significant attention due to their unique electromagnetic properties, that enable dynamic reconfigurability in antenna systems. Early studies, such as those by Borg et al. [9] and Rayner et al. [10], explored plasma as an efficient radiating element, demonstrating its potential for agile frequency control and tunability. Later, Anderson investigated plasma-based steerable antennas using the concept of plasma windowing [11], and Ja'afar et al. further implemented it at 4.9 GHz [12]. Subsequently, Wang et al. [13] modified the conventional plasma window antenna, transforming it into an end-fire plasma array antenna to enhance directional control. These studies highlighted the compactness and scalability of steerable plasma antennas but noted limitations such as narrow bandwidth and beam steering restricted to the azimuthal plane.

Malhat et al. [14] introduced a hybrid plasma-phased array system, combining electronic and plasma tuning mechanisms to achieve wide-angle steering, albeit with increased system complexity. More recent work by Mansutti et al. [15] and Magarotto et al. [16] explored intelligent reflective surfaces with enhanced steering precision, though these designs remain unimplemented and face practical challenges.

Building on these advancements, some of the authors previously proposed a 3D beam-steerable antenna [17,18] that utilizes a circular array of plasma reflectors in the form of a cup and an end-fire helical antenna. The design allows dynamic control of the beamwidth (37°–50°) and beam direction (±6° in 3D space) while maintaining structural simplicity and cost-effectiveness. However, the structure exhibits limitations in its steering range.

To address these limitations, this study proposes an improved design that introduces additional rows of plasma cups encircling the radiating helical antenna. As a result, it significantly enhances the steering range while preserving simplicity and affordability. The objective is to present this modified antenna and demonstrate its extended steering capabilities.

While the proposed design focuses on utilizing plasma materials for beamforming, it is important to compare this approach with other beamforming methods. By evaluating and contrasting these methods with plasma-based beamforming, the strengths and challenges of this innovative approach can be clearly understood. To this end, Section 2 provides a comparative analysis of different beamforming methods and technologies. Section 3 reviews the theoretical characteristics of plasma as an innovative technology for facilitating beamforming antennas. Section 4 presents a comprehensive investigation, including numerical simulations and experimental validations of a prototype beamforming antenna based on plasma material. Finally, Section 5 summarizes and concludes this study.

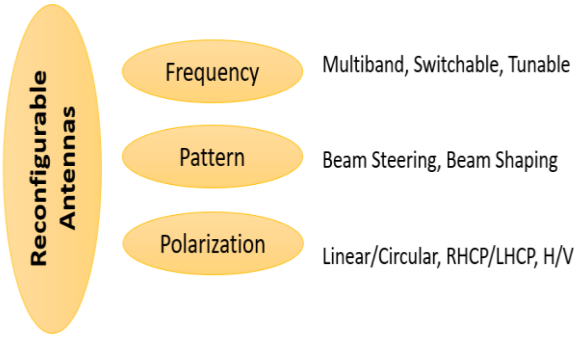

Fig. 1. Categorization of reconfigurable antennas.

2. BEAMFORMING METHODS

The rapid advancement of wireless technology has ignited a growing demand for versatile beamforming antennas. These antennas, valued for their reduced complexity and cost compared to traditional phased array systems, have gained significant attention in the ever-evolving landscape of wireless communication [19].

The term “reconfigurable antenna” refers to antennas designed to dynamically adjust parameters such as frequency, radiation pattern, or polarization, as depicted in Fig. 1. In the realm of space communication antennas, beamforming methods play a critical role in enabling efficient communication between ground stations and satellites or spacecraft. Specifically, an antenna falls into the category of beamforming antennas when it is capable of dynamically shaping or steering the radiation pattern to focus energy in desired directions, thereby enhancing communication performance.

Beamforming antennas contribute significantly to the success of both 5G, 6G, and satellite communications by optimizing signal transmission, enhancing network capacity, and adapting to the dynamic requirements of modern communication systems.

As depicted in Fig. 2, notable innovations have emerged to produce beamforming antennas. These innovations include electrical methods involving switches in the antenna structure, optical methods using photoconductive materials, structural alterations in the antenna configuration, and the incorporation of novel materials such as ferrites and plasmas into the antenna structure [23-26].

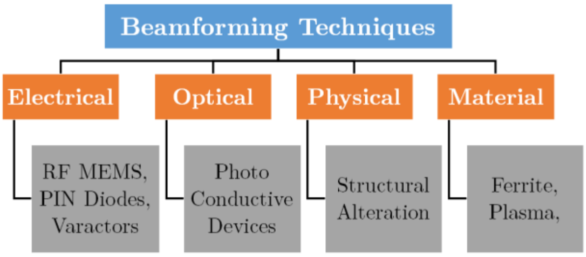

Fig. 2. Beamforming methods in antennas.

Table 1. Comparison between the features of beamforming methods in antennas: L (Low), M (Medium), H (High), and V (Variable).

Method Feature	Electrical	Optical	Physical	Material based
Response time	V	L	H	M
Stability	H	V	V	V
Complexity	M	L	M	M
Price	V	M	M	V
Power consumption	M	L	M	L

Table 2. Comparison between different technologies of beamforming.

Technology	Complexity	Beamwidth	Price	Scanning Angle	Frequency Range	Velocity of Steering	Accuracy
Phased Array Antennas	Moderate to High	Fixed	High	Wide	Wide	Fast	High
Metamaterial Antennas	High	Fixed	Can vary	Limited	Wide	Moderate	High
Liquid Crystal Antennas	Moderate	Flexible	Moderate	Limited	Limited	Moderate	Moderate
Plasma Antennas	Moderate	Flexible	Low	Wide	Wide	Fast	Moderate

A comparative analysis between the beamforming methods in antennas is presented in Table 1, utilizing acronyms to denote the levels of Low (L), Medium (M), and High (H). In this table, the reconfigurability of electrical, optical, physical, and material-based methods is highlighted, with considerations for response time, stability, complexity, price, and power consumption. This comparison provides insights into the trade-offs associated with different approaches, guiding the selection of an appropriate method based on specific application requirements.

For better understanding, some of the key technologies to provide beamforming antennas, including phased array antennas [27-30], metamaterial-based structures [31,32], liquid crystal-based antennas [33–36], and antennas based on plasma material [37-44], are compared and the results are presented in Table 2. The comparison considerations include complexity, beamwidth, price, scanning angle, frequency range, beamforming speed, and accuracy in this table.

Each technology offers unique advantages and limitations. For instance, phased arrays provide fast and precise beam steering but suffer from fixed beamwidth, high complexity and cost, and susceptibility to grating lobes [45] and [46]. As a specific implementation of phased arrays, Butler matrix-based beamforming networks [47] offer a compact and efficient solution for mm-wave beam-steering, achieving wide scanning angles (~94°) and moderate beamwidths; however, they are more suitable for applications in high-frequency ranges (e.g. Ka-band) and face challenges related to broadband impedance matching, fixed beamwidth, and practical robustness.

Metamaterial-based structures utilize engineered artificial materials with extraordinary EM properties but face complexity in design, fabrication, and integration with practical systems and usually limited operating bandwidth [48].

Liquid crystal-based antennas provide another method for beamforming, utilizing the properties of liquid crystals to dynamically control the radiation pattern and polarization of the antenna. This technology offers advantages such as relatively fast response time and low power consumption. However, challenges include complexity in driving mechanisms and limited scanning angle and bandwidth compared to other methods [49].

Beamforming using plasma offers flexibility compared to other techniques while remaining relatively cost-efficient. An additional advantage is that plasma components can be electrically switched ON/OFF, allowing the entire antenna or parts of it to be concealed [50-57]. Based on these advantages, the following section presents the concept of plasma technology, and subsequently, a plasma-based beamforming antenna is introduced.

3. PLASMA TECHNOLOGY CONCEPT

To investigate the effect of plasma media on the radiation characteristics of antennas, it’s essential to understand some basic properties of plasma. The complex permittivity ε_p of an isotropic plasma, which is a dispersive medium, under low-pressure conditions, can be modeled as [50-51]:

$$\frac{\varepsilon_p}{\varepsilon_0} = 1 - \frac{\omega_p^2}{\omega^2 + j\omega\upsilon} \qquad (1)$$

where ω is the operating angular frequency in rad/s, ν is the electron-neutral collision frequency in Hz, ε_0 is the free-space permittivity, and ω_p is the plasma angular frequency in rad/s, defined as [58]:

$$\omega_p = \sqrt{\frac{ne^2}{m\varepsilon_0}} \qquad (2)$$

Here, n represents the electron density in m^{-3}, e is the charge of the electron, and m is the electron mass in Kg.

It is important to note that the plasma frequency can be adjusted by altering plasma characteristics such as density, allowing adjustment of the frequency band in which the plasma operates as a dielectric or as a conductor. For instance, for an incident EM wave with a frequency greater than the plasma frequency, the plasma medium behaves as a dielectric with positive permittivity, allowing the propagation of the incident wave through plasma.

Conversely, at frequencies lower than the plasma frequency, the plasma exhibits negative permittivity, prohibiting the propagation of the EM wave. At frequencies significantly lower than the plasma frequency, the plasma medium can act as a conductor, albeit not a very good one.

The electrical conductivity σ of plasma is determined by [50]:

$$\sigma = \left(\frac{\varepsilon_0 \upsilon \omega_p^2}{\upsilon^2 + \omega^2}\right) - j\left(\frac{\varepsilon_0 \omega \omega_p^2}{\upsilon^2 + \omega^2}\right) \qquad (3)$$

This relation shows that the electrical conductivity of a plasma medium at a specific operating frequency can also be controlled by varying the plasma frequency, or collision frequency. The loss tangent tanδ of the plasma can be derived from the ratio of the imaginary part of plasma permittivity to its real part as [58]:

$$\tan\delta = \frac{\mathrm{Im}(\varepsilon_p)}{\mathrm{Re}(\varepsilon_p)} = \frac{-(\frac{\omega_p^2 \nu}{\omega(\omega^2+\nu^2)})}{(1-\frac{\omega_p^2}{\omega^2+\nu^2})} = -\frac{\nu\omega_p^2}{\omega(\omega^2+\nu^2-\omega_p^2)} \qquad (4)$$

This expression indicates that plasma loss is influenced by the plasma parameters, and changes at different operating and plasma frequencies.

4. CASE STUDY

To demonstrate the potential of plasma in beamforming applications, this section presents a flexible and cost-efficient beamforming antenna based on plasma technology. The antenna can both steer the radiated beam and control its beamwidth. The first part of this section details the structure of the antenna. This is followed by the numerical study of the radiation characteristics of the antenna, and then the experimental validation is presented.

4.1 Antenna Structure

The antenna configuration, shown in Fig. 3(a), consists of an axial mode helical antenna which is surrounded by two concentric plasma cups. As shown in the figure, each plasma cup is formed by a dense array of U-shaped plasma tubes. Plasma media can generally be created by ionizing a gas using methods such as DC biasing, RF excitation, or microwave ionization [44]. In this study, the power to energize the plasma tubes is supplied by a set of electrical ballasts functioning as converters, while each converter is connected to a switch. The state of each switch is independently managed by a microcontroller, thereby enabling plasma tubes to be individually switched ON or OFF. Figure 3(b) illustrates the block diagram of this control setup, showing the plasma tubes and the corresponding electronic devices.

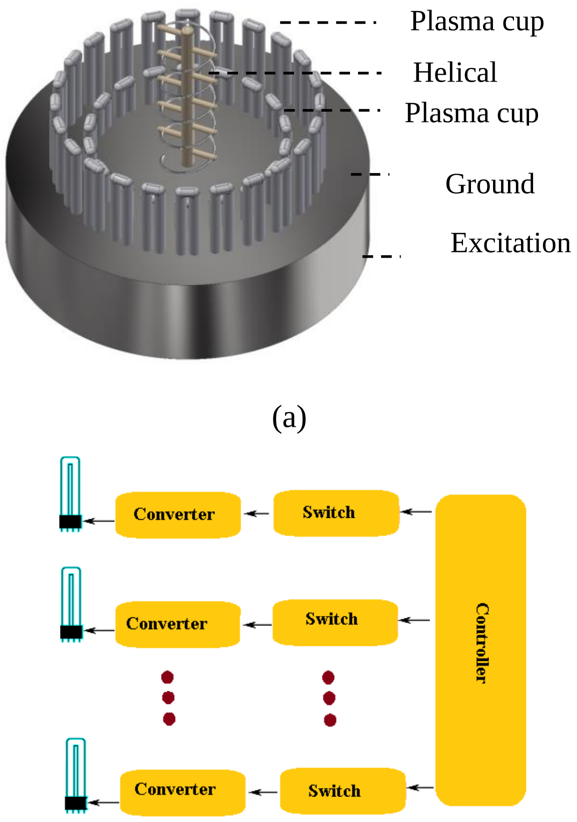

(a)

(b)

Fig. 3. (a) Three-dimensional view and the details of the antenna with two plasma cups, (b) Block diagram of the controlling circuit of plasma tubes.

The plasma and collision frequencies of the tubes are respectively f_p = 7.8 GHz and ν = 1 GHz. Note that, in this study, energizing half of the adjacent plasma elements, known as “half-cup”, is what steers the radiated beam of the helical antenna. Dimensions of the half-cup, including its height (H_C) and diameter (D_C), are crucial in the determination of the steering range.

Dimensions of the helical section of the antenna for operating at a center frequency of 927 MHz are as follows: Diameter D_{Helix} = 114 mm (0.35λ), pitch angle α = 13.6°, height H_{Helix} = 544 mm (1.68λ), and N = 6.25 turns. The ground plane diameter is D_g = 480 mm**.**

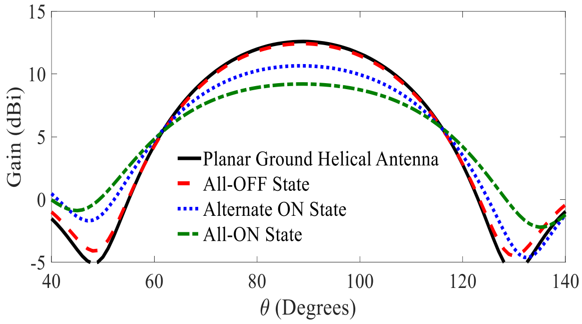

Fig. 4. Simulated radiation gain of the helical antenna surrounded by a single plasma cup.

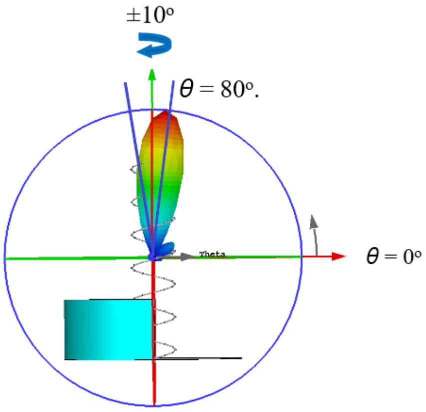

Fig. 5. Simulated ultimate steered radiated beam of one plasma half-cup around the helical antenna.

4.2 Numerical Investigation

A commercial full-wave numerical modeling tool based on the finite difference time domain (FDTD) method is used to assess the performance of the proposed antenna. Numerical EM simulations of the helical antenna with a ground plane (without plasma cups), serving as the reference antenna, reveal a radiation gain of approximately 12.6 dBi and a half-power beamwidth (HPBW) of 38.7° at θ = 90°. As was discussed previously in [17] and [18], a single plasma cup controls the beamwidth of the helical antenna. Figure 4 illustrates the radiated gain of the antenna with different numbers and arrangements of activated plasma elements when the height H_{c1} = 160 mm (~ 0.5 λ) and diameter D_{c1} = 330 mm (~ λ). When all elements are turned off (All-OFF state), a relatively narrow (38.7°) radiated beam identical to the beam of the helical antenna is observed. Activating all plasma elements (All-ON state) widens the beam from 38.7° to 50.3°. Intermediate activation (Alternate state) yields a beamwidth between the All-OFF and All-ON states. Generally, increasing the number of activated plasma elements widens the beam.

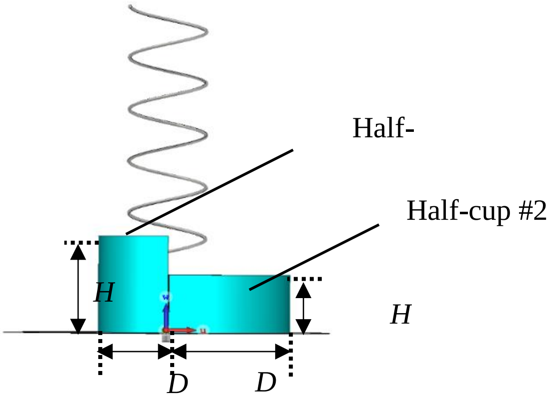

Fig. 6. Details of the antenna, while two plasma half cups with different diameters and heights are excited in opposite directions.

Unsymmetrical activation of the cup elements (resulting in a half-cup) steers the radiated beam of the helix, as depicted in Fig. 5, and alters the direction of its radiated beam within a solid angle of up to ±10 degrees. This mode allows for steering the antenna beam in the end-fire direction, with the scanning angle determined by the height and radius of the plasma cup. However, utilizing only one half-cup restricts the steering range. To enhance it, a second plasma half-cup positioned opposite the initial one, as illustrated in Fig. 6 is used. This configuration effectively modifies the direction of the radiated beam. Fig. 7 illustrates the simulated pattern of the helical antenna using two half-cups for H_{C1} = 0.5 λ, D_{C1} = 0.5 λ, H_{C2} = 1.3 λ and D_{C2} = 1.05 λ. The results show ±27° steering in the radiation pattern. The results presented in [42] examine the influence of the dimensions of the second half-cup on the radiation characteristics of this antenna.

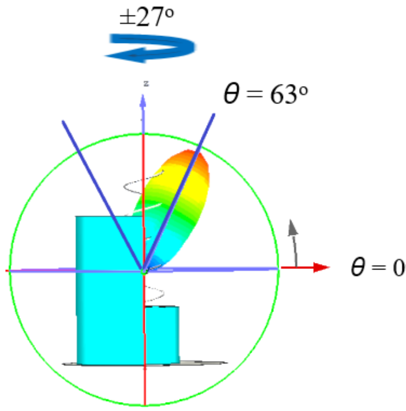

Fig. 7. The simulated radiation pattern of the antenna with two plasma haf-cups for HC1 = 0.5 λ, DC1 = 0.5 λ, HC2 = 1.3 λ and DC2 = 1.05 λ.

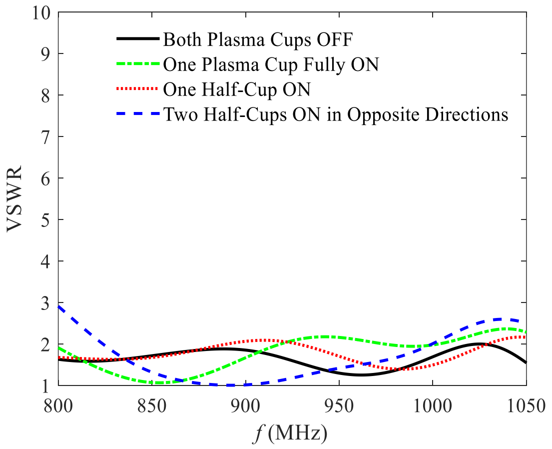

Fig. 8. Simulated VSWR of the antenna across different configurations of the plasma cup reflectors.

Although the utilized helical antenna is inherently designed to operate over a wide frequency range with good impedance matching due to its structural features, it is important to investigate the effects of the plasma reflectors on the impedance matching of the antenna. To this aim, Fig. 8 illustrates the effects of the plasma reflectors under four different configurations on the Voltage Standing Wave Ratio (VSWR) graph of the antenna: *a*) both plasma cups OFF, *b*) one plasma cup fully ON, *c*) one half-cup ON, and *d*) two half-cups ON in opposite directions. The results show minimal variation in VSWR across different scenarios because the plasma reflectors handle only small current densities.

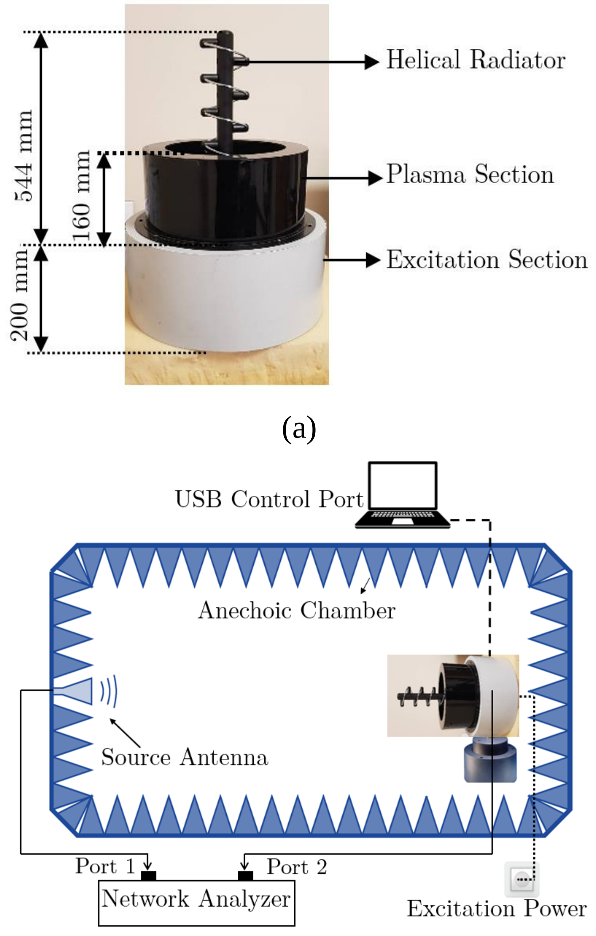

(a)

(b)

Fig. 9. (a) Fabricated prototype antenna using a single plasma cup and details of its dimensions, (b) measurement setup.

5. EXPERIMENTAL VALIDATION

For experimental validation, a prototype of the proposed antenna using a single plasma cup for operation at a frequency of f = 927 MHz is fabricated, as shown in Fig. 9. The height and diameter of the first plasma cup are H_{c1} = 160 mm and D_{c1} = 330 mm, respectively. The height and diameter of the second cup are set to H_{c2} = 0 mm and D_{c2} = 0 mm. The measurements are performed in an anechoic chamber with a peak gain accuracy better than 0.5 dBi within the operating frequency range of the antenna. The measurement setup is illustrated in Fig. 9(b). In this setup, two connections for energizing the excitation section of the antenna and also a USB port as a user interface are illustrated.

A series of measurements are conducted, and a comparison between the simulated and measured results is presented.

Figure 10 compares the simulated and measured radiation gain of the antenna for various plasma reflector configurations, showing good agreement between simulated and measured results. In summary, the proposed method for beamwidth control and beam steering using a reflector in the form of a plasma cup is validated both numerically and experimentally.

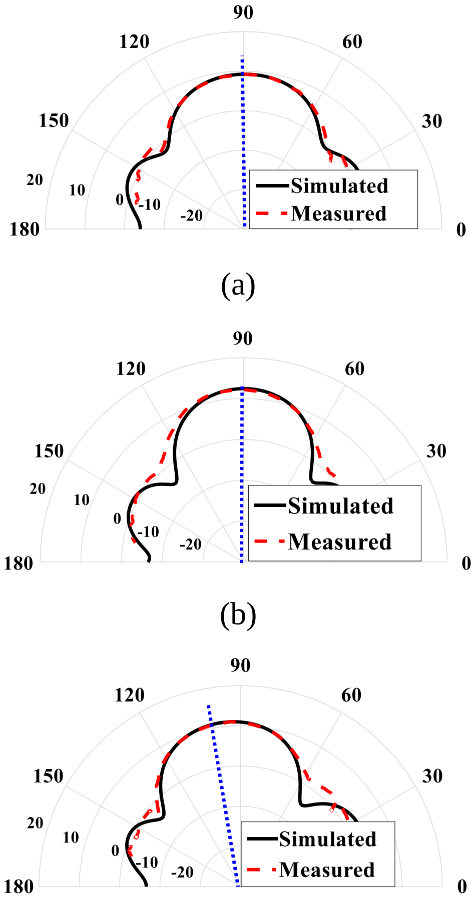

(a)

(b)

(c)

Fig. 10. Comparison between the simulated and measured radiation gain of the antenna in different modes: (a) ALL-ON states, (b) ALL-OFF states, (c) Half-cup.

6. CONCLUSION

In this paper, dynamic beamforming of the radiated beam from a helical antenna has been demonstrated. it has been shown through full-wave EM simulations that plasma cups around the helical antenna can electronically alter both the direction and width of the radiated beam. Asymmetrically activated configurations allow for steering the end-fire beam pattern of the helical antenna up to 54°.

A prototype has been fabricated and tested in L-band frequency, validating the concept and computational results through good agreement between simulation and measurement data. This cost-effective method offers the potential for scanning and detecting targets in space communications and radar systems, utilizing the versatility of plasma materials

CONFLICT OF INTERESTS

The authors declare that they have no conflict of interest

REFERENCES

[1] H. T. Chou, "Equivalent orthogonal beam steering for fast determination of reactions between two phased arrays of antennas with analog beamforming networks for maximum wireless power transfer," *IEEE Transactions on Antennas and Propagation*, vol. 69, no. 12, pp. 8449-8460, 2021, https://doi.org/10.1109/TAP.2021.3090517.

[2] A. Raeesi, A. Palizban, A. Ehsandar, H. Al-Saedi, S. Gigoyan, and W. M. Abdel-Wahabet, "A low-profile 2D passive phased-array antenna-in-package for emerging millimeter-wave applications," *IEEE Transactions on Antennas and Propagation*, vol. 71, no. 1, pp. 1093-1098, 2023, https://doi.org/10.1109/TAP.2022.3207203.

[3] D. Kozlov, I. Munina, P. Turalchuk, V. Kirillov, A. Shitvov, and D. Zelenchuk, "Characterization of tiled architecture for C-Band 1-Bit beam-steering transmitarray," *Sensors*, vol. 21, no. 4, 2021, Art. no. 1259, https://doi.org/10.3390/s21041259.

[4] Q. Ali *et al.*, "Recent developments and challenges on beam steering characteristics of reconfigurable transmitarray antennas," *Electronics*, vol. 11, no. 4, 2022, Art. no. 587, https://doi.org/10.3390/electronics11040587.

[5] T. Ohira and K. Iigusa, "Electronically steerable parasitic array radiator antenna," *Electronics and Communications in Japan (Part II: Electronics)*, vol. 87, no. 10, pp. 25-45, 2004, https://doi.org/10.1002/ecjb.20081.

[6] H. Kawakami and T. Ohira, "Electrically steerable passive array radiator (ESPAR) antennas," *IEEE Antennas and Propagation Magazine*, vol. 47, no. 2, pp. 43-50, 2005, https://doi.org/10.1109/MAP.2005.1487777.

[7] M. Boyarsky, T. Sleasman, M. F. Imani, J. N. Gollub, and D. R. Smith, "Electronically steered metasurface antenna," *Scientific Reports*, vol. 11, 2021, Art. no. 4693, https://doi.org/10.1038/s41598-021-83377-9. .

[8] M. S. Rabbani, J. Churm, and A. P. Feresidis, "Continuous beam-steering low-loss millimeter-wave antenna based on a piezo-electrically actuated metasurface," *IEEE Transactions on Antennas and Propagation*, vol. 70, no. 4, pp. 2439-2449, 2022, https://doi.org/10.1109/TAP.2021.3137248.

[9] G. G. Borg *et al.*, "Plasmas as antennas: Theory, experiment and applications," *Physics of Plasmas*, vol. 7, no. 5, pp. 2198–2202, 2000, https://doi.org/10.1063/1.874041.

[10]J. P. Rayner, A. P. Whichello, and A. D. Cheetham, "Physical characteristics of plasma antennas," *IEEE Transactions on Plasma Science*, vol. 32, no. 1, pp. 269–281, 2004, https://doi.org/10.1109/TPS.2004.826019.

[11]T. Anderson, *Plasma Antennas*, 2nd ed. United Kingdom: Artech House, 2021.

[12]H. Ja'afar, M. T. B. Ali, A. N. B. Dagang, H. M. Zali, and N. A. Halili, "A reconfigurable monopole antenna with fluorescent tubes using plasma windowing concepts for 4.9-GHz application," *IEEE Transactions on Plasma Science*, vol. 43, no. 3, pp. 815–820, 2015, https://doi.org/10.1109/TPS.2015.2398878.

[13]C. Wang, W. Shi, B. Yuan, and J. Mao, "Pattern-Steerable Endfire Plasma Array Antenna," *IEEE Transactions on Antennas and Propagation*, vol. 69, no. 10, pp. 6994-6998, 2021, https://doi.org/10.1109/TAP.2021.3070181.

[14]H. A. E. A. Malhat, M. M. Badawy, S. H. Zainud-Deen, and K. H. Awadalla, "Dual-mode plasma reflectarray/ transmitarray antennas," *IEEE Transactions on Plasma Science*, vol. 43, no. 10, pp. 3582-3589, 2015, https://doi.org/10.1109/TPS.2015.2440237.

[15]G. Mansutti, P. D. Carlo, M. Magarotto, M. A. Hannan, P. Rocca, and A. D. Capobianco, "Design of a hybrid metal-plasma transmit-array with beam-scanning capabilities," *IEEE Transactions on Plasma Science*, vol. 50, no. 3, pp. 662-669, 2022, https://doi.org/10.1109/TPS.2022.3149473.

[16]M. Magarotto, L. Schenato, P. De Carlo and A. -D. Capobianco, "Feasibility of a Plasma-based intelligent reflective surface," *IEEE Access*, vol. 10, pp. 97995-98003, 2022, https://doi.org/10.1109/ACCESS.2022.3206548.

[17]F. Sadeghikia, M. Valipour, M. T. Noghani, H. Ja'afar, and A. K. Horestani, "3D Beam steering end-fire helical antenna with beamwidth control using plasma reflectors," *IEEE Transactions on Antennas and Propagation*, vol. 69, no. 5, pp. 2507-2512, 2021, https://doi.org/10.1109/TAP.2020.3031473.

[18]F. Sadeghikia, M. Valipour, A. K. Horestani, M. Himdi, and T. Anderson, “Beam-steerable helical antenna using plasma reflectors,” in *16th* European *Conference on Antennas and Propagation (EuCAP)*, Madrid, Spain, 2022, https://doi.org/10.23919/EuCAP53622.2022.9769604.

[19]S. P. Chen and H. Schmiedel, *RF Antenna Beam Forming Focusing and Steering in Near and Far Field*, 2nd ed., Springer, 2024.

[20]Z. Xiao, Z. Han, A. Nallanathan, O. A. Dobre, B. Clerckx, and J. Choi, “Antenna array enabled space/air/ground communications and networking for 6G,” *IEEE Journal on Selected Areas in Communications*, vol. 40, no. 10, pp. 2773-2804, 2022, https://doi.oeg/10.1109/JSAC.2022.3196320.

[21]L. Yu, J. Wan, K. Zhang, F. Teng, L. Lei, and Y. Liu, “Spaceborne multibeam phased array antennas for satellite communications,” *IEEE Aerospace and Electronic Systems Magazine*, vol. 38, no. 3, pp. 28-47, 2023, https://doi.org/10.1109/MAES.2022.3231580.

[22]T. Tandel and S. Trapasiya, “Reconfigurable antenna for wireless communication: Recent developments, challenges and future,” *Wireless Personal Communication*, vol. 133, pp. 725–768, 2023, https://doi.org/10.1007/s11277-023-10785-7.

[23]K. Karthika and K. Kavitha, “Reconfigurable antennas for advanced wireless communications: A review,” *Wireless Personal Communication*, vol. 120, pp. 2711–2771, 2021, https://doi.org/10.1007/s11277-021-08555-4.

[24]J. K. Ji and M. G. Cho, “Compact beam steering antenna with low-loss Co2 Y-type hexagonal ferrite elements for wireless multiple-input multiple-output (MIMO) antenna applications,” *IEEE Magnetics Letters*, vol. 7, pp. 1-5, 2016, Art. no. 5504405, https://doi.org/10.1109/LMAG.2016.2585570.

[25]S. S. Iqbal Mitu, A. M. Al-Garni, H. A. Ragheb, and E. E. M. Hassan, “Three-dimensional beam scan using ferrite-loaded circular waveguide antenna,” *IEEE Antennas and Wireless Propagation Letters*, vol. 16, pp. 1131-1134, 2017, https://doi.org/10.1109/LAWP.2016.2624218.

[26]M. Magarotto, L. Schenato, P. De Carlo, and A. D. Capobianco, “Plasma-based reflective surface for polarization conversion,” *IEEE Transactions on Antennas and Propagation*, vol. 71, no. 3, pp. 2849-2854, 2023, https://doi.org/10.1109/TAP.2023.3239165.

[27]H. Yu, P. Li, J. Su, Z. Li, S. Xu, and F. Yang, “Reconfigurable bidirectional beam-steering aperture with transmitarray, reflectarray, and transmit-reflect-array modes switching,” *IEEE Transactions on Antennas and Propagation*, vol. 71, no. 1, pp. 581-595, 2023, https://doi.org/10.1109/TAP.2022.3222337.

[28]Y. Ji, L. Ge, J. Wang, Q. Chen, W. Wu, and Y. Li, “Reconfigurable phased-array antenna using continuously tunable substrate integrated waveguide phase shifter,” *IEEE Transactions on Antennas and Propagation*, vol. 67, no. 11, pp. 6894-6908, 2019, https://doi.org/10.1109/TAP.2019.2927813.

[29]B. Xi, Y. Xiao, S. Tan, F. Yang, and Z. Chen, “2-Bit wideband electronically controlled reconfigurable phased array with wide-angle beam-scanning capacity,” *IEEE Transactions on Antennas and Propagation*, vol. 71, no. 5, pp. 4128-4137, 2023, https://doi.org/10.1109/TAP.2023.3256276.

[30]M. I. Skolnik, *Introduction to Radar Systems*, 3rd ed., New York, NY, USA: McGraw-Hill, 2001.

[31]T. Liang, Z. Wang, and Y. Dong, “A beamwidth and steering reconfigurable active integrated metasurface antenna for dynamic radiation control,” *IEEE Transactions on Antennas and Propagation*, vol. 70, no. 10, pp. 9006-9016, 2022, https://doi.org/10.1109/TAP.2022.3177497.

[32]H. Li *et al.*, “Dual-band fresnel zone plate antenna with independently steerable beams,” *IEEE Transactions on Antennas and Propagation*, vol. 66, no. 4, pp. 2113–2118, 2018, https://doi.org/10.1109/TAP.2018.2804761.

[33]R. Morris, C. Jones, and M. Nagaraj, “Liquid crystal devices for beam steering applications,” *Micromachines*, vol. 12, no. 3, 2021, Art. no. 247, https://doi.org/10.3390/mi12030247.

[34]P. Aghabeyki, Y. Cai, G. Deng, Z. H. Tan, and S. Zhang, “A dual-polarized reconfigurable reflectarray with a thin liquid crystal layer and 2-D beam scanning,” *IEEE Transactions on Antennas and Propagation*, vol. 71, no. 4, pp. 3282-3293, 2023, https://doi.org/ 10.1109/TAP.2023.3240853.

[35]R. Reese *et al.*, “A millimeter-wave beam-steering lens antenna with reconfigurable aperture using liquid crystal,” *IEEE Transactions on Antennas and Propagation*, vol. 67, no. 8, pp. 5313-5324, 2019, https://doi.org/10.1109/TAP.2019.2918474.

[36]A. Manabe, “Liquid crystals for microwave applications,” in *7th European Conference on Antennas and Propagation (EuCAP)*, Gothenburg, Sweden, 2013, pp. 1793-1794, https://doi.org/10.1117/12.2016578.

[37]D. Melazzi, P. D. Carlo, F. Trezzolani, M. Manente, A. D. Capobianco, and S. Boscolo, “Beam-forming capabilities of a plasma circular reflector antenna,” *IET Microwaves, Antennas & Propagation*, vol. 12, no. 15, pp. 2301-2306, 2018, https://doi.org/10.1049/iet-map.2018.5178.

[38]M. T. Jusoh, O. Lafond, F. Colombel, and M. Himdi, “Performance of a reconfigurable reflector antenna with scanning capability using low-cost plasma elements,” *Microwave and Optical Technology*

Letters, vol. 55, no. 12, pp. 2869-2874, 2013, https://doi.org/10.1002/mop.27958.

[39]X. Ye *et al.*, “Radiation pattern in a tunable plasma window antenna,” *Journal of Physics D: Applied Physics*, vol. 55, no. 34, 2022, Art. no. 345201, https://doi.org/10.1088/1361-6463/ac7364.

[40]F. Sadeghikia, A. K. Horestani, and M. Himdi, “Reconfigurable antennas based on plasma reflectors and cylindrical slotted waveguide,” *Plasma Science - Recent Advances, New Perspectives and Applications [Working Title]*, IntechOpen, 2022, https://doi.org/10.5772/intechopen.108017.

[41]E. Koohkan, S. Jarchi, A. Ghorbani, and M. Bod, “Vortex beam generation based on plasma reflect- array surface at microwave frequencies,” *IEEE Transactions on Plasma Science*, vol. 49, no. 7, pp. 2086-2092, 2021, https://doi.org/10.1109/TPS.2021.3083199.

[42]F. Sadeghikia, F. Zamani, H. Ja'afar, and A. K. Horestani, “Steering radiated beam of a helical antenna using plasma reflectors,” in *International Workshop on Antenna Technology (iWAT)*, Sendai, Japan, 2024, pp. 63-66, https://doi.org/10.1109/iWAT57102.2024.10535799.

[43]F. Sadeghikia and F. Hodjat Kashani, “A two element plasma antenna array,” *Engineering, Technology, and Applied Science Research*, vol. 3, no. 5, pp. 516–521, 2013, https://doi.org/10.48084/etasr.319.

[44]M. Magarotto *et al.*, “Plasma antennas: A comprehensive review,” *IEEE Access*, vol. 12, pp. 80468-80490, 2024, https://doi.org/10.1109/ACCESS.2024.3411142.

[45]A. Ludvig-Osipov, J. M. Hannula, P. Naccachian, and B. L. G. Jonsson, “Physical limitations of phased array antennas,” *IEEE Transactions on Antennas and Propagation*, vol. 69, no. 9, pp. 5512-5523, 2021, https://doi.org/10.1109/TAP.2021.3069485.

[46]Z. Iqbal and M. Pour, “Grating lobe reduction in scanning phased array antennas with large element spacing,” *IEEE Transactions on Antennas and Propagation*, vol. 66, no. 12, pp. 6965-6974, 2018, https://doi.org/10.1109/TAP.2018.2874717.

[47]Z. Mousavi and P. Rezaei, “Millimetre-wave beam-steering array antenna by emphasising on improvement of Butler matrix features,” *IET Microwaves, Antennas & Propagation*, vol. 13, no. 9, pp. 1287–1292, 2019, https://doi.org/10.1049/iet-map.2018.5340.

[48]C. Caloz and T. Itoh, *Electromagnetic Metamaterials: Transmission Line Theory and Microwave Applications*, Hoboken, New Jersey, USA: Wiley & Sons, Inc., 2006.

[49]D. Wang, E. Polat, H. Tesmer, H. Maune, and R. Jakoby, “Switched and steered beam end-fire antenna array fed by wideband via-less butler matrix and tunable phase shifters based on liquid crystal technology,” *IEEE Transactions on Antennas and Propagation*, vol. 70, no. 7, pp. 5383-5392, 2022, https://doi.org/10.1109/TAP.2022.3142334.

[50]M. R. Dorbin, A. K. Horestani, F. Sadeghikia, M. T. Noghani, and H. Jaafar, “Analytical study on the resonance frequency of tunable surface-wave-excited plasma antennas,” *IEEE Transactions on Antennas and Propagation*, vol. 70, no. 10, pp. 3073-9082, 2022, https://doi.org/10.1109/TAP.2022.3184510.

[51]M. R. Dorbin, J. A. Rashed Mohassel, F. Sadeghikia, and H. B. Ja’afar, “Analytical estimation of the efficiency of surface-wave-excited plasma monopole antennas,” *IEEE Transactions on Antennas and Propagation*, vol. 70, no. 4, pp. 3040-3045, 2022, https://doi.org/10.1109/TAP.2021.3139967.

[52]M. Talafi Noghani, A. Karami Horestani, F. Sadeghikia, and M. R. Dorbin, “Theoretical modeling of resonant wavelength in 3-layered plasma antennas,” *Waves Random Complex Media*, vol. 31, no. 6, pp. 1587–1596, 2021, https://doi.org/10.1080/17455030.2019.1687959.

[53]F. Sadeghikia, M. R. Dorbin, A. K. Horestani, M. T. Noghani, and H. Ja'afar, “Tunable inverted-F antenna using plasma technologies,” *IEEE Antennas and Wireless Propagation Letters*, vol. 18, no. 4, pp. 702-706, 2019, https://doi.org/10.1109/LAWP.2019.2901354.

[54]F. Sadeghikia, K. Zafari, M. R. Dorbin, M. Himdi, and A. K. Horestani, “Reconfigurable biconcave lens antenna based on plasma technology,” *Scientific Reports*, vol. 13, 2023, Art. no. 9213, https://doi.org/10.1038/s41598-023-36332-9.

[55]F. Sadeghikia, M. R. Dorbin, A. K. Horestani, M. T. Noghani, and H. Ja’afar, “Multi-beam frequency tunable antenna based on plasma-nested helix,” in *13th European Conference on Antennas and Propagation (EuCAP)*, Krakow, Poland, 2019, pp. 1-3.

[56]J. Bazrafshan, F. Sadeghikia, A. K. Horestani, and M. Himdi, “A reconfigurable and steerable horn antenna using plasma dielectric slabs for controllable gain and beam steering,” *Journal of Space Science and Technology*, vol. 17, no. 3, pp. 18-24, 2024, https://doi.org/10.22034/jsst.2024.1455.

[57]J. Bazrafshan, F. Sadeghikia, A. K. Horestani, M. Himdi, and H. Jaafar, “Design and analysis of plasma-based reconfigurable maxwell fish-eye-lens antennas,” *Journal of Space Science and Technology*, vol. 17, Special Issue, pp. 22-31, 2024, https://doi.org/10.22034/jsst.2024.1491.

[58]F. Sadeghikia, H. Mahdikia, M. R. Dorbin, M. T. Noghani, A. K. Horestani, and H. Ja’afar, “A study on the effect of gas pressure and excitation frequency of a cylindrical plasma antenna on its radiation efficiency,” in *13th European Conference on Antennas and Propagation (EuCAP)*, Krakow, Poland, 2019, pp. 1-4.

JSST
Journal of Space Science and Technology

P-ISSN: 2008-4560
E-ISSN: 2423-4516

Journal of Space Science and Technology

Vol. 18, Special Issue, pp. 26-33, 2025
https://doi.org/10.22034/jsst.2025.1520
Journal Homepage: https://www.jsstpub.com

Original Research Paper

Effectiveness of Multi-Layered Radiation Shields Constructed from Polyethylene and Metal Hydrides Using HZETRN and OLTARIS for Space Applications

VV Sreedevi and Kavita Lalwani*

Department of Physics, Malaviya National Institute of Technology Jaipur, India

ARTICLE INFO

Article History:

Received 15 January 2025
Revised 22 February 2025
Accepted 02 March 2025
Available Online 08 April 2025

Keywords:

Space radiation
Metal hydrides
Polyethylene
HZETRN
OLTARIS

ABSTRACT

A major challenge for extended human spaceflight in deep space is the hazardous exposure to space radiation, which consists of high-energy particles that pose significant risks to astronaut health. Effective radiation shielding is essential to mitigate these risks. This study optimizes the shielding performance of a multi-layered structure composed of polyethylene and metal hydrides for space applications. Using two simulation tools: HZETRN and OLTARIS, developed by NASA, we model these structures and evaluate dose equivalent in a Galactic Cosmic Ray (GCR) free-space radiation environment, which is the primary and major contributor to radiation exposure for long-duration space missions. Among the materials studied, lithium hydride exhibits the highest shielding effectiveness. The results on the dose equivalent are compared with aluminum, a conventional shielding material, revealing that the multi-layered structure constructed from polyethylene and lithium hydride provides a 54.9% improvement in shielding effectiveness while maintaining structural stability. Additionally, the dose equivalent contribution of different radiation particles (protons, alpha particles, and heavy ions) and their flux are analyzed for further validation across both tools. Our results highlight the effectiveness of multi-layered shielding in reducing dose equivalent while maintaining structural stability, making it a viable solution for deep-space missions.

* Corresponding Author's E-mail: kavita.phy@mnit.ac.in

How to Cite this Article:
VV. Sreedevi and Kavita Lalwani, "Effectiveness of multi-layered radiation shields constructed from polyethylene and metal hydrides using HZETRN and OLTARIS for space applications," *Journal of Space Science and Technology*, Vol. 18, Special Issue, pp. 26-33, 2025, https://doi.org/10.22034/jsst.2025.1520.

1. INTRODUCTION

One of the main challenges for prolonged human space expeditions is space radiation. Unlike on Earth, interplanetary space is constantly being bombarded with ionising radiation [1]. Exposure to such high radiation for a long duration can-do severe harm to the human body as well as electronic equipment. Space radiation cannot reach the Earth's surface because of the strong magnetic field and thick atmosphere of Earth. There are three main sources of space radiation: Galactic Cosmic Rays (GCRs), Solar Particle Events (SPEs), and Trapped particles such as electrons and protons. GCR is the primary and major contributor to radiation exposure for long-duration space missions. It consists of high-energy particles comprising 85% proton, 13% alpha particles, and heavy ions, with atomic numbers ranging from Z=1 to Z=28, that can penetrate spacecraft shielding and induce secondary radiation, making them crucial for shielding optimization. SEPs are sporadic and event-driven, whereas trapped radiation (Van Allen belts) is mainly relevant for LEO, not deep-space conditions considered in this study. Hence only GCR flux is considered for dose calculations in this study. Effective shielding against GCRs requires materials that not only stop primary particles but also minimize the production of secondary particles.

To minimize the radiation effects from different particles in the GCR space radiation environment, there are mainly two techniques for space radiation shielding: active and passive shielding methods [2]. Active shielding uses electromagnetic fields to divert harmful radiation. This advanced technique lowers direct exposure but necessitates energy input and intricate systems to sustain its effectiveness [3]. Active shielding remains largely theoretical and requires substantial advancements before it can be widely deployed. In this work, we focus on passive shielding techniques, where a physical material is employed, which can effectively attenuate the incoming radiation. Heavy charged particles lose their energy in shielding materials through electronic and nuclear fragmentation. Conventionally, aluminum is used as a passive shielding material due to its high density and tensile strength. However, studies have shown that liquid hydrogen offers significantly better dose reduction. Despite its effectiveness, liquid hydrogen is highly unstable, making it impractical for space radiation shielding. While previous studies have broadly explored the shielding effectiveness of various materials, we investigate the shielding effectiveness of hydrogen-rich materials, specifically metal hydrides. To further enhance structural strength, we propose multi-layered shields combining metal hydrides with polyethylene. This novel shielding design not only improves dose equivalent reduction but also enhances mechanical stability. Thus, the objective of this study is to evaluate the effectiveness of metal hydride-based shielding compared to conventional materials using HZETRN [4] and OLTARIS [5,6] simulations.

2. MATERIALS AND SIMULATION SETUP

In this section, the different shielding materials and their properties are discussed in detail. Further, the simulation tools HZETRN and OLTARIS are introduced.

2.1 Radiation Shielding Materials:

The selection of shielding materials for spacecraft must consider both high shielding effectiveness and additional essential properties such as high tensile strength and low reactivity. While high-density materials offer structural strength, they can also contribute to increased radiation exposure due to secondary radiation production. In contrast, low-density, hydrogen-rich materials are highly effective in reducing the dose equivalent but often require additional structural reinforcement. A promising approach to optimizing shielding performance is multi-layered shielding, which strategically combines materials of different densities to balance radiation protection and mechanical stability. Traditionally, aluminum has been widely used in spacecraft due to its lightweight nature and structural integrity. However, studies have shown that several other materials result in lower absorbed doses compared to aluminum. Among shielding materials, hydrogen is the most effective in reducing radiation exposure. However, its high instability presents significant challenges for practical application in spacecraft. As an alternative, hydrogen-containing compounds exhibit excellent shielding properties while offering better stability. Polyethylene, which has one of the highest hydrogen contents among polymers, is more effective than many other conventional materials, including aluminum. Additionally, as a polymer, its structural properties can be modified to enhance both mechanical strength and radiation shielding performance. UHMWPE (Ultra High Molecular Weight Polyethylene) [7] is a specialised form of polyethylene, characterised as a linear, semi-crystalline homopolymer with an exceptionally high molecular mass. UHMWPE fibres offer excellent radiation shielding, high tensile strength, low density, superior impact resistance, and durability in space environments, making them a promising material for future space structure applications. Metal hydrides are known for their hydrogen-storing capacity [8-10]. Following astrophysical conventions, all elements heavier than hydrogen are often referred to as metals. Therefore, in this study metal hydrides refer to compounds where hydrogen is chemically bonded to elements heavier than hydrogen. This paper explores the shielding effectiveness of various metal hydrides, as well as multi-layered shields combining polyethylene and metal hydrides. The materials such as Lithium Hydride, Lithium Borohydride, Beryllium Hydride, Beryllium Borohydride, Ammonia Borane, and Super Hydride are selected for their high hydrogen content and the presence of other low-Z elements, both of which are effective in attenuating high-energy heavy ions. Table 1 gives the list of all materials used in this study along with their chemical formula and density.

Table 1. List of optimised shielding materials.

S.No.	Material Name	Chemical Formula	Density in g/cm^3
1	Aluminum	Al	2.7
2	Polyethylene	C_2H_4	0.96
3	Beryllium Borohydride	$Be\,(BH_4)_2$	0.604
4	Ammonia Borane	NH_3BH_3	0.78
5	Super Hydride	$Li(C_2H_5)_3BH$	0.89
6	Beryllium Hydride	BeH_2	0.65
7	Lithium Borohydride	$LiBH_4$	0.68
8	Lithium Hydride	LiH	0.82

2.2 HZETRN

The HZETRN (High charge (Z) and Energy TRaNsport) code is a deterministic transport model designed by NASA specifically for simulating space radiation transport. The HZETRN code employs numerical solutions to the time-independent, linear Boltzmann equation, utilizing the continuous slowing-down approximation. In this approach, discrete atomic interactions are modeled through stopping power. HZETRN2015 is employed for all calculations in this study. The code supports transport calculations for Galactic Cosmic Rays (GCR), Solar Particle Events (SPE), Low Earth Orbit (LEO), and custom environmental boundary conditions. For SPE and LEO scenarios, it accounts for the transport of neutrons, protons, and light ions, while GCR boundary conditions extend to include heavy ions, pions, muons, electrons, positrons, and photons.

2.3 OLTARIS

In this work, OLTARIS simulation software is used to investigate the proposed materials for space radiation shielding. OLTARIS is a NASA-based software platform. A flowchart for data flow and execution is shown in Figure 1. Materials for space radiation shielding are characterized based on their density and chemical composition. The chemical composition of the materials is defined in terms of chemical formula, elemental mass percentage or molecular mass percentage. The geometry of the shields is specified as either a semi-infinite slab or a spherical configuration with any number of materials/layers in any order. In this study, spherical geometry is being used with radius varying from 1-15 g/cm^2. Also, for simulating multi-layered shields, semi-infinite slab geometry consisting of three layers is used.

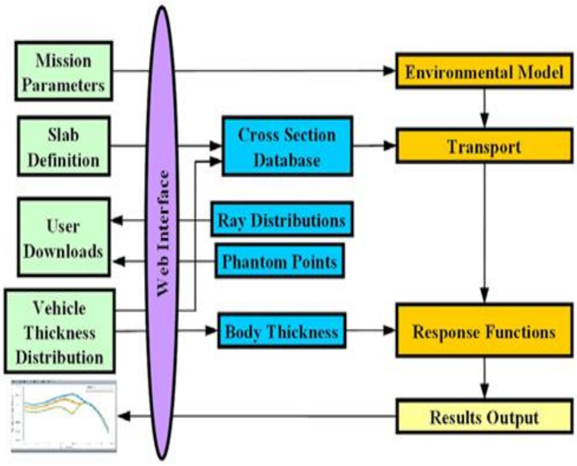

Fig. 1. OLTARIS data and execution flowchart [5].

OLTARIS has many benefits as it provides information on dose equivalent and flux contributions from different particle radiations such as protons, alpha particles, neutrons, and heavy ions. In addition, it also gives organ-wise dose equivalent, effective dose equivalent (for female or male anatomical model), and Linear Energy Transfer (LET) as response functions.

All simulations are carried out in a free-space Galactic Cosmic Ray (GCR) environment at 1 AU, using the Badhwar-O'Neill 2014 model [11]. The full GCR spectrum is included, incorporating all ions (proton and heavy ions) atomic numbers ranging from Z = 1 to Z = 28 in the boundary conditions. Since GCR flux is higher during solar minimum, a solar modulation parameter (φ) of 475 MV is selected to represent these conditions for a 1-day mission duration. The response is evaluated in tissue using the ICRP 60 quality factor [12]. These parameters remain consistent across both HZETRN and OLTARIS simulations.

3. RESULTS

In this section, the dose equivalent contribution of different radiation particles (protons, alpha particles, and heavy ions) and their flux are analyzed using both tools. As the absorbed dose quantifies the energy deposited per unit mass of a material, therefore in order to account for the varying biological impact of different types of radiation, the dose equivalent is calculated by multiplying the absorbed dose by a quality factor (Q), which adjusts for radiation-specific biological effectiveness.

3.1 Dose Equivalent for Variable Thickness of Shielding Materials

The dose equivalent of different materials is computed in the tissue by varying their thickness from 5 to 15 g/cm^2 in HZETRN. Spherical geometry is used to run the simulation. The results are shown in Fig. 2.

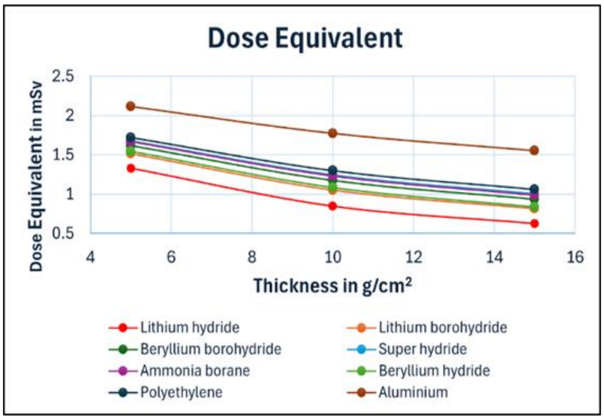

Fig. 2. Variation of dose equivalent with a thickness of metal hydrides, polyethylene, and aluminium using HZETRN.

It can be seen from the figure that, beyond 15 g/cm^2, there is no considerable reduction in dose. The dose equivalent of metal hydrides is less than polyethylene and aluminium. Lithium hydride offers a much lesser dose equivalent than other metal hydrides. Hence, it has greater potential for space radiation shielding as compared to other metal hydrides.

3.2 Dose Equivalent from Different Particles

The particle-wise dose equivalent is studied for different incoming particles such as proton, alpha particle, and heavy ion (iron) in the GCR spectrum. The thickness for all the materials is 15 g/cm^2. Proton and alpha particles are the particles with high relative abundance in the GCR spectrum and iron represents the HZE (High Charge and Energy) particle category. The results are shown in Fig. 3.

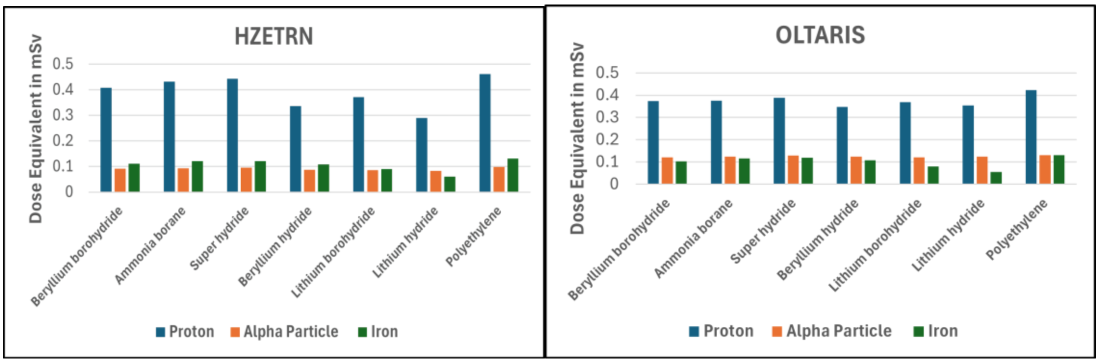

Fig. 3. Particle-wise dose equivalent of 15 g/cm^2 of metal hydrides and polyethylene using HZETRN (left) and OLTARIS (right).

The highest dose equivalent is due to the proton, which is clearly due to its abundance. The dose equivalent due to iron, despite its low abundance, is comparable to that of alpha particles. The comparison between the metal hydrides aligns with the previous trend (Section 3.1). Lithium hydride is effective in reducing proton as well as heavy ion doses. The results from both HZETRN and OLTARIS confirm the relative effectiveness between the different materials. The dose equivalent of proton in HZETRN is in general slightly higher than that in OLTARIS and the dose equivalent of alpha particle is higher in OLTARIS when compared to that in HZETRN. The difference in these results can be due to the difference in numerical approximations employed in HZETRN and OLTARIS that can introduce systematic biases in their radiation transport calculations. Because HZETRN uses semi-empirical nuclear fragmentation models, and OLTARIS incorporates updated NASA cross-section libraries.

3.3 Comparison of Dose Equivalent in HZETRN and OLTARIS

In this section, we compare the dose equivalent for variable thickness of LiH and polyethylene from HZETRN and OLTARIS. The results are shown in Fig. 4.

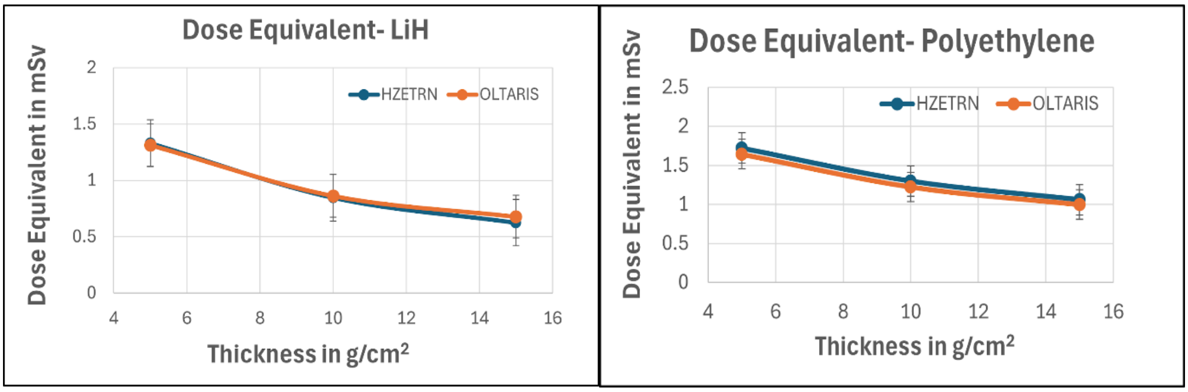

Fig. 4. Dose equivalent of lithium hydride (left) and polyethylene (right) - comparison between OLTARIS and HZETRN.

From section 3.1 it can be seen that out of all metal hydrides, LiH proves to be a better shielding material, as it produces the least dose equivalent. Polyethylene is also taken into consideration due to its high tensile strength. For LiH, dose equivalent values from both transport codes are in agreement. For polyethylene, the dose equivalent values from HZETRN are higher than that from OLTARIS by 0.0715 mSv on average.

3.4 Comparison of Radiation Flux in HZETRN and OLTARIS

Radiation flux after transport as a function of kinetic energy is studied for proton, alpha particle, and iron in LiH. The results are shown in Fig. 5.

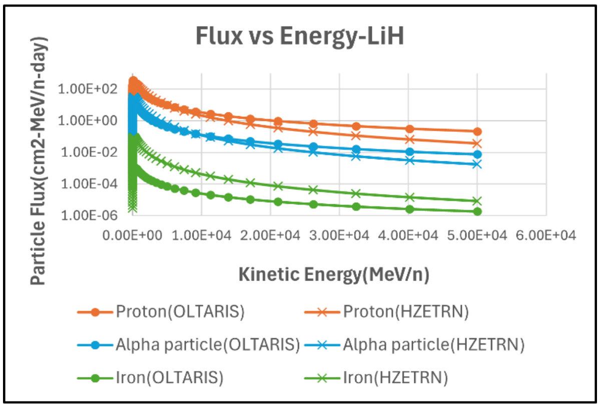

Fig. 5. Flux vs energy of 15 g/cm^2 lithium hydride using HZETRN and OLTARIS.

The relative values of particle flux for proton, alpha particle, and iron correspond to their abundance in the GCR spectrum. At higher energies, the particle flux for each particle reduces. Flux after transport obtained from OLTARIS is higher for proton and alpha particles and is lesser for iron when compared to the values from HZETRN.

3.5 Comparison of Dose Equivalent for Multi-layered Shields

A multi-layered semi-infinite slab of 15 g/cm^2, which consists of three layers of 5 g/cm^2 each is created using polyethylene and lithium hydride. The dose equivalent is calculated for all possible combinations of such a shield and is compared with that of 15 g/cm^2 LiH slab and 15 g/cm^2 polyethylene slab. The results of dose equivalent from OLTARIS and HZETRN are compared and shown in Fig. 6.

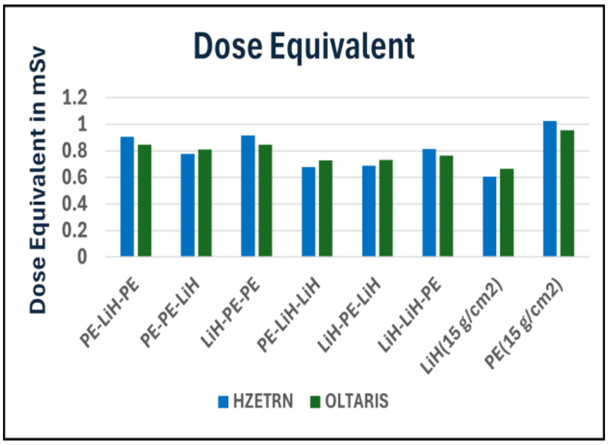

Fig. 6. Dose equivalent of different combinations of a multi-layered shield using polyethylene and lithium hydride.

The results show that the dose equivalent not only depends on the material composition of the shield but also the relative position of the materials. LiH seems to be more effective when placed in the innermost layer than when it is placed in the middle or outer layer. The dose equivalent values from HZETRN and OLTARIS are in agreement. The average difference between both sets of results is 0.0537mSv. It is noteworthy that there is only a little difference in dose equivalent between the 15 g/cm^2 LiH slab and PE-LiH-LiH combination. On comparing the results from multi-layered shields of this work with the previous work [13] where aluminium was used, we observed that a multi-layered shield with polyethylene gives a lesser dose equivalent and it is more feasible as it is lightweight shielding material for practical application in space.

3.6 Variation of Dose Equivalent with Depth Inside the Multi-layered Shields

From section 3.5, it is observed that the dose equivalent depends on the order of different shielding layers inside the radiation shield. Therefore, it is necessary to investigate the variation in dose equivalent with depth inside the shield. Let us take the cases of two shields with the same material composition: PE-LiH-LiH and LiH-LiH-PE (two LiH layers and one PE layer). The multi-layered shields consist of three layers of 5 g/cm^2 each, the total thickness of the shield being 15 g/cm^2. The variation of dose equivalent with depth of these two shields is computed and is shown in Fig. 7.

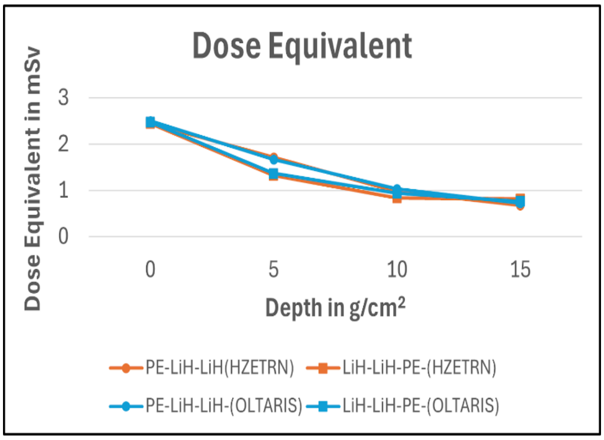

Fig. 7. Dose equivalent vs depth for PE-LiH-LiH and LiH-LiH-PE combinations using OLTARIS and HZETRN.

It can be seen that maximum dose reduction is achieved in the outermost layer. Polyethylene on the inner layer does not contribute to the dose reduction as when it is placed on the outer layer. The results from both sources align with this observation.

4. CONCLUSION

In this study, we investigated the shielding effectiveness of various metal hydrides based on their hydrogen storage capacity. The dose equivalent variation with shield thickness was analyzed, along with particle-wise dose contributions. All tested hydrides outperformed conventional materials like aluminum and polyethylene, with lithium hydride (LiH) emerging as the most effective. Further, a multi-layered shield combining LiH with polyethylene was evaluated, showing that an outer polyethylene layer improves the structural stability of the radiation shield without affecting the dose equivalent significantly. Particle flux after transport through 15 g/cm² of LiH was also examined. The variation of dose equivalent with depth inside the optimal combination of multi-layered structures was also studied. This novel study is important as it gives information on how the radiation from different particles interacts while passing through the shielding material and it was not done in the previous work [13]. The results from HZETRN and OLTARIS showed strong agreement, with a maximum discrepancy of 0.07 mSv. These findings highlight the potential of LiH-based shielding in space applications, offering an effective balance between radiation protection and structural stability.

5. FUTURE PERSPECTIVES

This study has demonstrated the radiation shielding effectiveness of multi-layered shields constructed from polyethylene and lithium hydride. The outcome of the simulation studies will be useful as an input for fabricating radiation shields for space applications. However, significant opportunities remain to enhance the shielding performance of polymer-based materials. One promising direction is the integration of various nanofillers into polymer matrices [14], which could improve material properties and enhance radiation attenuation. Additionally, further investigation into a broader range of hydride materials may lead to the discovery of novel compounds with superior dose-reduction capabilities.

Another emerging area of research is the development of hybrid methods [15] that integrate passive and active shielding techniques. These approaches aim to combine the material-based shielding of passive systems with the dynamic capabilities of active shielding technologies, such as magnetic or electric fields, to achieve more effective and versatile radiation protection. Together, these advancements could revolutionize shielding strategies, offering lightweight, efficient, and adaptable solutions for a variety of applications.

CONFLICTS OF INTERESTS

The authors declare that they have no conflict of interest.

ACKNOWLEDGEMENTS

We thank MNIT Jaipur for supporting this research work. We are also thankful for the OLTARIS and HZETRN transport codes provided by NASA.

REFERENCES

[1] G. A. Nelson, “Space radiation and human exposures, A primer,” *Radiation Research*, vol. 185, no. 4, pp. 349–358, 2016, https://doi.org/10.1667/RR14311.1.

[2] P. Spillantini *et al.*, “Shielding from cosmic radiation for interplanetary missions: Active and passive methods,” *Radiation Measurements*, vol. 42, no. 1, pp. 14-23, 2007, https://doi.org/10.1016/j.radmeas.2006.04.028.

[3] L. W. Townsend, “Overview of active methods for shielding spacecraft from energetic space radiation,” *Physica Medica*, vol. 17, pp. 84-85, 2001.

[4] J. W. Wilson *et al.*, “HZETRN: description of a free-space ion and nucleon transport and shielding computer program,” NASA, Tech. Paper 349, 1995.

[5] NASA. “OLTARIS” (18/02/2025). [Online]. Available: https://oltaris.larc.nasa.gov/

[6] T. C. Slaba, A. M. McMullen, S. A. Thibeault, C. A. Sandridge, M. S. Clowdsley, and S. R. Blattnig, “OLTARIS: An efficient web-based tool for analyzing materials exposed to space radiation,” *Nanophotonics and Macrophotonics for Space Environments V*, vol. 8164, 2011, Art. No. 81640G, https://doi.org/10.1117/12.898960.

[7] J. H. Cha, S. K. Sarath Kumar, C. G. Kim, J. E. Noh, J. S. Choi, and Y. Kim, “Ultra-high-molecular-weight-polyethylene/hydrogen-rich benzoxazine composite with improved interlaminar shear strength for cosmic radiation shielding and space environment applications,” *Composite Structures*, vol. 300, 2022, Art. no. 116157, https://doi.org/10.1016/j.compstruct.2022.116157.

[8] B. Sakintuna, F. Lamari-Darkrim, and M. Hirscher, “Metal hydride materials for solid hydrogen storage: A review,” *International Journal of Hydrogen Energy*, vol. 32, no. 9, 2007, pp. 1121-1140, 3199, https://doi.org/10.1016/j.ijhydene.2006.11.022.

[9] W. Atwell, K. Rojdev, D. Liang, and M. Hill, “Metal hydrides, MOFs, and Carbon composites as space radiation shielding mitigators,” in *44th International Conference on Environmental Systems*, Tucson, Arizona, USA, 2014.

[10] A. M. Osman, “Analysis of radiation shielding effectiveness of hydride and borohydride metals for nuclear industry,” *International Journal of Advanced Nuclear Reactor Design and*

Technology, vol. 5, no. 1, pp. 30-43, 2023, https://doi.org/10.1016/j.jandt.2023.04.001.

[11] P. M. O'Neill, S. Golge, and T. C. Slaba, “Badhwar-O'Neill 2014 galactic cosmic ray flux model description,” NASA, TP-2015-218569, 2015.

[12] A. V. Sannikov and E. N. Savitskaya, “Ambient dose equivalent conversion factors for high energy neutrons based on the icrp 60 recommendations,” *Radiation Protection Dosimetry*, vol. 70, no. 1-4, pp. 383–386, 1997, https://doi.org/10.1093/oxfordjournals.rpd.a031982.

[13] A. Gohel and R. Makwana, “Multi-layered shielding materials for high energy space radiation,” *Radiation Physics and Chemistry*, vol. 197, 2022, Art. no. 110131, https://doi.org/10.1016/j.radphyschem.2022.110131.

[14] E. Toto, L. Lambertini, S. Laurenzi, and M. Gabriella Santonicola, “Recent advances and challenges in polymer-based materials for space radiation shielding,” *Polymers*, vol. 16, no. 3, 2024, Art. no. 382, https://doi.org/10.3390/polym16030382.

[15] R. P. Chowdhury, L. A. Stegeman, M. L. Lund, D. Fry, S. Madzunkov, and A. A. Bahadori, “Hybrid methods of radiation shielding against deep-space radiation,” *Life Sciences in Space Research*, vol. 38, pp. 67-78, 2023, https://doi.org/10.1016/j.lssr.2023.04.004.

JSST Journal of Space Science and Technology

P-ISSN: 2008-4560
E-ISSN: 2423-4516

Journal of Space Science and Technology

Vol. 18, Special Issue, pp. 34-40, 2025
https://doi.org/10.22034/jsst.2025.1526
Journal Homepage: https://www.jsstpub.com

Original Research Paper

Simultaneous Resolution and Dynamic Range Improvement in Microwave Phase-Variation Displacement Sensors

Amirhossein Karami Horestani*, Ferran Paredes, and Ferran Martín

Departament d’Enginyeria Electrònica, Universitat Autónoma de Barcelona, Bellaterra, Spain

ARTICLE INFO

Article History:

Received 26 January 2025
Revised 08 April 2025
Accepted 15 April 2025
Available Online 19 April 2025

Keywords:

Index terms-microstrip technology
Microwave sensor
Reflective-mode sensor
Displacement sensor
Phase-variation sensor

ABSTRACT

In this paper, a reflective-mode phase-variation microwave displacement sensor is proposed. It consists of a reader, a one-port microstrip line terminated with a matched load, and a movable resonator (etched in an independent substrate), which exhibits three different resonance frequencies, two of them in low frequency range and close to each other, and the third one at a higher frequency. The sensing mechanism is based on the motion of the resonator along the microstrip line, with a small airgap in between. The phase of the reflection coefficient at the three resonance frequencies of the resonator is recorded at the input port of the reader. As a result, the motion of the movable resonator can be characterized. The phase of the reflection coefficient at the two lower frequencies is used to enhance the dynamic range, while the phase at the higher frequency improves sensor resolution.

* Corresponding Author’s E-mail: Amirhossein.Karami@uab.cat

How to Cite this Article:
A. Karami Horestani, F. Paredes, and F. Martín, "Simultaneous resolution and dynamic range improvement in microwave phase-variation displacement sensors," *Journal of Space Science and Technology*, Vol. 18, Special Issue, pp. 34-40, 2025, https://doi.org/10.22034/jsst.2025.1526.

1. INTRODUCTION

In many industrial, medical, and laboratory systems, the use of linear or angular displacement/velocity sensors is vital and, according to the needs and conditions of any of these applications, the proper type of sensor differs. Thus, different types of displacement/velocity sensors, like optical, microwave, and magnetic have been proposed by researchers [1-11]. In [1], rotary encoders which are one of the most widely used displacement sensors have been discussed while magnetic and Hall-effect sensors are presented in [4-8]. On the other hand, some microwave displacement sensors are introduced in [9-11] which are a clue to show the interest of the researchers in this technology for sensor realization. The advantages of microwave sensors over other sensor types are their low cost and their robustness in harsh environments, besides being implementable in printed circuit board (PCB) technology.

One method for sensing the displacement/velocity in microwave sensors is based on measuring the changes in the amplitude or phase of the reflection or transmission coefficient in a reader (typically a transmission line) by moving a planar resonant element on top of it [12-23]. Some of these cited works are related to the displacement sensors for smaller dynamic ranges like [12-14] and some others like [15,16] are electromagnetic encoders which allow detecting displacements in higher dynamic ranges but lower resolution. In one of the authors' recent work, a linear displacement sensor suitable for breath rate monitoring, based on the measurement of the phase of the reflection coefficient of the reader line, has been presented [24]. In that sensor, resolution cannot be improved without sacrificing the dynamic range and by increasing the resonance frequency of the resonator, i.e., the frequency of operation. By increasing the frequency (decreasing the wavelength) of the feeding signal, the resolution improves, but the dynamic range decreases. So, a trade-off between resolution and dynamic range exists in that sensor. After the mentioned work, two other works have been carried out in order to address this issue. In [25] by working simultaneously with two different frequencies and utilizing two resonators rather than one, it is demonstrated that the sensor exhibits better resolution, without decreasing the dynamic range. On the other hand, in [26], a sensor based also on measuring the phase of the reflection coefficient was proposed, but the reader in that sensor consists of two microstrip lines (rather than one), and the movable part includes two resonators tuned at closely spaced frequencies. By using this method, the input dynamic range (which is normally limited to the half-wavelength at the working frequency) can be dramatically enhanced without degrading the resolution. In this paper, we combine the two previously mentioned ideas in order to improve the dynamic range and resolution of the sensor simultaneously. As an explanation, we used three working frequencies, two of them in lower frequencies and close to each other, to enhance the dynamic range of the sensor based on what proposed in [26] and the third working frequency, much higher than the two first, to be able to improve the resolution of the sensor based on what presented in [25]. The compactness of the sensor was also improved, by using a single microstrip line in the reader (instead of two lines in [26]) and a single resonator in the movable part which can resonate in all the three considered working frequencies.

This proposed microwave displacement sensor has potential applications in space technology, particularly in precision positioning systems. The ability to characterize motion with enhanced dynamic range and high resolution makes it suitable for tracking the displacement of critical components in satellites, space probes, and robotic arms used in space applications.

The paper is organized as follows. The proposed displacement sensor and its working principle are presented in Section II. In Section III, the sensor is validated both at simulation level and experimentally. In Section IV, the resolution and dynamic range of the proposed sensor is compared with that of other displacement sensors. Finally, the main conclusions are highlighted in Section V.

2. SENSOR CONCEPT AND WORKING PRINCIPLE

As mentioned in the introduction, a displacement sensor based on retrieving the phase of the reflection coefficient of the reader line was published in [24]. That sensor consists of a (static) reader and a movable (resonator) part. The reader in that sensor is a simple 50-Ω microstrip line terminated with a matched load. A resonator etched/printed on a separate dielectric substrate is able to move on top of the reader with a small air gap between them along the microstrip axis. A single frequency harmonic signal is injected to the input port of the reader with a frequency identical to the resonance frequency of the resonator on the movable part. Thus, the injected signal is reflected at the transverse plane where the resonator is placed (on top of the microstrip line), and the phase of this reflected signal depends on the distance between the resonator and the input port of the reader. Therefore, by reading this phase, the position of the resonator can be retrieved. Note that in this kind of sensors, based on the phase of the reflection coefficient, the dynamic range of the sensor is limited to a half wavelength at the working frequency, since, after this range, the phase cyclically repeats. On the other hand, the resolution of this type of sensor is related to the least amount of detectable phase for the system and the amount of phase change versus displacement. Obviously by working at higher frequencies the resolution will improve because the same amount of displacement makes higher phase change in higher frequencies. However, this strategy causes a reduction in the sensor dynamic range due to decrease in the wavelength.

In [25], the resolution was improved without decreasing the dynamic range in these sensors. To achieve this goal, two resonators were etched on the movable substrate. One of these resonators was tuned to a low frequency, so that by reading the phase of the reflection coefficient at that frequency, an acceptable dynamic range (given by the half wavelength of the signal at that frequency) was achieved. The second resonator, tuned to a higher frequency, was used to enhance the resolution of the sensor by measuring the phase of the reflection coefficient at its resonance frequency. It is worth mentioning that, with this method, two harmonic signals with frequencies equal to the resonance frequencies of the resonators must be injected to the input port of the reader.

In [26], the dynamic range was increased without considering lower frequencies (since this would result in a degradation of the sensor resolution). The proposed structure in [26] consists of a reader with two independent 50-Ω microstrip lines terminated with matched loads. The substrate of the movable part contains two resonators etched on it, each one moving on top and along the axis of the reader microstrip lines. The dimensions of the resonators were chosen in a way that their resonance frequencies were close spaced. Therefore, in each phase cycle caused by the displacement of the resonators on top of reader, there is a small difference between the phase of the reflection coefficient read in the two reader ports (the phase cycle for the higher frequency is slightly lower than the other). As a result, even though the phase of the reflection coefficient repeats cyclically for both line by displacing the resonators on top of the reader, the phase difference between them differs for each cycle, until a total displacement equivalent to the minimum common multiple (MCM) of the half wavelength at both frequencies is achieved. By using this method, comprehensively discussed in [26], the dynamic range of the sensor was increased considerably without degrading the resolution.

In this work, we combine the two previously mentioned methods in order to improve simultaneously the resolution and the dynamic range of the sensor, avoiding the use of two microstrip lines in the reader. By this means, the resulting sensor is more compact. The reader consists of a unique 50-Ω microstrip line terminated with a matched load. The movable part consists of a microwave substrate with a single resonator (made of two back-to-back connected C-shaped loops) etched on it. This movable part displaces along the microstrip line axis on top of it with a small airgap between them. The resonator exhibits three resonance frequencies which are of our interest. Two of them (f_A, f_B) are closely spaced and relatively small (suitable for the method presented in [26] to increase the dynamic range). The third frequency (f_C), at higher frequencies, is suitable for enhancing the resolution [25]). So, by injecting a multiple-frequency signal containing all these three frequencies, the phase of the reflection coefficient can be used to detect the displacement and position with precise resolution and long dynamic range. A perspective view of the sensor's structure is shown in Fig. 1.

Fig. 1. Perspective view of the proposed reflective-mode phase-variation displacement sensor.

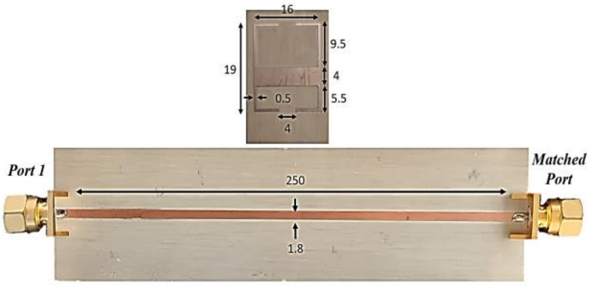

Fig. 2. Photograph of the fabricated reader and resonators with their dimensions in mm.

3. FABRICATION, MEASUREMENT, AND RESULTS

To validate the method, the proposed sensor, consisting of the reader (static part) and the resonator (movable part) has been designed, simulated, and fabricated on the *I-Tera MT40* substrate with dielectric constant $\varepsilon_r = 3.38$, thickness $h = 0.76$ mm, and loss tangent tanδ = 0.0028. The airgap between the reader and resonator has been considered to be $g = 0.2$ mm. To implement a 50-Ω microstrip line in this substrate, the width of the line is set to $W = 1.8$ mm. The frequencies of interest in this work, in which the resonator causes a strong reflection are considered to be $f_A = 3.0$ GHz, $f_B = 3.7$ GHz, and $f_C = 9.1$ GHz. The corresponding wavelengths are approximately $\lambda_A = 6.0$ cm, $\lambda_B = 4.8$ cm, and $\lambda_C = 2.0$ cm. As a result, according to [26], the sensor dynamic range is approximately $4\lambda_A/2 = 5\lambda_B/2 = 12$ cm. On the other hand, the resolution of the sensor is determined by the phase changes at f_C. To clarify this, we can consider that the smallest phase difference that can be detected by our measurement setup is 5°. So, the obtainable resolution for f_A, f_B, and f_C are 0.42 mm, 0.33 mm, and 0.14 mm respectively. Thus, the resolution of the whole system is given by the smallest value (at f_C), namely, 0.14 mm. The structure and dimensions of the reader and resonator can be seen in Fig. 2.

A set of electromagnetic simulations was carried out using the *ANSYS HFSS* commercial software. The magnitude of the reflection coefficient when the resonator is placed on top of the reader line is depicted in Fig. 3. It can be appreciated that the signal at the considered frequencies, f_A, f_B, and f_C, is significantly reflected back to the input port (i.e., the return loss is close to 0dB at these frequencies).

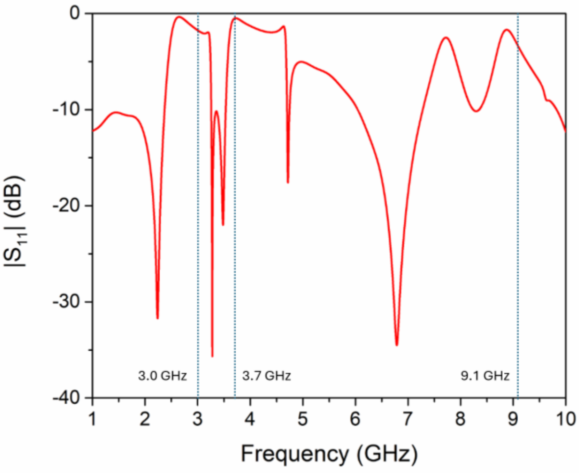

Fig. 3. Magnitude of the reflection coefficient versus frequency inferred from electromagnetic simulation.

In Fig. 4, the phase of the reflection coefficient at the considered frequencies inferred from electromagnetic simulation is depicted, whereas the measured phases are shown in Fig. 5. The measurement has been carried out on the fabricated prototype by using the vector network analyzer (VNA) *Keysight FieldFox N9950B*. Note that the discrepancies between simulation and measurement results are related to fabrication tolerances and to the fact that it is difficult in practice to keep exactly the same condition as in simulation. By inspection of Figs. 4 and 5, it follows that by using the phase of the reflection coefficient at two lower frequencies, the displacement and position can be appreciated at least in a range of $4\lambda_A/2 = 5\lambda_B/2 = 12$ cm, as mentioned before. On the other hand, after determining the position of the sensor with low resolution using the phase of the reflection coefficient at f_A and f_B, the phase at f_C provides the position with high resolution and accuracy. It is worth noting that the vertical distance between the resonator and the reader must be in a range that in which there is enough coupling between the resonator and the reader's line to have enough reflected signal in working frequencies. So, the airgap can be chosen any value in the mentioned range but once we select the amount of airgap, it should be kept constant during the measurement because changing the airgap can lead to alteration of the resonance frequencies. Another point to consider is that the resonator must move along the microstrip line's axis and misalignment from the line's axis can lead to wrong outputs.

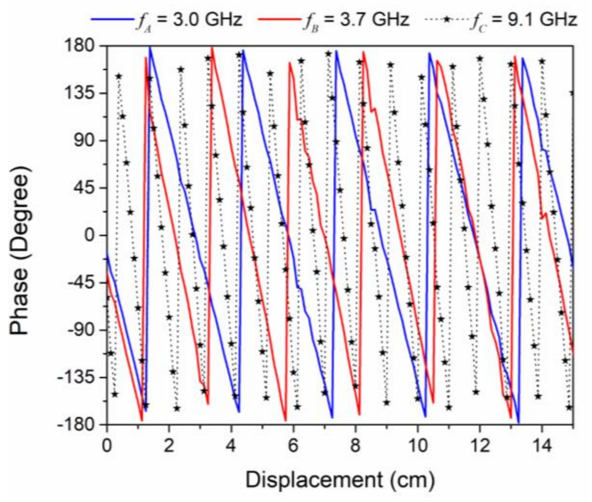

Fig. 4. Variation of the phase of the reflection coefficient with the displacement as inferred by electromagnetic simulation.

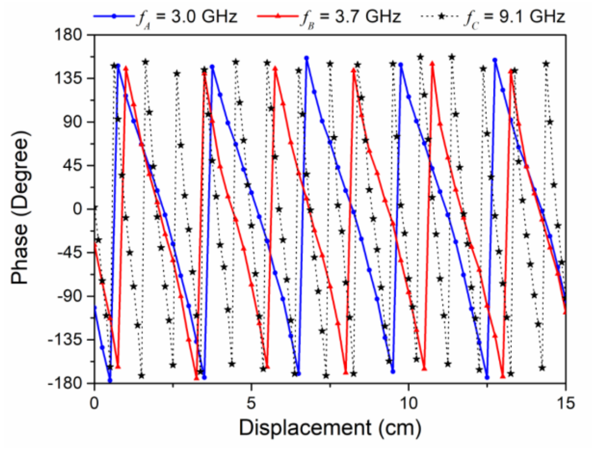

Fig. 5. Variation of the phase of the reflection coefficient with the displacement as inferred from measurement.

4. COMPARATIVE ANALYSIS

To have a perspective of goal achievements in this work, we compare the resolution and dynamic range of the sensor presented in this work with its counterparts in Table I. Comparing to the three preceding works by the authors [24-26], both resolution and dynamic range have been improved in this work simultaneously. In [23] the resolution is very good due to the highly sensitive structure of the sensor, but the dynamic range is small. In other cases which are based on frequency [12,13] or magnitude [17,18] variation, although good resolutions have been reported, the dynamic range is limited, and these sensors can only be used in sub-cm or sub-mm displacement scenarios.

Table 1. Comparison of various linear displacement sensors

Ref.	Resolution (mm)	Dynamic range (cm)
[12]	0.03	0.4
[13]	< 1	0.3
[17]	< 0.2	0.1
[18]	< 0.1	0.07
[23]	0.016	0.5
[24]	0.61	4.4
[25]	0.29	6.2
[26]	5	<14
This Work	**0.14**	**12**

5. CONCLUSION

In conclusion, in this paper, a planar microwave displacement sensor based on phase measurements has been presented and validated. The sensor consists of the reader line, a one-port matched line terminated with a matched load (the static part), and a planar resonant element (made of two back-to-back connected C-shaped loops etched on a movable substrate) exhibiting three resonances. The resonator has been designed such that two resonances (those exhibiting the lower frequencies and present in the low frequency range) are closely spaced, the third resonance being present at a significantly higher frequency. Displacement measurement is based on retrieving the phase of the reflection coefficient at the three frequencies as the movable resonator displaces along the line axis at short vertical distance (0.2 mm in this work). It has been demonstrated that by using the phase of the reflection coefficient measured at the lower frequencies, the dynamic range of the sensor can be enhanced (12 cm in the fabricated prototype), whereas resolution improvement (0.14 mm in the reported sensor) is determined by the phase measured at the higher frequency. In summary, this paper has presented a displacement sensor that combines the ideas of two previous realizations, one focused on resolution improvement, and one devoted to dynamic range optimization. The result has been a sensor where both performance indicators (resolution and dynamic range) have been simultaneously optimized. The sensor exhibits also good linearity and can be applied in scenarios where cm-scale measurements are needed, e.g., motion control, structural health monitoring, servomechanisms, automotive industry, etc.

CONFLICTS OF INTERESTS

The authors declare that they have no conflict of interest.

REFERENCES

[1] E. Eitel, “Basics of rotary encoders: Overview and new technologies,” *Machine Design Magazine*, vol. 4, no. 2, pp. 1-9, 2014.

[2] G. K. McMillan and D. M. Considine, *Process/Industrial Instrument and Control Handbook*, McGRAW-HILL, 1999.

[3] X. Li, J. Qi, Q. Zhang, and Y. Zhang, “Bias-tunable dual-mode ultraviolet photodetectors for photoelectric tachometer,” *Applied Physsics Letters*, vol. 104, 2014, Art. no. 041108, https://doi.org/10.1063/1.4863431.

[4] J. Jezný and M. Curilla, “Position measurement with hall effect sensors,” *American Journal of Mechanical Engineering*, vol. 1, no. 7, pp. 231–235, 2013.

[5] A. H. Karami, F. K. Horestani, M. Kolahdouz, and A. K. Horestani, "Rotation sensor based on magnetic microrods," *IEEE Sensors Journal*, vol. 18, no. 1, pp. 77-82, 2018, https://doi.org/10.1109/JSEN.2017.2771225.

[6] A. H. Karami, F. K. Horestani, M. Kolahdouz, A. K. Horestani, and F. Martín, "2D rotary sensor based on magnetic composite of microrods," *Journal of Materials Science: Materials in Electronics*, vol. 31, pp. 167-174, 2020, https://doi.org/10.1007/s10854-019-02652-8.

[7] X. Zhang, M. Mehrtash, and M. B. Khamesee, “Dual-axial motion control of a magnetic levitation system using hall-effect sensors,” *IEEE/ASME Transactions on Mechatronics*, vol. 21, no. 2, pp. 1129–1139, 2016, https://doi.org/10.1109/TMECH.2015.2479404.

[8] G. Liu, B. Chen, and X. Song, “High-precision speed and position estimation based on Hall vector frequency tracking for PMSM with bipolar hall-effect sensors,” *IEEE Sensors Journal*, vol. 19, no. 6, pp. 2347–2355, 2019, https://doi.org/10.1109/JSEN.2018.2885020.

[9] Z. Zhang, Y. Dong, F. Ni, M. Jin, and H. Liu, “A method for measurement of absolute angular position and application in a novel electromagnetic encoder system,” *Journal of Sensors*, vol. 2015, no. 1, 2015, Art. no. 503852, https://doi.org/10.1155/2015/503852.

[10] Z. Zhang, F. Ni, Y. Dong, M. Jin, and H. Liu, “A novel absolute angular position sensor based on electromagnetism,” *Sensors and Actuators, A: Physical*, vol. 194, pp. 196-203, 2013, https://doi.org/10.1016/j.sna.2013.01.040.

[11] F. Martín, P. Vélez, J. Muñoz Enano, and L. Su, *Planar Microwave Sensors*, 1st ed., Wiley/IEEE Press, 2022.

[12] C. Mandel, B. Kubina, M. Schüßler, and R. Jakoby, "Passive chipless wireless sensor for two-dimensional displacement measurement," in *41st European Microwave Conference*, Manchester, UK, 2011, pp. 79-82, https://doi.org/10.23919/EuMC.2011.6101801.

[13] A. K. Horestani, J. Naqui, Z. Shaterian, D. Abbott, C. Fumeaux, and F. Martín, "Two-dimensional alignment and displacement sensor based on movable broadside-coupled split ring resonators," *Sensors and Actuators A: Physical*, vol. 210, pp. 18-24, 2014, https://doi.org/10.1016/j.sna.2014.01.030.

[14] A. K. Jha, N. Delmonte, A. Lamecki, M. Mrozowski, and M. Bozzi, "Design of microwave-based angular displacement sensor," *IEEE Microwave and Wireless Components Letters*, vol. 29, no. 4, pp. 306-308, 2019, https://doi.org/10.1109/LMWC.2019.2899490.

[15] A. Karami Horestani, F. Paredes, and F. Martín, "Hybrid time/phase/frequency domain linear electromagnetic encoders for displacement sensing and near-field chipless-RFID," *IEEE Journal of Radio Frequency Identification*, vol. 8, pp. 134-144, 2024, https://doi.org/10.1109/JRFID.2024.3366309.

[16] A. Karami Horestani, F. Paredes, and F. Martin, "Enhancing the bit density and capacity in hybrid time/phase domain electromagnetic encoders," in *International Conference on Electromagnetics in Advanced Applications (ICEAA)*, Venice, Italy, 2023, pp. 352-356, https://doi.org/10.1109/ICEAA57318.2023.10297670.

[17] A. Karami Horestani, C. Fumeaux, S. F. Al Sarawi, and D. Abbott, “Displacement sensor based on diamond-shaped tapered split ring resonator,” *IEEE Sensors Journal*, vol. 13, no. 4, pp. 1153–1160, 2013, https://doi.org/10.1109/JSEN.2012.2231065.

[18] A. K. Horestani, J. Naqui, D. Abbott, C. Fumeaux, and F. Martín, “Two-dimensional displacement and alignment sensor based on reflection coefficients of open microstrip lines loaded with split ring resonators,” *Electronics Letters*, vol. 50, no. 8, pp. 620–622, 2014, https://doi.org/10.1049/el.2014.0572.

[19] A. Karami Horestani, F. Paredes, and F. Martín, "Synchronous electromagnetic encoders based on step-impedance resonators," *IEEE Sensors Journal*, vol. 23, no. 19, pp. 22440-22450, 2023, https://doi.org/10.1109/JSEN.2023.3301095.

[20] A. Karami Horestani, F. Paredes, and F. Martín, "Hybrid time/phase domain synchronous electromagnetic encoders for near-field chipless-RFID and motion control applications," *IEEE Transactions on Microwave Theory and Techniques*,

vol. 71, no. 12, pp. 5457-5469, 2023, https://doi.org/10.1109/TMTT.2023.3277934.

[21] A. Karami Horestani, F. Paredes, and F. Martín, "Hybrid time/frequency domain electromagnetic encoders dispenser-printed on PET substrate," in *17th European Conference on Antennas and Propagation (EuCAP)*, Florence, Italy, 2023, pp. 1-5, https://doi.org/10.23919/EuCAP57121.2023.10133254.

[22] A. Karami Horestani, F. Paredes, and F. Martín, "Frequency-coded and programmable synchronous electromagnetic encoders based on linear strips," *IEEE Sensors Letters*, vol. 6, no. 8, 2022, Art. no. 3501704, https://doi.org/10.1109/LSENS.2022.3193329.

[23] J. Muñoz Enano, P. Vélez, L. Su, M. Gil Barba, and F. Martín, "A reflective-mode phase-variation displacement sensor," *IEEE Access*, vol. 8, pp. 189565-189575, 2020, https://doi.org/10.1109/ACCESS.2020.3031032.

[24] A. Karami Horestani, F. Paredes, and F. Martín, "Phase-variation microwave displacement sensor with good linearity and application to breath rate monitoring," *IEEE Sensors Journal*, vol. 23, no. 19, pp. 22486-22495, 2023, https://doi.org/10.1109/JSEN.2023.3307575.

[25] A. Karami Horestani, F. Paredes, and F. Martín, "Phase-variation microwave displacement sensor with high resolution, sensitivity, and dynamic range," in *18th European Conference on Antennas and Propagation (EuCAP)*, 2024, https://doi.org/10.23919/EuCAP60739.2024.10501699.

[26] A. Karami Horestani, F. Paredes, and F. Martín, "Microwave displacement sensor with good linearity and dynamic range based on a microstrip line pair loaded with movable electric-LC resonators," *IEEE Sensors Journal*, vol. 24, no. 13, pp. 20529-20538, 2024, https://doi.org/10.1109/JSEN.2024.3398420.

.

JSST
Journal of Space Science and Technology

P-ISSN: 2008-4560
E-ISSN: 2423-4516

Journal of Space Science and Technology

Vol. 18, Special Issue, pp. 41-51, 2025
https://doi.org/10.22034/JSST.2025.1521
Journal Homepage: https://www.jsstpub.com

Original Research Paper

Numerical Study of V-Shaped Microgrooves Location on an Aerodynamic Surface for Drag Reduction

Mohammad Javad Kahalian[1], Ramin Kamali Moghadam[2]*, Iman Bahman Jahromi[3], and Mahmoud Najafi[4]

1-3. Aerospace Research Institute, Ministry of Science, Research and Technology, Tehran, Iran
4. Mathematical Science Department, Kent State University, USA

ARTICLE INFO

Article History:

Received 17 January 2025
Revised 16 February 2025
Accepted 22 February 2025
Available Online 23 February 2025

Keywords:

Microstructure
Drag reduction
Transverse flow
NACA 8-H-12

ABSTRACT

One important passive technique for drag reduction is the use of microstructured surfaces. In recent years, the advantages of this method have led some airlines to reduce their fuel consumption by installing microstructured films on aircraft. To understand the physics governing microstructures, this article investigates the effect of V-shaped transverse microgrooves on the NACA 8-H-12 airfoil. For this purpose, grooves with a base and height of 150 μm are placed transversely at eight different locations on the airfoil surface and their effects are investigated at zero angle of attack (AoA) and at velocities of 35, 65, and 100 m/s. The results show that vortices trapped within the transverse microgrooves reduce viscous drag by decreasing shear stress magnitude near the peaks and reversing its direction within the valleys. However, the microgrooves also generate pressure drag due to pressure gradients created within and around the structures. The combined effects of these changes in viscous and pressure drag determine the overall change in total drag. Total drag can either increase or decrease depending on the microgrooved surface area, its location on the airfoil, and the freestream velocity. The maximum drag reduction observed in this study was approximately 6%, achieved with two 200 mm microgrooved surfaces located mid-chord on both the suction and pressure sides at 35 m/s.

*Corresponding Author's E-mail: rkamali@ari.ac.ir

How to Cite this Article:
M. J. Kahalian, R. Kamali Moghadam, I. Bahman Jahromi, and M. Najafi, "Numerical study of V-shaped microgrooves location on an aerodynamic surface for drag reduction," *Journal of Space Science and Technology*, Vol. 18, Special Issue, pp. 41-51, 2025, https://doi.org/10.22034/JSST.2025.1521.

1. INTRODUCTION

Drag management is one of the most basic issues facing aerospace designers. While increased drag is desirable in some applications, such as reentry capsules, due to its role in energy dissipation, drag reduction is a primary concern in most aerospace designs. Microstructured surfaces [1] represent an important class of passive drag reduction techniques, which often involve manipulating surface properties such as geometry [2] and roughness [3, 4].

Walsh [5, 6, 7, 8] pioneered the study of drag reduction by ribbed surfaces. He investigated the different behavior of surfaces with bladed, scalloped and triangular riblets and showed that the symmetrical V-shaped structure had the best effect in drag reduction. Bechert et al. [9,10] investigated different configurations of bladed, scalloped, and sharkskin-like blades. They also conducted an experimental investigation into viscous reduction methods using ribbed surfaces. Djenidi and Antonia [11] measured the drag reduction effect of the V-shaped groove through experiments and found that the drag reduction effect is related to the peak-to-peak distance. Debisschop and Nieuwstadt [12] experimentally investigated the groove effect and found that in the presence of a adverse pressure gradient, the drag reduction can be as high as 13%. Duan and Choudhari [13] found by direct numerical simulation that the drag reduction mechanism proposed for incomprisible flows can still apply for high-speed boundary layers. Chu and Karniadakis [14] studied the drag reduction effect of transverse grooves under different Reynolds numbers. They found that the drag reduction was greater at higher Reynolds numbers. Ahmadi-Baloutaki et al. [15] investigated the effect of the groove surface on turbulence through experimental measurements and found that the presence of a groove increases the boundary layer thickness. Wang et al. [16] conducted a comparative study between simulation and experiment on transverse grooves and observed that a vortex structure is formed inside the transverse grooves. Sutardi and Widodo [17] evaluated the behaviour of the laminar sub-layer in a turbulent boundary using a hot-wire anemometer system. The results showed that no significant differences in the streamwise mean velocity, steamwise turbulence intensity, and velocity signals for the smooth and grooved wall cases. However, the energy spectra for the grooved wall case is slightly lower than that on the smooth wall case. The flow fields over a riblet surface with semicircular grooves were investigated using the synchronized smoke-wire method and the velocity field measurement techniques by Li and Li [18]. They studied how vortices behaved under conditions of decreasing and increasing drag, as well as the effect of the distance between the riblets and observed that if most of the streamwise vortices remained above the riblets, the flow above the riblet valley would be sufficiently calm and drag would decrease. However, if the riblet spacing was large enough that most of the streamwise vortices remained inside the riblet valley (high-velocity flows could penetrate the valleys), drag would increase.

In recent years, Guler et al. [19] used triangular riblets on the suction side of the NACA 0018 airfoil to improve its aerodynamic performance. They observed that the presence of riblet structures increased the lift coefficient and concurrently delayed the stall angle by up to 19°. Notably, the ribbed structures effectively mitigated the interaction between the laminar separation bubble and trailing-edge separation, resulting in reduced turbulent kinetic energy. Li et al. [20] used large eddy simulation (LES) to investigate the vortex structures on a ribbed surface with varying protrusion heights. They observed that the drag reduction rate increased from 3.4% when the ribs were completely submerged within the turbulent boundary layer to 7.9% when the protrusion height reached 11.2. Li et al. [21] investigated the use of transverse grooves on micro air vehicles airfoils to reduce viscous drag. By considering overall aerodynamic performance, they designed a grooved airfoil that demonstrated a 33.747% improvement in lift-to-drag ratio compared to the smooth airfoil. Pakatchian et al.'s review paper [22] is devoted to the application of riblets in the aviation industry, focusing on studies conducted in wind tunnels, flight tests, and using numerical techniques. Bliamis et al. [23] examined various blade-shaped riblet designs for use on Unmanned Aerial Vehicles. They concluded that riblets with a width-to-height ratio of 1 ($s/h = 1$) provided the best drag reduction, whereas those with the largest width ($s/h = 2$) performed poorly and exhibited exceptionally high wall shear stresses.

To elucidate the physics governing microstructured surfaces, this article investigates the aerodynamic parameters resulting from airflow over such surfaces, including drag components, velocity profiles, and shear stress. While most of the previous studies on transverse microstructures have frequently attributed drag reduction to velocity slip above the structures or a reduction in viscous drag, this work demonstrates, through analysis of shear stress distributions, that the negative viscous drag within the microgroove valleys, in addition to reduced shear stress near the peaks, contributes significantly to overall drag reduction. Furthermore, a review of the literature reveals a lack of consensus regarding the underlying physics and parametric influences of microstructures, highlighting the need for further data. Therefore, the novel aspect of this study is the investigation of V-shaped microgroove placement at various locations on an NACA 8-H-12 airfoil. Specifically, microgrooves of uniform base and height are positioned at eight distinct locations on the smooth airfoil, and the resulting drag components are analyzed at AoA = 0 and velocities of 35, 65, and 100 m/s. These results are then compared with those obtained from the smooth airfoil under identical conditions.

2. PROBLEM DEFINITION

In this section, the geometry of the airfoil and microgrooves, the locations of microgrooved surfaces on the airfoil, mesh properties, governing equations and solution method are presented. Finally, the validation of the solution method and its independence from the mesh are investigated.

2.1 Geometry and mesh

As mentioned and shown in Fig.1, V-shape transverse microgrooves with base and height of 150 µm are used in this study. These microgrooves are placed on eight different locations on the surface of the NACA 8-H-12 airfoil with chord of 220 mm, each location being identified by a unique code. Table 1 details the location of the microgrooves and corresponding case codes.

The coding system is as follows: the first part indicates on which side of the airfoil the microgrooved film is located (S for suction side, P for pressure side, SP for both); the second part indicates the film's position along the chord, relative to its center (M for symmetrical at the chord center, F for front of the airfoil, R for rear of the airfoil); and the final part represents the length of the microgrooved surface in millimeters.

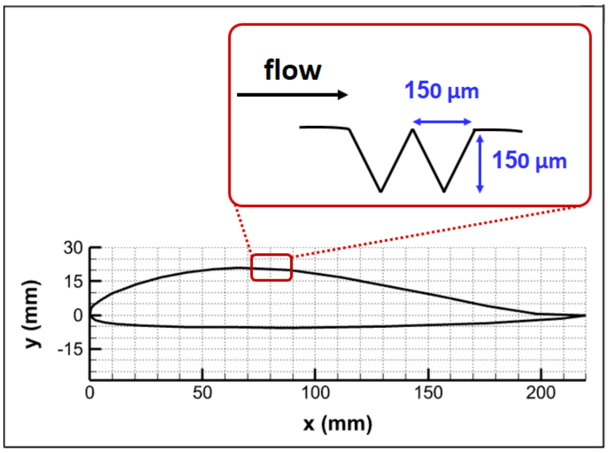

Fig. 1. Geometry of transverse microgrooves and NACA 8-H-12 airfoil.

Table 1. Location of the microgrooved surface.

Code	Location of microgrooves
SMOOTH	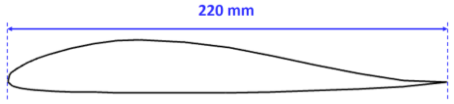
S-M-100	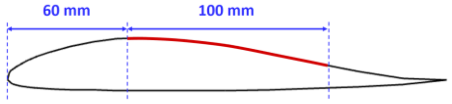
S-F-100	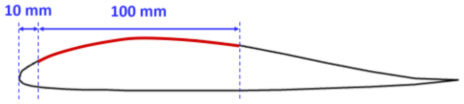
S-R-100	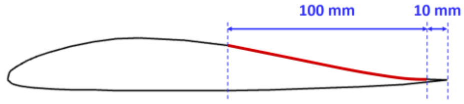
SP-F-200	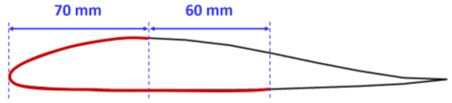
SP-R-200	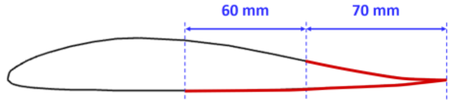
S-M-200	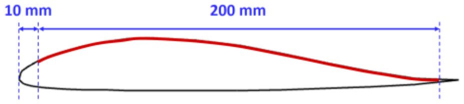
P-M-200	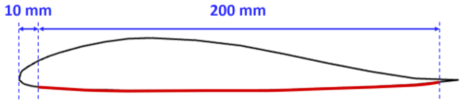
SP-M-400	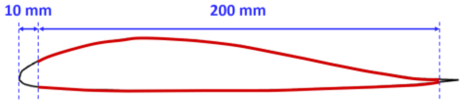

The computational domain was discretized using an unstructured mesh with several boundary layer cells. On the microgrooved surfaces, the first cell height was approximately 24 µm, with a typical cell length of 9 µm. Fig.2 presents the Y-Plus distribution of the microgrooved surface for the S-M-100 case.

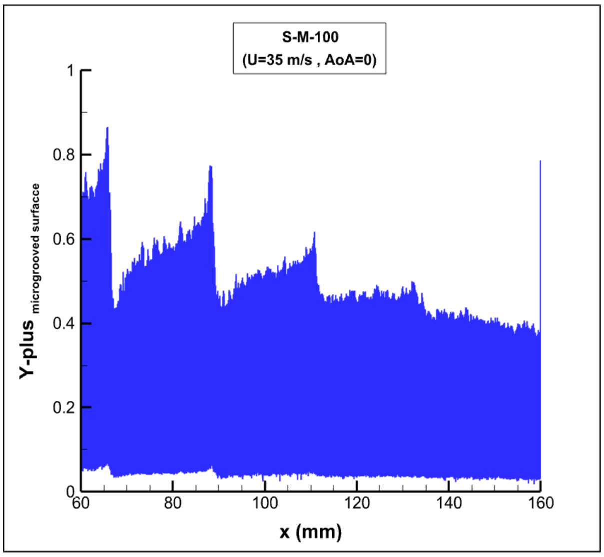

Fig. 2. Y-plus of the S-M-100 case.

2.2 Governing equations

The Knudsen number is a criterion of flow continuity that can be calculated from Eq. (1) [24].

$$Kn = \sqrt{\frac{\pi\gamma}{2}}\frac{Ma}{Re} \tag{1}$$

In this relation, γ represents the specific heat ratio, Ma the Mach number and Re the Reynolds number. Based on the size of the microgrooves, the maximum value of the Knudsen number is approximately equal to 4.3×10^{-4}; therefore considering the range of application of the Navier Stokes equations, these equations can be used in this study.

On the other hand, the primary mechanism for drag reduction in transverse microstructures is the generation of vortices within the structures, which causes local turbulence. Therefore, by using an appropriate mesh, some RANS models are able to capture local vortices and their effects. For example references [21,25,26] have also used some of these models. Considering the use of the RANS approach, the mass and momentum conservation equations are respectively [27]:

$$\frac{\partial \rho u_j}{\partial x_j} = 0 \tag{2}$$

and

$$\begin{aligned}\frac{\partial \rho u_i}{\partial t} + \frac{\partial}{\partial x_j}(\rho u_i u_j) &= -\frac{\partial p}{\partial x_i} + \mu\frac{\partial^2 u_i}{\partial x_j \partial x_j} \\ &- \frac{\partial}{\partial x_j}\left(\frac{2}{3}\rho k \delta_{ij} - \mu_t\left(\frac{\partial u_i}{\partial x_j} + \frac{\partial u_j}{\partial x_i}\right)\right)\end{aligned} \tag{3}$$

where u_i represents the average velocity vector component, p the average pressure, k the turbulence kinetic energy, δ_{ij} the Kronecker delta, μ the dynamic viscosity, and μ_t the turbulence viscosity. μ_t is calculated using turbulence models, and in this study, the k-ω SST model is employed. According to this model, the turbulence viscosity is obtained using the following relations [28, 29]:

$$\mu_t = \frac{\rho a_1 k}{max(a_1\omega\,, \sqrt{2}S_t F_2)} \tag{4}$$

In above equation, a_1 is a constant, ω is the specific turbulent dissipation rate, and S_t is the magnitude of the strain rate. k, ω, and F_2 are also calculated using the following relations:

$$\frac{\partial}{\partial t}(\rho k) + \frac{\partial}{\partial x_i}(u_i \rho k) = \frac{\partial}{\partial x_j}\left(\mu_k \frac{\partial}{\partial x_j}k\right) + \tilde{P}_k - \beta^* \rho \omega k \tag{5}$$

and

$$\begin{aligned}\frac{\partial}{\partial t}(\rho\omega) + \frac{\partial}{\partial x_i}(u_i \rho \omega) &= \frac{\partial}{\partial x_j}\left(\mu_\omega \frac{\partial}{\partial x_j}\omega\right) + P_\omega - \beta\rho\omega^2 \\ &+2\rho(1-F_1)\frac{1}{\omega}\frac{1}{\sigma_{\omega,2}}\frac{\partial}{\partial x_j}k\frac{\partial}{\partial x_j}\omega\end{aligned} \tag{6}$$

and

$$F_2 = tanh\left[\left[max\left(2\frac{\sqrt{k}}{\beta^*\omega(d_\perp)}, \frac{500\mu}{\rho\omega(d_\perp)^2}\right)\right]^2\right] \tag{7}$$

In these relations μ_k and μ_ω are the effective viscosities, $\tilde{P}_k$ is the effective rate of production of k, P_ω is the rate of production of ω, $d_\perp$ is the shortest distance to the near wall, β and β^* and $\sigma_{\omega,2}$ are the turbulence modeling constants, and finally F_1 is the blending function. In this study, Ansys Fluent was used to numerically solve the governing equations.

2.3 Validation of method and mesh independency

In order to validate the numerical methodology, flow over a NACA 0012 airfoil was simulated and the computed pressure and drag coefficients were compared with the experimental data reported in [30]. The airfoil chord was 67 cm, the freestream velocity is 55.35 m/s, and the AoA varied from 0° to 10°.

Figure 3 and Fig.4 show the pressure and drag coefficients, respectively. The good agreement between the present numerical results and the experimental data, as shown in these figures, validates the accuracy of the numerical methodology.

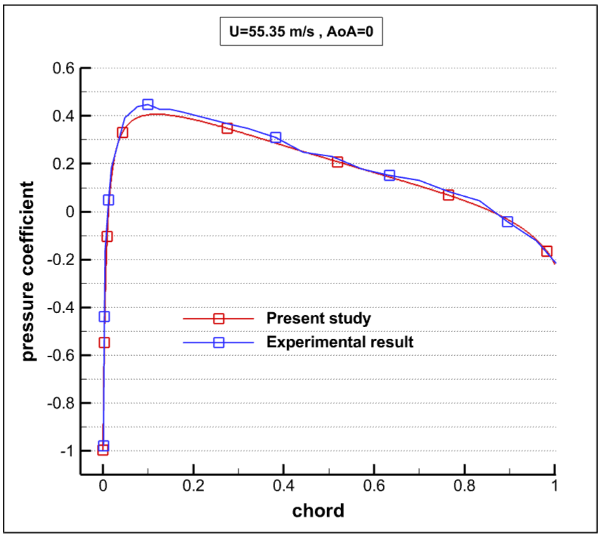

Fig. 3. Comparison of the pressure coefficients.

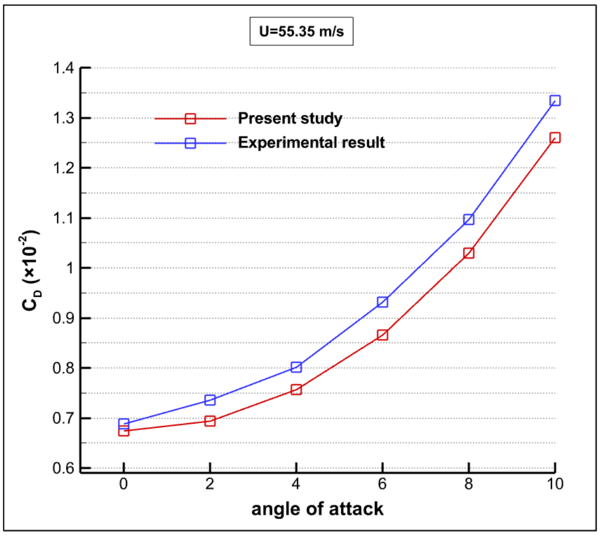

Fig. 4. Comparison of the drag coefficients.

In order to select the appropriate mesh size, four different cases were compared on the S-M-100, and finally a mesh with the mentioned specifications (section 2.1) was selected. The drag coefficients for these four cases can be seen in Fig. 5.

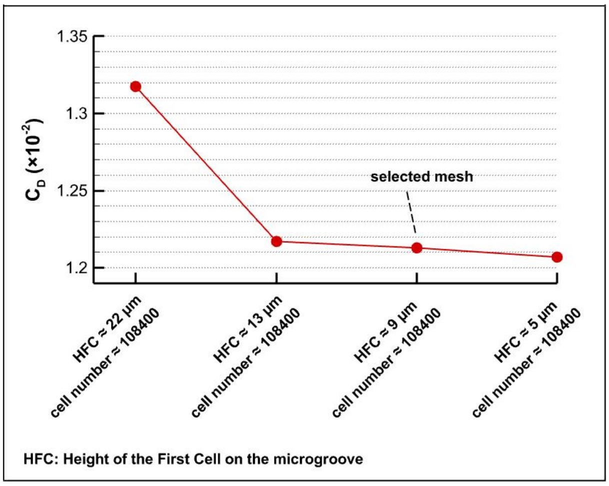

Fig. 5. Comparison of the drag coefficient, in order to investigate the independence of solution from the mesh.

3. RESULTS AND DISCUSSION

The results of this study are presented in three sections. The first section explains the mechanism by which transverse microgrooves reduce viscous drag. The second section discusses the influence of microgrooves on pressure drag generation. Finally, the third section presents the overall drag variation and the trends observed for each drag component

3.1 Mechanism of viscous drag reduction on microgrooved surface

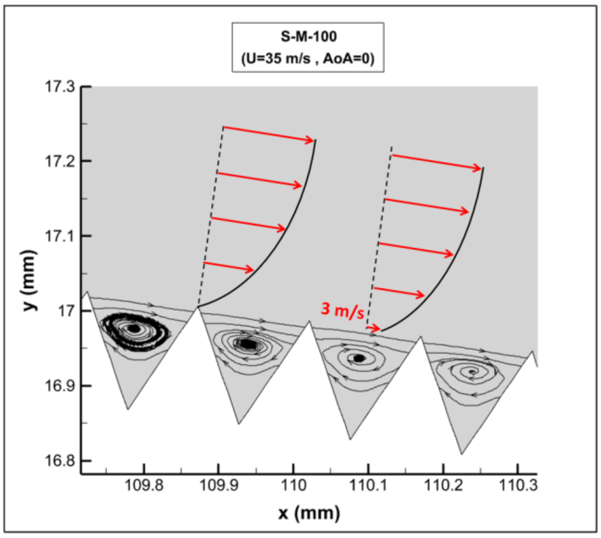

Fig. 6. Streamlines inside the microgrooves.

Figure 6 shows the streamlines for the case S-M-100 at a velocity of 35 m/s. The formation of a vortex within the microgroove causes the flow to slip over the vortex, which can be seen by comparing the profiles of velocity in Fig. 6. According to this figure, the slip velocity on the vortices in the middle of the suction side of the airfoil is approximately 3 m/s.

In describing the mechanism of viscous drag reduction, some researchers have emphasized the flow slippage on the vortex. In this article, the change in the magnitude and direction of shear stress is described as the primary mechanism of drag reduction. The equation for calculating viscous drag in the present study is [31]:

$$D_v = \int_{x_1}^{x_2} \tau_x dx \tag{8}$$

where τ_x is the shear stress in the direction of the freestream flow. Fig. **7** shows τ_x at the middle of the suction side of airfoil for the two cases of S-M-100 and smooth. In this figure, the shear stress magnitudes of the microgrooves are lower than those of the smooth surface. Furthermore, since the direction of the vortex trapped within the groove is opposite to the direction of the flow above it, the shear stress in this region becomes negative.

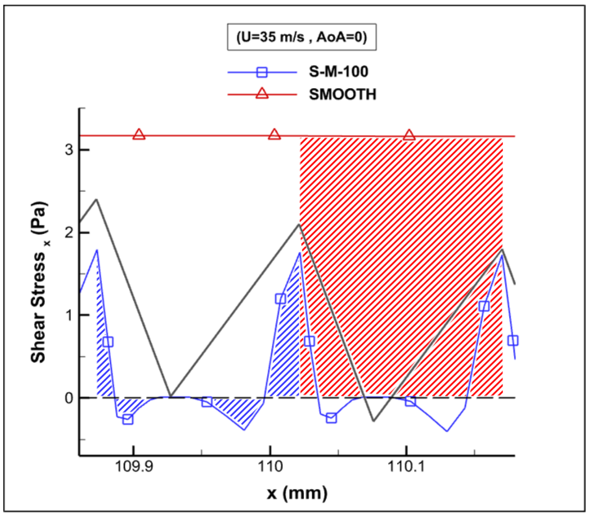

Fig. 7. Shear stress in x direction for smooth airfoil and the S-M-100 case.

According to Eq. (8), the viscous drag is calculated from the area between the graph of τ_x and the x-axis. As a result, according to Fig. 7, the decrease in the shear stress around the peak and the increase in its magnitude inside the valley (with a negative sign) leads to a decrease in the viscous drag.

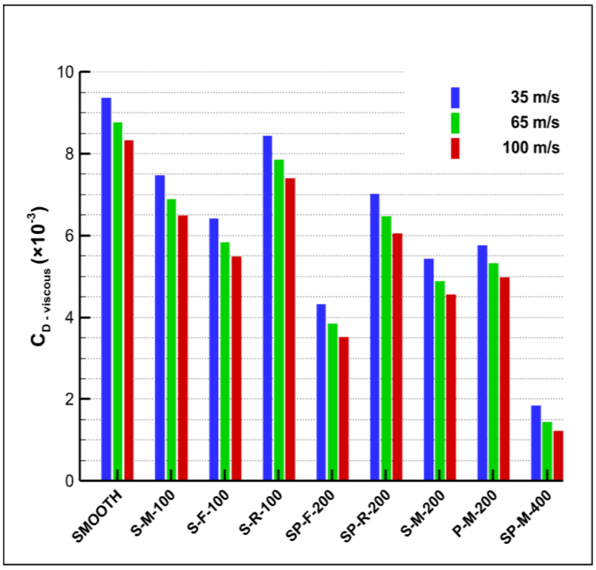

Fig. 8. Comparison of the viscous drag coefficients.

Figure 8 presents the viscous drag coefficient of different cases. According to this figure, the presence of microgrooves has reduced the viscous drag in all cases, but the amount of reduction does not depend only on the length of the microgrooved surface but also depends on its location. For example, placing 100 mm of microgrooves on the suction side and near the leading edge (S-F-100) has a greater drag reduction than placing the grooves in the middle of the airfoil (S-M-100) and also near the trailing edge (S-R-100). As another example, placing 100 mm of microgrooves on the suction side and near the leading edge (S-F-100) will reduce drag more than placing 200 mm of microgrooves around the trailing edge (SP-R-200). The trend of viscous drag reduction is similar at all three velocities, and the greatest reduction occurs in case SP-M-400.

3.2 The effect of microgrooves on the pressure drag

The use of microstructures on a smooth surface generates pressure drag, which is due to the pressure difference inside and around the structures, that ultimately creates resistance to fluid movement. Figure 9 shows the pressure difference generates around the microgrooves by comparing the static pressure on the smooth airfoil and case S-M-100.

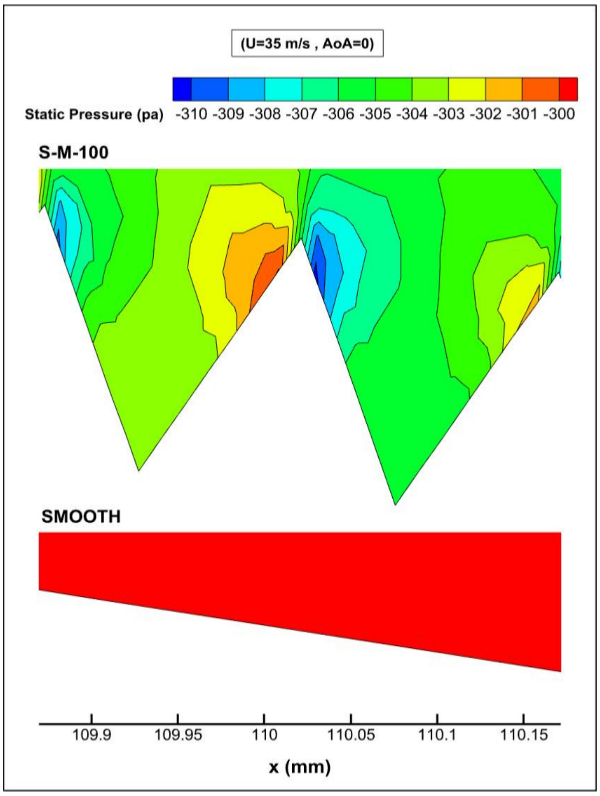

Fig. 9. Comparison of the static pressure.

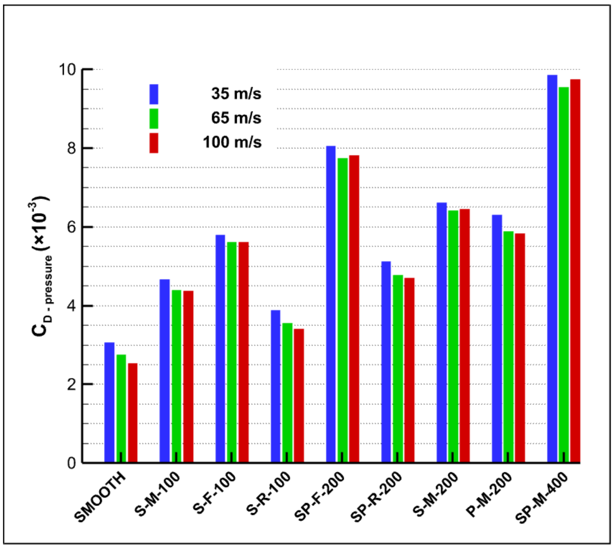

Fig. 10. Comparison of the pressure drag coefficients.

Figure 10 shows the pressure drag coefficient of different cases. In all cases, the presence of microgrooves increased the pressure drag compared to the smooth airfoil. Similar to viscous drag, the increase in pressure drag does not depend only on the length of the microgrooved surface but also depends on its location. It is noteworthy that the trend of pressure drag increase in different cases exactly follows the trend of viscous drag decrease, so that case SP-M-400, which had the largest amount of viscous drag reduction, also had the largest increase in pressure drag.

3.3 The effect of microgrooves on the total drag

The overall drag variation is determined by the combined effects of the changes in viscous and pressure drag. Figure 11 illustrates the variation of the drag components and the total drag relative to the smooth airfoil at U=35 m/s. These changes were calculated using the following equation [32].

$$\eta_t = \frac{D_{str}-D_{smh}}{D_{smh}}\times 100 = \frac{D_{str-v}-D_{smh}}{D_{smh}}\times 100 - \frac{D_{str-p}}{D_{smh}}\times 100 = \eta_v+\eta_p \tag{9}$$

Where D represents drag and η represents the percentage change relative to the smooth airfoil. The subscripts smh, str, p, v and t denote the smooth airfoil, microstructured airfoil, pressure component, viscous component, and total change, respectively.

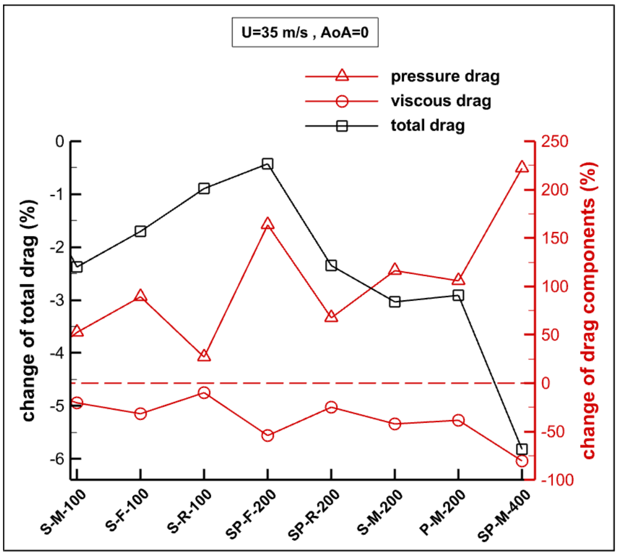

Fig. 11. The amount of change of drag components and total drag relative to the smooth airfoil.

As previously noted, the largest reduction in viscous drag occurs in case SP-M-400, which according to Fig. 11 is more than 80% (relative to the smooth airfoil). Conversely, the pressure drag increases by more than 220% (relative to the smooth airfoil). According to Fig. 12 for the smooth airfoil, the viscous component contributes approximately 75% of the total drag. Therefore, an 80% reduction in viscous drag can overcome a 220% increase in pressure drag, resulting in a total drag reduction of approximately 5%.

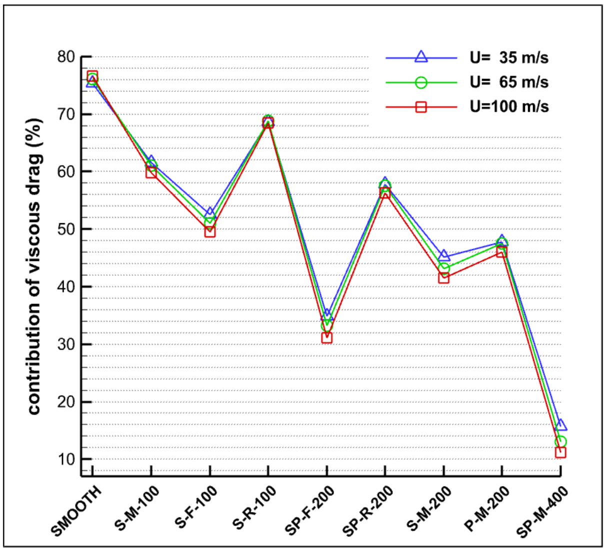

Fig. 12. Contribution of the viscous drag to the total drag.

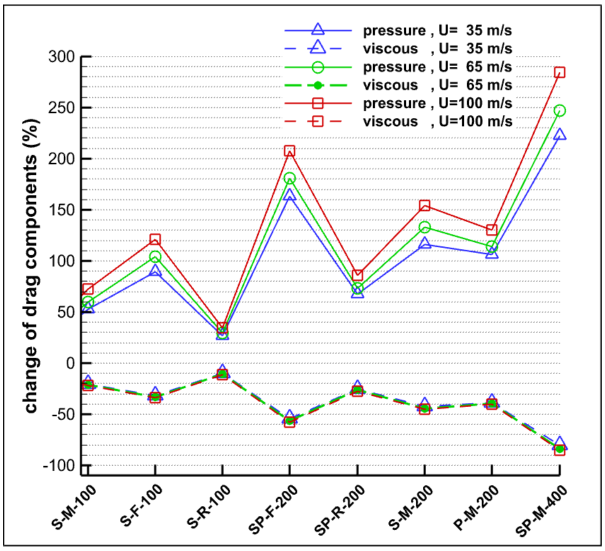

Fig. 13. The amount of change of drag components relative to the smooth airfoil at different velocities.

Figure 13 shows the change in the viscous drag and the pressure drag components of different cases at three freestream velocities of 35, 65 and 100 m/s. As can be seen, the trends in drag component variation are consistent across these velocities. Furthermore, a greater decrease in viscous drag correlates with a greater increase in pressure drag for each configuration, and these trends are consistent across all three velocities. On the other hand, in each case where the viscous drag decreases more, the pressure drag increases more, and these trends are the same for all three velocities. It is interesting to note that the trend of viscous drag change in Fig. 13 is similar to the trend of contribution in Fig. 12 In other words, a larger decrease in viscous drag is equivalent to a smaller contribution of this component to the total drag.

Figure 14 shows the variation in total drag for different cases and at freestream velocities of 35, 65 and 100 m/s. While total drag is the sum of the viscous and pressure drag components, its trend does not necessarily follow that of either component. Furthermore, despite similar trends in the variation of the drag components across the different velocities, the total drag variation differs at each velocity. As shown in Fig. 14, at 35 m/s and 65 m/s, the greatest drag reduction, approximately 6% and 4.5% respectively, is observed for the SP-M-400 case. However, at 100 m/s, the total drag for this configuration increases by approximately 1%. At this higher velocity, the greatest drag reduction, approximately 1%, is achieved by the SP-R-200. In general, a reduction in viscous drag does not guarantee a reduction in total drag. As in many cases, the use of microgrooves increased the total drag, and the amount of increase was greater at higher velocities.

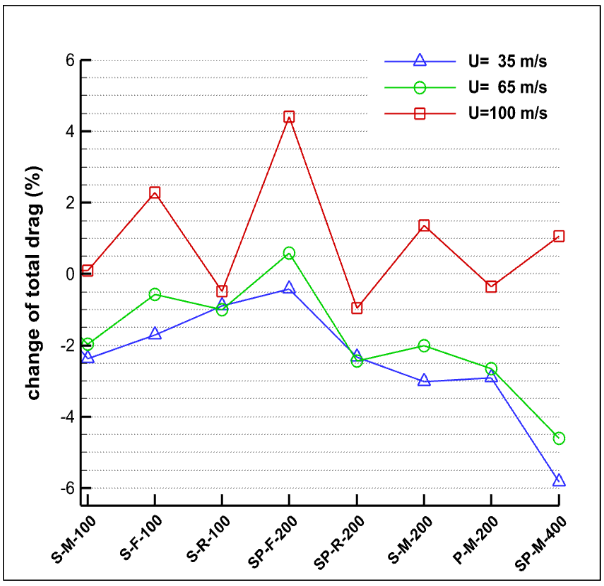

Fig. 14. The amount of change of total drag relative to the smooth airfoil at different velocities.

3.4 The effect of microgrooves on the lift

While this study focuses on drag variation, this section briefly examines the observed changes in lift. As shown in Fig. 15, across all tested velocities, placing the microstructures near the leading edge (cases S-F-100 and SP-F-200) results in a small reduction in lift (less than 1%) compared to the smooth airfoil. The two largest lift increases are observed when the microstructures are positioned near the trailing edge (cases S-R-100 and SP-R-200). For case SP-M-400, which exhibits the greatest drag reduction at 35 and 65 m/s, the change in lift is negligible, increasing by less than 1%. Conversely, case SP-R-200, which shows the greatest drag reduction at 100 m/s, also experiences the largest lift increase, approximately 3.4%.

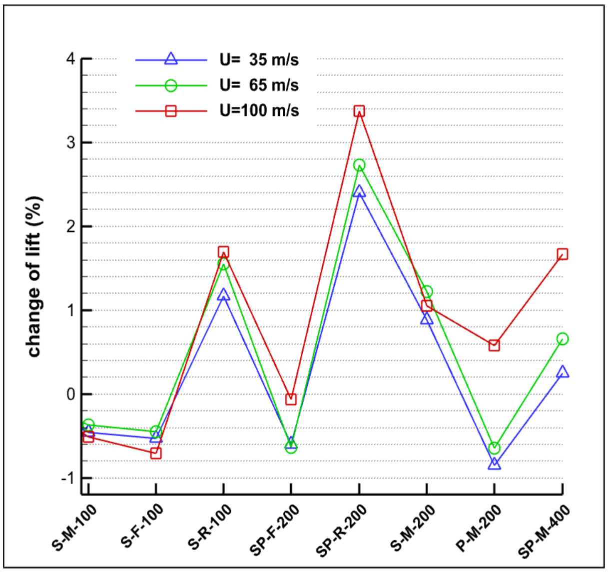

Fig. 15. The amount of change of lift relative to the smooth airfoil at different velocities.

4. CONCLUSION

This study investigates the drag reduction mechanism of V-shaped transverse microgrooves and their influence on the drag components of a NACA 8-H-12 airfoil. For this purpose, grooves with base and height of 150 µm were placed at eight different locations of the smooth airfoil with a chord of 220 mm and the drag components were investigated at AoA=0 and at velocities of 35, 65 and 100 m/s. The drag components of the microgrooved airfoils were then compared with those of the smooth airfoil under identical conditions.

The results revealed that the vortices trapped within the transverse microgrooves reduce viscous drag by decreasing the magnitude of shear stress near the peaks and altering its direction within the valleys. On the other hand, due to the pressure difference within and around the structures and ultimately the resistance to fluid movement, the use of transverse microgrooves leads to an increase in the pressure drag. The overall drag variation is then determined by the combined effects of these changes in viscous and pressure drag.

The results further indicate that the total drag can either increase or decrease depending on the microgrooved surface area, its location on the airfoil, and the freestream velocity. The maximum drag reduction observed, approximately 6%, occurred with two 200 mm microgrooved surfaces located in the mid-chord on both the suction and pressure sides at a velocity of 35 m/s.

Across the studied cases, the trend of increasing pressure drag mirrored the trend of decreasing viscous drag; the configuration exhibiting the largest decrease in viscous drag also experienced the greatest increase in pressure drag. This correlation was consistent across all three velocities (35, 65, and 100 m/s). Furthermore, the trend of the viscous component's contribution to total drag followed the same trend as the change in viscous drag itself. However, the trend in total drag variation did not necessarily align with the trends observed for either viscous or pressure drag. Total drag reduction was more prevalent at lower velocities, while at higher velocities, total drag increased in most configurations.

The AoA influences total drag by affecting its components and the flow separation point. Therefore, the increase or decrease of the drag is dependent on the AoA. Hence, a study on this relationship could be a topic for future research.

CONFLICT OF INTERESTS

The authors declare that they have no conflict of interest.

REFERENCES

[1] G. D. Bixler and B. Bhushan, “Fluid drag reduction with shark-skin riblet inspired microstructured surfaces,” *Advanced Functional Materials*, vol. 23, no. 36, pp. 4507-4528, 2013, https://doi.org/10.1002/adfm.201203683.

[2] E. M. Fayyadh and N. M. Mahdi, “Effect of riblets geometry on drag reduction,” in *International Mechanical Engineering Congress and Exposition. Volume 7: Fluids and Heat Transfer, Parts A, B, C, and D*, Houston, Texas, USA, 2012, pp. 87-100, https://doi.org/10.1115/IMECE2012-85228.

[3] A. C. Kah Poh, C. See Yuan, A. K. Mat Yamin, A. J. Jalaluddin, I. S. Ishak, and S. Mansor, “Effect of surface roughness on drag of loggerhead carapace,” *Jurnal Mekanikal*, vol. 26, no. 2, pp. 37–48, 2018.

[4] T. S. Surwase and D. R. Vaidya, “Study of effect of surface roughness on drag,” in *Mechanical Engineering PG Conference*, MAEER’s MIT, United States, 2015, pp. 149–154.

[5] M. Walsh, “Turbulent boundary layer drag reduction using riblets,” in *20th Aerospace Sciences Meeting*, Orlando, FL, USA, 1982, https://doi.org/10.2514/6.1982-169.

[6] M. J. Walsh, “Drag characteristics of V-groove and transverse curvature riblets,” in *Symposium on Viscous Drag Reduction*, Dallas, TX, 1979, Paper 19810042106.

[7] M. J. Walsh, “Riblets as a viscous drag reduction technique,” *AIAA Journal*, vol. 21, no. 4, pp. 485-486, 1983, https://doi.org/10.2514/3.60126.

[8] M. J. Walsh, “Effect of detailed surface geometry on riblet drag reduction performance,” *Journal Aircraft*, vol. 27, no. 6, 1990, https://doi.org/10.2514/3.25323.

[9] D. W. Bechert, M. Bruse, and W. Hage, “Experiments with three-dimensional riblets as an idealized model of shark skin,” *Experiments in Fluids*, vol. 28, no. 5, pp. 403–412, 2000, https://doi.org/10.1007/s003480050400.

[10] D. W. Bechert, M. Bruse, W. Hage, J. G. T. Van Der Hoeven, and G. Hoppe, “Experiments on drag-reducing surfaces and their optimization with an adjustable geometry,” *Journal of Fluid Mechanics*, vol. 338, pp. 59–87, 1997, https://doi.org/10.1017/S0022112096004673.

[11] L. Djenidi and R. A. Antonia, “Laser Doppler anemometer measurements of turbulent boundary layer over a riblet surface,” *AIAA Journal*, vol. 34, no. 5, 1996, https://doi.org/10.2514/3.13180.

[12] J. R. Debisschop and F. T. M. Nieuwstadt, “Turbulent boundary layer in an adverse pressure gradient: Effectiveness of riblets,” *AIAA Journal*, vol. 34, no. 5, 1996, https://doi.org/10.2514/3.13170.

[13] L. Duan and M. Choudhari, “Effects of riblets on skin friction and heat transfer in high-speed turbulent boundary layers,” in *50th AIAA Aerospace Sciences Meeting Including the New Horizons Forum and Aerospace Exposition*, Nashville, Tennessee, 2012, Paper 2012-1108, https://doi.org/10.2514/6.2012-1108.

[14] D. C. Chu and G. E. Karniadakis, “A direct numerical simulation of laminar and turbulent flow over riblet-mounted surfaces,” *Journal of Fluid Mechanics*, vol. 250, pp. 1-42, 1993, https://doi.org/10.1017/S0022112093001363.

[15] M. Ahmadi Baloutaki, R. Carriveau, and D. S. K. Ting, “Effect of free-stream turbulence on flow characteristics over a transversely-grooved surface,” *Experimental Thermal and Fluid Science*, vol. 51, pp. 56-70, 2013, https://doi.org/10.1016/j.expthermflusci.2013.07.001.

[16] B. Wang, J. Wang, G. Zhou, and D. Chen, “Drag Reduction by Microvortexes in Transverse Microgrooves,” *Advances in Mechanical Engineering*, vol. 6, 2014, https://doi.org/10.1155/2014/734012.

[17] S. Sutardi and W. A. Widodo, “Analysis of turbulence characteristics in the laminar sub-layer region of a perturbed turbulent boundary layer,” *Applied Mechanics and Materials*, vol. 836, pp. 115-120, 2016, https://doi.org/10.4028/www.scientific.net/AMM.836.115.

[18] S. J. Lee and S. H. Lee, “Flow field analysis of a turbulent boundary layer over a riblet surface,” *Experiments in Fluids*, vol. 30, pp. 153–166, 2001, https://doi.org/10.1007/s003480000150.

[19] E. Güler, E. Pınar, and T. Durhasan, “The effect of riblets on the aerodynamic performance of NACA 0018 airfoil,” *Cukurova University Journal of the Faculty of Engineering*, vol. 39, no. 1, pp. 119–132, 2024, https://doi.org/10.21605/cukurovaumfd.1459405.

[20] Z. LI *et al.*, “Numerical study on influence of protrusion heights on Reynolds stress and viscous stress variations in turbulent vortical structures,” *Chinese Journal of Aeronautics*, vol. 37, no. 9, pp. 59-71, 2024, https://doi.org/10.1016/j.cja.2024.05.019.

[21] Z. Li *et al.*, “A numerical study on the influence of transverse grooves on the aerodynamic performance of micro air vehicles airfoils,” *Applied Sciences*, vol. 13, no. 22, 2023, Art. no. 12371, https://doi.org/10.3390/app132212371.

[22] M. R. Pakatchian, J. Rocha, and L. Li, “Advances in riblets design,” *Applied Sciences*, vol. 13, no. 19, 2023, Art. no. 10893, https://doi.org/10.3390/app131910893.

[23] C. Bliamis, Z. Vlahostergios, D. Misirlis, and K. Yakinthos, “Numerical simulation of blade-shaped riblets using LES based methods,” *Chemical Engineering Transactions*, vol. 103, pp. 481–486, 2023, https://doi.org/10.3303/CET23103081.

[24] S. Varoutis, S. Naris, V. Hauer, C. Day, and D. Valougeorgis, “Computational and experimental study of gas flows through long channels of various cross sections in the whole range of the Knudsen number,” *Journal of Vacuum Science & Technology A*, vol. 27, no. 1, pp. 89–100, 2009, https://doi.org/10.1116/1.3043463.

[25] Z. Wu, S. Li, M. Liu, S. Wang, H. Yang, and X. Liang, “Numerical research on the turbulent drag reduction mechanism of a transverse groove structure on an airfoil blade,” *Engineering Applications of Computational Fluid Mechanics*, vol. 13, no. 1, pp. 1024-1035, 2019, https://doi.org/10.1080/19942060.2019.1665101.

[26] M. E. Benhamza and F. Belaid, “Computation of turbulent channel flow with variable spacing riblets,” *Mechanika*, vol. 79 , no. 5, pp. 36–41, 2009.

[27] S. N. A. Yusof, Y. Asako, N. A. C. Sidik, S. B. Mohamed, and W. M. A. A. Japar, “A short review on RANS turbulence models,” *CFD Letters*, vol. 12, no. 11, pp. 83-96, 2020, https://doi.org/10.37934/cfdl.12.11.8396.

[28] F. Moukalled, L. Mangani, and M. Darwish, *The Finite Volume Method in Computational Fluid Dynamics*, Springer, 2016. https://doi.org/10.1007/978-3-319-16874-6.

[29] P. A. Costa Rocha, H. H. Barbosa Rocha, F. O. Moura Carneiro, M. E. Vieira da Silva, and A. V. Bueno, “K-ω SST (shear stress transport) turbulence model calibration: A case study on a small scale horizontal axis wind turbine,” *Energy*, vol. 65, pp. 412-418, 2014, https://doi.org/10.1016/j.energy.2013.11.050.

[30] N. Gregory and C. L. O’Reilly, “Low-speed aerodynamic characteristics of NACA 0012 aerofoil section, including the effects of upper-surface roughness simulating hoar frost,” AERADE Aeronautical Research Council, London, Rep. R & M. No. 3726, 1970.

[31] J. D. Anderson, *Fundamentals of Aerodynamics*, 2nd ed., McGraw-Hill Companies, 1991.

[32] Z. Li, Y. Zuo, H. Lu, L. He, and B. Meng, “Numerical study on the influence of top and valley shape of the transverse groove on the drag reduction rate,” *Journal of Theoretical and Applied Mechanics*, vol. 61, no. 4, pp. 741-754, 2023, https://doi.org/10.15632/jtam-pl/171470.

JSST Journal of Space Science and Technology

P-ISSN: 2008-4560
E-ISSN: 2423-4516

Journal of Space Science and Technology

Vol. 18, Special Issue, pp. 52-59, 2025
https://doi.org/10.22034/JSST.2025.1525
Journal Homepage: https://www.jsstpub.com

Original Research Paper

Boundary Layer Transition and Re-Laminarization in the Nozzle of a Shock Tunnel–a Numerical Study

Shahed Malekipour[1], Iman Bahman Jahromi[2], and Meisam Mohammadi Amin[3]*

1,2. Aerospace Research Institute, Ministry of Science, Research and Technology, Tehran, Iran
3. Technical University of Denmark

ARTICLE INFO

Article History:

Received 21 January 2025
Revised 07 February 2025
Accepted 16 February 2025
Available Online 23 February 2025

Keywords:

Boundary layer transition
Computational fluid dynamics
Hypersonic nozzle flow
Nozzle starting flow
Shock tunnel

ABSTRACT

The boundary layer behavior in hypersonic nozzle of a shock tunnel has been investigated by means of the computational fluid dynamics simulations. The state of boundary layer at the nozzle outlet can highly affect the downstream flow passing around the test model in the shock tunnel test section. Focusing on the transitional boundary layer simulation, results of the optimal nozzle's steady-state flow indicate that the boundary layer enters the throat region, undergoes a phase transition, and then returns to a laminar state due to re-acceleration. The turbulence intensity in this region, coupled with the width of the transition zone, increases with higher upstream stagnation pressure. Furthermore, simulation of the unsteady starting flow shows that the passage time of unsteady waves and the quasi-steady region is good enough to have a steady state boundary layer assumption. The formation of shock and expansion wave systems towards the downstream diaphragm and the reflection and expansion waves towards the upstream shock tube were well-simulated after the diaphragm rupture.

---

* Corresponding Author’s E-mail: dr.mohammadiamin@gmail.com

How to Cite this Article:
S. Malekipour, I. Bahman Jahromi, and M. Mohammadi Amin, "Boundary layer transition and re-laminarization in the nozzle of a shock tunnel–a numerical study," *Journal of Space Science and Technology*, Vol. 18, Special Issue, pp. 52-59, 2025, https://doi.org/10.22034/JSST.2025.1525.

1. INTRODUCTION

The exploration of flow patterns in shock tunnels is one of the fascinating areas for the development and optimization of hypersonic test equipment [1]. In many hypersonic flows through convergent-divergent nozzles, the boundary layer is subjected to transition condition or even experiences a significant reduction in turbulence intensity [2]. The growth rate of the laminar or turbulent boundary layer has a substantial impact on the flow quality at the exit [3]. So, numerous studies have been conducted to investigate the status of the boundary layer in such applications. Gu and Herbert, have studied the capabilities and limitations of the available hypersonic equipment [4]. One of the major drawbacks of conventional hypersonic wind tunnels and shock tunnels is the presence of noise due to upstream flow oscillations, often one or two orders of magnitude higher than flight conditions. The dominant noise in these oscillations is acoustic noise emanating from the turbulent boundary layer on the diverging nozzle walls and they might have a noticeable effect on boundary layer transition and other phenomena in test section. One of the main challenges in high speed flow research is the accurate prediction of boundary layer transition and re-laminarization. In many high speed flows through convergent-divergent nozzles, the boundary layer is subjected to transition condition and also experiences a significant reduction in turbulence intensity, up to 100%. Researches have shown that pressure gradients resulting from flow curvature and geometry in hypervelocity boundary layers can significantly affect the flow turbulence level [2].

Since the early 21st century, most numerical analyses of high speed nozzles have used the SST (Shear Stress Transport) model. The SST model combines the advantages of the k-ε and k-ω models. Duan et al. used it to simulate the performance of hypersonic nozzles [5]. Ownbey used the SST model for designing a high-enthalpy hypersonic nozzle [6]. Collen et al. and Hoffman et al. also utilized this model for studying nozzle of Mach 7 in test facilities [7,8]. Shear Stress Transport model is not capable to predict the transition or re-laminarization of the boundary layer.

The topic of re-laminarization in the boundary layer of high speed nozzles emerged in the late 20th century and continues to be a significant focus in this field. Back et al. observed that the actual boundary layer thickness was lower than expected while examining heat transfer rates on the wall of a conical nozzle at high Reynolds numbers (around 105 to 106 based on throat diameter) in the JPL laboratory. Further investigation led them to conclude that the turbulent boundary layer seemed to become laminar again. They proposed a criterion based on the properties of the boundary layer edge [9]. Kemp et al. studied the boundary layers of high speed nozzles from Mach 20 to 47. Despite the desirable pressure gradient, they found that the flow becomes turbulent in the throat and becomes laminar again in that region [10]. Kreskovsky et al. investigated the effect of severe acceleration of the flow on the turbulent boundary layer by comparing analytical and experimental results. The findings showed that even in the presence of high turbulence levels upstream, the boundary layer becomes laminar in the throat, and its thickness significantly decreases [11]. Jentink investigated various definitions of flow acceleration criteria using turbulence models to identify boundary layer re-laminarization in nozzles [12]. The study of transition conditions and re-laminarization of the boundary layer continued on various geometries until around 2005 when turbulence models with the capability to detect transition zones started being used in simulations.

Abraham et al. utilized the three-equation Menter model (γ-SST) for defining a criterion to identify the re-laminarization of turbulent flow in internal flows. He defined a criterion as the ratio of turbulence production to its dissipation, stating that if it is less than one, the boundary layer tends to become laminar [13]. Bader et al. studied the capability of the four-equation model (γ-Reθ-SST) in predicting the re-laminarization of the flow over a turbine airfoil under rapid acceleration conditions. The results of these analyses were compared with DNS results, demonstrating that the four-equation model performs well [14].

Kiselv et al. investigated heat transfer in a small supersonic nozzle under conditions of re-laminarization of the boundary layer. They used both the three-equation and four-equation turbulence models. The heat transfer coefficient in the throat region was higher in the three-equation model than the actual value, while in the four-equation model, it was lower than the experimental value, indicating that four-equation model has a greater tendency toward flow re-laminarization conditions [15].

So, one of the main challenges in hypersonic flow research is the accurate prediction of boundary layer transition. The performance of the shock tunnel hypersonic flow is highly sensitive to various disturbances and pressure fluctuations, introducing complexity to the analysis. To ensure a uniform flow at the outlet, a nozzle design is considered here that was optimized previously by the authors [16] based on a fully turbulent Reynolds-Averaged Navier-Stokes (RANS) steady-state CFD model (Ansys Fluent) which similar to most numerical analyses of hypersonic nozzles, have used SST (Shear Stress Transport) turbulence model that combines the advantages of the k-ε and k-ω models [6].

Given the development of new numerical methods for studying the transition region and the lack of resources regarding the efficiency of these methods in converging-diverging hypersonic nozzle flows, this paper focuses on studying the transition region and investigates the effect of upstream pressure in the transition region. The transition and re-laminarization can be distinguished by transitional models in hypersonic nozzle instead of classic re-laminarization parameters for the first time. Then, the flow behavior and interaction of transient unsteady starting waves in nozzle with the boundary layer are examined. Comparing the simulation results with the experimental data obtained from the ARIST shock tunnel [17] shows a good agreement and the capability of CFD for understanding complex phenomena related to the formation of shock and expansion waves and their interaction with the boundary layer. This unsteady simulation shows that the duration of the steady state flow establishment is enough for such assumption in the boundary layer study.

2. METHODOLOGY

In this work, the ARIST shock tunnel nozzle is considered, designed to create test conditions with hypersonic Mach numbers (Mach 6) and high stagnation temperatures (around 600 Kelvin). An overall view of the ARIST shock tunnel facility, the nozzle, and the test section is depicted in Figure (1). The shock tunnel generally consists of a high-pressure tube (driver section), a low-pressure tube (driven section), the main diaphragm section, a secondary diaphragm, a converging-diverging nozzle, test section and a dump tank. Complete specifications and the details of this shock tunnel are presented in [17].

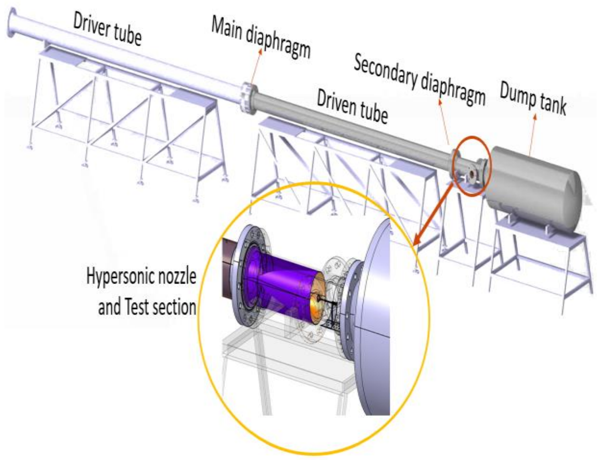

Fig. 1. ARIST reflected shock tunnel [10].

Based on Reynolds-Averaged Navier-Stokes formulation for the fluid dynamics modeling [18], the four-equation model was chosen to investigate the boundary layer in the selected nozzle. The Langtry-Menter four-equation model, also known as γ-Reθ or γ-Reθ-SST, has been developed for predicting the boundary layer transition with RANS models. For this purpose, the intermittency equation and the transition onset momentum thickness equation are added to the model. For that, the intermittency variable is multiplied in the turbulence kinetic energy production term, and its dissipation term [18]:

$$\begin{aligned}\frac{\partial \rho k}{\partial t}+\frac{\partial \rho u_j k}{\partial x_j}\\ =\gamma_{eff}.P_k-\min\left(\max\left(\gamma_{eff},0.1\right),1.0\right).\beta^*\rho\omega k\\ +\frac{\partial}{\partial x_j}\left[(\mu+\sigma_k\mu_t)\frac{\partial k}{\partial x_j}\right]\end{aligned} \tag{1}$$

For γ and Re_θ:

$$\frac{\partial \rho\gamma}{\partial t}+\frac{\partial \rho u_j\gamma}{\partial x_j}=P_\gamma-E_\gamma+\frac{\partial}{\partial x_j}\left[\left(\mu+\frac{\mu_t}{\sigma_f}\right)\frac{\partial\gamma}{\partial x_j}\right]$$

$$\frac{\partial \rho\tilde{R}e_{\theta t}}{\partial t}+\frac{\partial \rho u_j\tilde{R}e_{\theta t}}{\partial x_j}=P_{\theta t}+\frac{\partial}{\partial x_j}\left[\sigma_{\theta t}(\mu+\mu_t)\frac{\partial\tilde{R}e_{\theta t}}{\partial x_j}\right]$$

The correlation equations used for transition prediction are based on the idea that the boundary layer transition initiates when reaching a critical value of the Transition onset momentum thickness Reynolds number, $Re_{\theta t}$. However, this criterion is meaningful only along the wall and in one dimension. Therefore, Langtry and Menter introduced the transport variable of $\tilde{R}e_{\theta t}$, which can be applied throughout the flow field. It is expressed as an empirical relationship as a function of the pressure gradient and the turbulence intensity of the free stream. The production term in the transport equation of $\tilde{R}e_{\theta t}$ is formulated as follows:

$$P_{\theta t} = c_{\theta t}\rho\frac{\rho U^2}{500\mu}\left(Re_{\theta t} - \tilde{R}e_{\theta t}\right)(1.0 - F_{\theta t}) \tag{2}$$

The production and dissipation terms of the γ transport equation are formulated as follows:

$$P_\gamma = F_{length}c_{a1}\rho S[\gamma F_{onset}]^{0.5}(1 - c_{e1}\gamma)$$

$$E_\gamma = c_{a2}\rho\Omega\gamma F_{turb}(c_{e2}\gamma - 1)$$

$$F_{onset} = \max\,(F_{onset2} - F_{onset3}, 0)$$

$$F_{onset3} = \max\,\left(1 - \left(\frac{R_T}{2.5}\right)^3, 0\right)$$

$$F_{onset2} = \min\,\left(\max\left(F_{onset1}, F_{onset1}{}^4\right), 2.0\right)$$

$$F_{onset1} = \frac{Re_v}{2.193Re_{\theta c}}$$

$$Re_v = \frac{\rho S d^2}{\mu}$$

The production term in the intermittency transport equation leads to an increase in intermittency and, consequently, triggers the transition, while the dissipation term promotes the re-laminarization of the boundary layer. The F_{length} and F_{onset} terms are essential for determining the length of the transition region length and location, depending on the $\tilde{R}e_{\theta t}$. The term F_{turb} depends only on local turbulence parameters, k and ω. The term $Re_{\theta c}$ in a function of $\tilde{R}e_{\theta t}$ and d is the nearest distance of arbitrary point in flow field to the wall. S and Ω are the strain rate and the vorticity, respectively. In laminar boundary layer separation conditions, to ensure the separated flow quickly enters the transition and turbulence phase and reattaches to the surface, the parameter γ_{eff} is introduced. In fact, γ is forced to have a value higher than one in separation conditions [19].

3. RESULTS AND DISCUSSIONS

For the validation of the CFD model, the boundary layer analysis of references [20, 21] for hypersonic flow over a flat plate has been studied. The results of the three- and four-equation SST models, are compared with the experimental results from [12], and the numerical results from [13], that showed a good agreement for the heat flux on the wall Figure (2). It is observed that the three-equation model predicts the transition location upstream of experimental onset, while the four-equation model predicts it a bit downstream. However, the behavior of the experimental data in the transitional region is much closer to the four-equation model. Thus, the four-equation model was chosen to investigate the boundary layer in the selected nozzle.

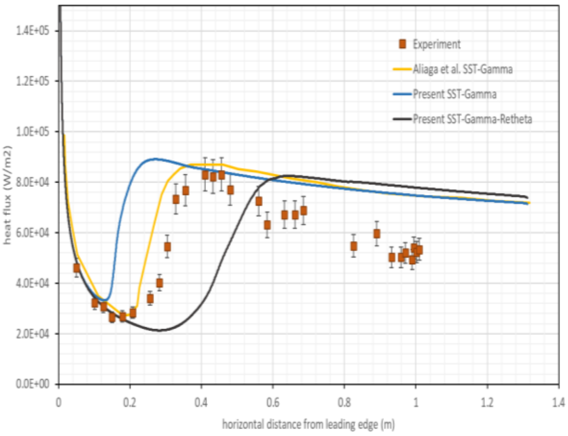

Fig. 2. Heat flux on a flat plate in Mach 11.

A no-slip adiabatic wall is considered for the nozzle and axisymmetric condition for the centerline. The simulations are performed with ANSYS Fluent 2016. This solver uses a finite volume approach with cell-centered variable arrangement. Density-based solution is used which is more advantageous for highly compressible applications. The fully coupled implicit algorithm provides 2nd order spatial discretization of the flow and turbulence equations, and it includes an AUSM scheme for the numerical convective flux. The independence of the solution from the grid is examined with four different computational grids. Additionally, the value of y^+ should be kept below one. The convergence criterion is the residual values to be less than 10^{-6}.

The computational domain, grid, and boundary conditions are illustrated in Figure (3). The comparison of Mach number distribution at the outlet of nozzle using numerical and experimental data in Figure (4) shows a good match between the experimental and simulation results (<3% error).

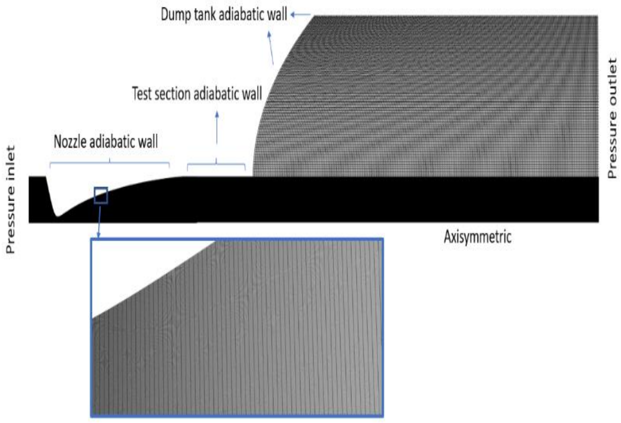

Fig. 3. Computational domain, grid, and boundary conditions.

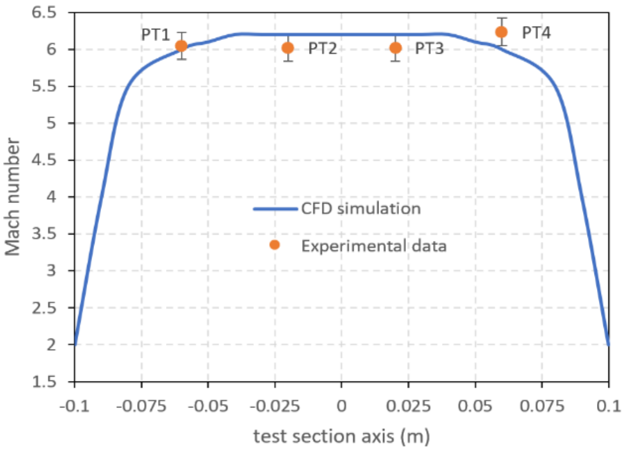

Fig. 4. Validation of Mach number at outlet.

For a better understanding of the flow nature, results of the shear stress distribution are presented under the assumptions of laminar flow and fully turbulent flow. It should be noted that here, the independence of the solution from the upstream turbulence intensity is examined and it was observed that with an increase in turbulence intensity, a negligible increase in wall shear stress occurs in the early centimeters of the convergent section. As shown in Figures (5) and (6), the flow in the region before the throat deviates from laminar state and moves towards transition and turbulence. After passing through the throat with acceleration, it returns to a laminar state again. The highlighted region in the figures indicates the transitional region. It is also can be observed that with an increase in pressure, the transitional and turbulent regions become larger and move towards the divergent section and the nozzle exit.

Additionally, the values of wall shear stress in the transitional analysis approach those obtained from the turbulent flow analysis, to the point where at 25 bars, these two curves coincide. Based on further numerical results, increasing the total pressure up to 40 bar, will result the boundary layer to be turbulent along almost the entire length of the nozzle.

.

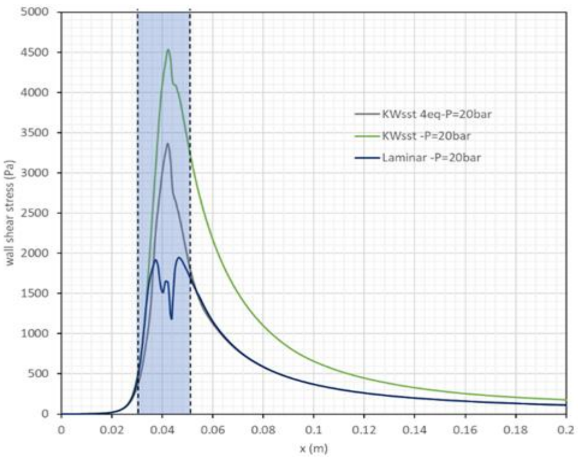

Fig. 5. Wall shear stress on the nozzle wall at total pressure of 20 bar.

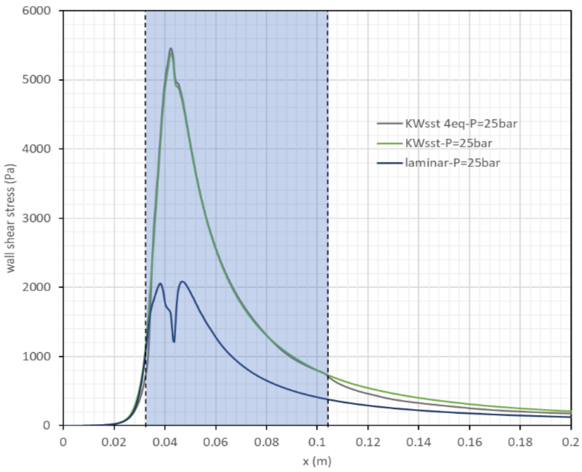

Fig. 6. Wall shear stress on the nozzle wall at total pressure of 25 bar.

In the next step, it is necessary to examine the boundary layer conditions for the optimal nozzle in the design conditions with the base nozzle. In Figure (7), the wall shear stress distribution for the base and optimal nozzles in the design conditions are compared. Due to the reduction in the length of the convergent section of the optimal nozzle, the shear stress level in the throat area of this nozzle is higher, the length of the optimal nozzle is shorter, but by controlling the curve of the divergent section and reducing the total length of the nozzle, the wall shear stress level in the divergent section and the outlet of the optimal nozzle is about 50% lower than that of the base nozzle.

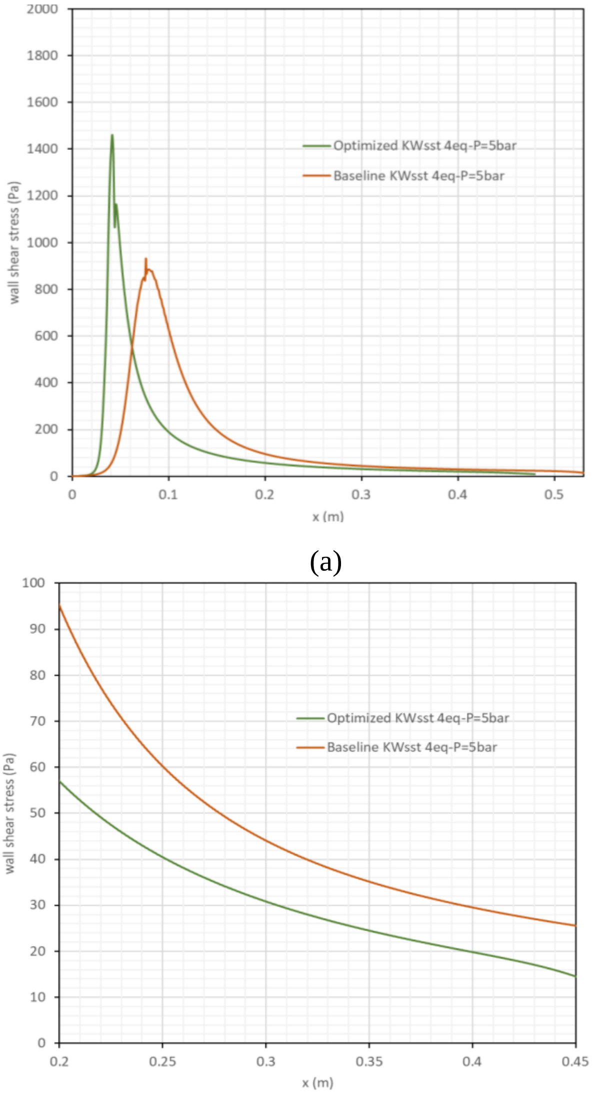

(a)

(b)

Fig. 7. Base and optimal nozzle wall shear stress distribution a) entire nozzle, b) end of divergent section.

In Figure (8), the velocity distribution in the nozzle outlet plane is presented in terms of the nozzle outlet radius. Also, in this figure, the effect of the analysis assuming laminar, turbulent and transient flow can be seen. It can be seen that the analysis with the four-equation model is consistent with the laminar analysis. Also, the boundary layer thickness in the optimal nozzle based on the 99% free stream velocity criterion has been reduced by about 40%.

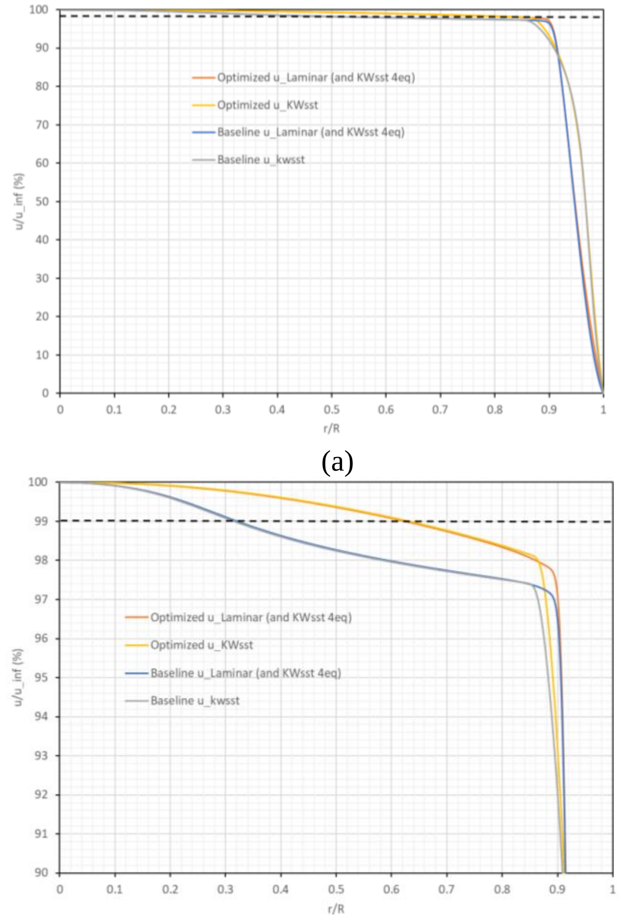

(a)

(b)

Fig. 8. Velocity distribution vs the outlet radius a) over the entire radius b) the boundary layer edge.

For the unsteady numerical simulation of hypersonic nozzle flow, the finite volume method with second-order accuracy and axisymmetric assumptions has been employed. The simulations have been conducted for both laminar and turbulent flow conditions. The working fluid, consistent with the test, is considered to be ideal air. The transient part is solved with implicit method. Also, the nozzle has a contoured convergent section with a secondary diaphragm upstream of nozzle. The diaphragm effect is simulated by initializing the upstream region of the nozzle with reservoir pressure and temperature. To observe the effect of diaphragm burst, radial oscillation is considered in the initial condition. The formation of the primary and secondary shock waves (PS & SS) moving downstream the nozzle, as well as the generation of reflective waves (RS) and expansion waves moving upstream towards the shock tube, is studied. Figures (7) and (8) show two instances of 0.03, 0.180 ms after secondary diaphragm burst, respectively. For the 0.18 ms snapshot, there are a strong secondary shock wave following an expansion region and a weaker primary shock wave heading downstream the nozzle while a reflected shock wave and expansion waves are going toward upstream of the shock tube.

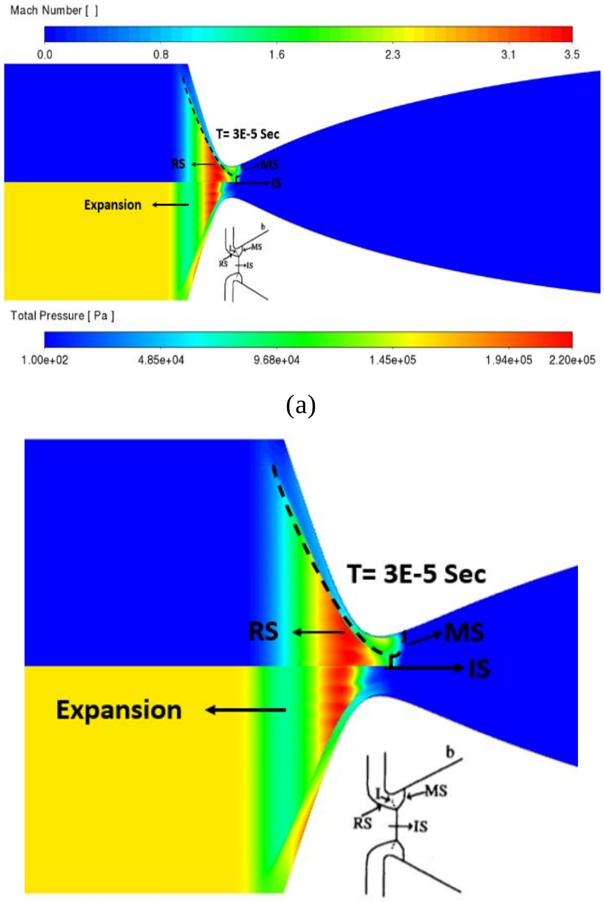

(a)

(b)

Fig. 9. Mach number and total pressure contours after secondary diaphragm burst; a) entire nozzle, b) magnified throat region.

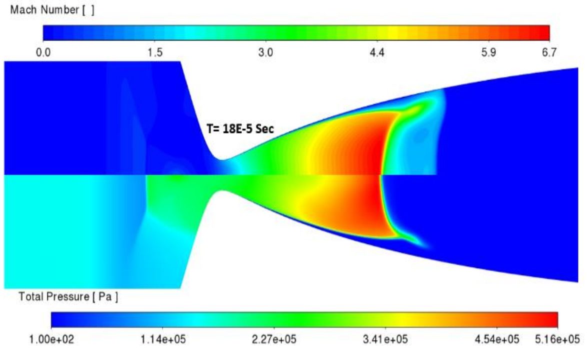

Fig. 10. Mach number and total pressure contours at 0.03 milliseconds after secondary diaphragm burst.

The starting time from numerical and experimental results is about 1.5 msec which is consistent with the calculations in design phase and it shows that the remaining time of steady state flow is an appropriate assumption for boundary layer study.

4. CONCLUSIONS

Mach 6 nozzle boundary layer was investigated via numerical simulation including a suitable four-equation model for studying the transitional flow. The results revealed the presence of a boundary layer transition in the throat region, and with the acceleration of the flow, the boundary layer reverts to a laminar state. As the upstream pressure of the nozzle increases, i.e. an increase in Reynolds number, turbulence intensity in the transitional region amplifies, causing a delay in the flow re-laminarization towards the nozzle exit. At high pressures, the entire divergent part of the nozzle can be situated within the turbulent boundary layer. Furthermore, the unsteady flow at the initiation of the nozzle was numerically examined. The formation of shock and expansion wave systems towards the downstream diaphragm and the reflection and expansion waves towards the upstream shock tube were well-simulated after the diaphragm rupture. It is observed that the passage time of unsteady waves and the quasi-steady flow establishment is good enough to have a steady state boundary layer assumption.

CONFLICT OF INTERESTS

The authors declare that they have no conflict of interest.

REFERENCES

[1] I. Kim, S. Lee, G. Park, and J.K. Lee, “Overview of flow diagnosis in a shock tunnel,” *International Journal of Aeronautical and Space Sciences*, vol. 18, no. 3, pp 425-435, 2017, https://doi.org/10.5139/IJASS.2017.18.3.425.

[2] N. R. Tichenor, “Characterization of the influence of a favorable pressure gradient on the basic structure of a Mach 5.0 high Reynolds number supersonic turbulent boundary layer,” Ph.D. dissertation, Texas A&M University, 2010.

[3] F. Lu and D. Wilson, “Survey of short duration, hypersonic and hypervelocity facilities,” in *25th Plasmadynamics and Lasers Conference*, Springs,

CO, USA, 1994, Paper 94-2491, https://doi.org/10.2514/6.1994-2491.

[4] S. Gu and O. Herbert, "Capabilities and limitations of existing hypersonic facilities," *Progress in Aerospace Sciences*, vol. 113, 2020, Art. no. 100607, https://doi.org/10.1016/j.paerosci.2020.100607.

[5] L. Duan, G. L. Nicholson, J. Huang, K. M. Casper, R. Wagnild, and N. Bitter, "Direct numerical simulation of nozzle-wall pressure fluctuations in a mach 8 wind tunnel." in *AIAA Scitech 2019 Forum*, San Diego, California, 2019, Paper 0874, https://doi.org/10.2514/6.2019-0874.

[6] J. C. Ownbey, "Preliminary design of a high-enthalpy hypersonic wind tunnel facility and analysis of flow interactions in a high-speed missile configuration," M.S. thesis, School of Aeronautics and Astronautics West Lafayette, Indiana, 2021.

[7] P. Collen *et al.*, "Development and commissioning of the T6 Stalker Tunnel," *Experiments in Fluids*, vol. 62, 2021, Art. no. 225, https://doi.org/10.1007/s00348-021-03298-1.

[8] E. N. Hoffman *et al.*, "Characterization of the UTSA mach 7 ludwieg tube," in *AIAA SciTech 2022 Forum*, San Diego, CA & Virtual, 2022, https://doi.org/10.2514/6.2022-1600.

[9] L. H. Back, R. F. Cuffel, and P. F. Massier, "Laminarization of a turbulent boundary layer in nozzle flow—boundary layer and heat transfer measurements with wall cooling," *ASME. Journal of Heat andMass Transfe*, vol. 92, no. 3, pp. 333-344, 1970, https://doi.org/10.1115/1.3449668.

[10] J. H. Kemp Jr and F. K. Owen, "Nozzle wall boundary layers at Mach numbers 20 to 47," *AIAA Journal*, vol. 10, no. 7, pp. 872-879, 1972, https://doi.org/10.2514/3.50239.

[11] J. P. Kreskovsky, S. J. Shamroth, and H. Mcdonald, "Parametric study of relaminarization of turbulent boundary layers on nozzle walls," NASA, Tech. Rep. CR-2370, 1974.

[12] T. Jentink, "An evaluation of nozzle relaminarization using low Reynolds number K-epsilon turbulence models," in *31st Aerospace Sciences Meeting*, Reno, NV, USA, 1993, https://doi.org/10.2514/6.1993-610.

[13] J. P. Abraham, E. M. Sparrow, J. C. K. Tong, and D. W. Bettenhausen, "Internal flows which transist from turbulent through intermittent to laminar," *International Journal of Thermal Sciences*, vol. 49, no. 2, pp. 256-263, 2010, https://doi.org/10.1016/j.ijthermalsci.2009.07.013.

[14] P. Bader, P. Pieringer, and W. Sanz, "On the capability of transition models to predict relaminarization," in *12th European Conference on Turbomachinery Fluid dynamics & Thermodynamics*, Stockholm, Sweden, 2017, Paper ETC2017-328, https://doi.org/10.29008/ETC2017-328.

[15] N.A. Kiselev, N.S. Malastowski, Y.A. Vinogradov, and A.G. Zditovets, "Experimental and numerical study of heat transfer under laminarization condition in a small size supersonic nozzle," *International Journal of Thermal Sciences*, vol. 187, 2023, Art. no. 108182, https://doi.org/10.1016/j.ijthermalsci.2023.108182.

[16]S. Malekipour, M. Mohammadi Amin, and I. Bahman Jahromi, "Towards a low noise shock tunnel facility via multi-objective optimization of hypersonic nozzle," *Journal of Aerospace Engineering*, vol. 34, no. 5, 2021, https://doi.org/10.1061/(ASCE)AS.1943-5525.0001296.

[17] S. Malekipour, I. Bahman Jahromi, and M. Mohammadi Amin, "Experimental investigation of Mach 6 optimal hypersonic nozzle performance in shock tunnel," *Journal of Aeronautical Engineering*, vol. 25, no. 2, pp. 21-33, 2023, https://doi.org/10.22034/joae.2023.366731.1139.

[18] F. R. Menter, R. B. Langtry, S. R. Likki, Y. B. Suzen, P. G. Huang, and S. Völker, "A correlation-based transition model using local variables—part I: Model formulation," *Journal of Turbomachinery*, vol. 128, no. 3, pp. 413-422, 2006, https://doi.org/10.1115/1.2184352.

[19] S. Kang, H. C. Shin, S. H. Park, J. Park, and D. Park, "Comparative assessment of modified γ-Re_$_{\theta t}$ models for scramjet intake flow analysis," *International Journal of Aerospace Engineering*, vol. 2021, no. 1, 2021, Art. no. 9916416, https://doi.org/10.1155/2021/9916416.

[20] J. G. Marvin, J. L. Brown, and P. A. Gnoffo, "Experimental database with baseline CFD solutions: 2-D and axisymmetric hypersonic shock-wave/turbulent-boundary-layer interactions," NASA, Tech. Rep. TM-2013-216604. 2013.

[21] C. Aliaga, K. Guan, J. Selvanayagam, J. Stokes, V. Viti, and F. Menter, "Hypersonic applications of the laminar turbulent transition SST model in ANSYS Fluent," in *AIAA Aviation 2020 Forum*, Virtual Event, 2020, https://doi.org/10.2514/6.2020-3290.

.